Investigation and Analysis of Phenomena in the Far-Infrared Region

Calum Neil Alasdair Towler, MChem

Submitted in accordance with the requirements for the degree of Doctor of Philosophy

The University of Leeds

School of Chemistry

December 2022

Declaration

The candidate confirms that the work submitted is his own, except where work which has formed part of jointly authored publications has been included. The contribution of the candidate and the other authors to this work has been explicitly indicated below. The candidate confirms that appropriate credit has been given within the thesis where reference has been made to the work of others.

Two publications have arisen from the work presented in this thesis, both from work detailed in Chapter 4:

C. N. A. Towler, J. Kendrick, and A. D. Burnett, "Understanding the effect of dispersion corrections on the calculated spectra of α-lactose monohydrate," in *2020 45th International Conference on Infrared, Millimeter, and Terahertz Waves (IRMMW-THz)*, 2020, pp. 1–2. 25

The time-domain spectroscopy system used to measure the terahertz absorption spectrum at 4 K was originally designed by Dr. Andrew Burnett. The software used to produce terahertz absorption spectra from calculated mode frequencies and intensities was written by Dr. John Kendrick. I collected all the data, produced all the figures and wrote the initial and final drafts of this paper, with all authors contributing between these drafts.

A. D. Burnett, **C. N. A. Towler**, and J. Kendrick, "Calculating the complex permittivity of powdered crystalline materials," in *2019 44th International Conference on Infrared, Millimeter, and Terahertz Waves (IRMMW-THz)*, 2019, pp. 1–2. 9

I produced the data and designed the figure for the comparison of the calculated and experimental terahertz absorption spectra of α-Lactose Monohydrate. No other contribution to this work occurred.

This thesis is dedicated to my wonderful parents

Acknowledgements

Firstly, I want to extend my enormous gratitude to Dr. Andrew Burnett who was my primary supervisor throughout my PhD and my Masters project. His support, guidance and patience has been invaluable throughout and I will forever be thankful for everything. Not only did he provide vital knowledge and direction but he also assisted with motivation and perspective when, owing to various difficult challenges during the PhD, these were not easily attained.

I would also like to extend my thanks to Dr. Aniela Dunn, Dr. Thomas Gill, Dr. Joshua Freeman and Dr. David Bacon, as well as the other members of the University of Leeds Terahertz Group, for providing their expertise and assistance when I was often out of my depth. From monitoring me in the clean room to endlessly diagnosing issues with the various experimental set-ups, their help was a critical element of my success in this project.

To my parents, and by extension my siblings and their children, your unwavering support over the last few years has made this project possible. Thank you so much for helping me attain this monumental achievement.

Finally, to my friends old and new. Thank you all for the wonderful times over the last few years. In particular, I would like to thank my friends Sam and Emma, who were there for me at every step and who kept me happy and alive during those critical junctures.

Thank you, again, everyone.

Abstract

The far-infrared (IR) frequency range, or more specifically the terahertz (THz) frequency range, of the electromagnetic spectrum has been comparatively underutilised in the field of solid-state vibrational spectroscopy. This was historically owing to a lack of coherent sources and detectors but now stems from the challenges involved with the interpretation of the resultant spectra as the excited motions in this frequency range consist of complex motions that must be deciphered with the aid of computational simulation using methods such as Density Functional Theory (DFT). This, in turn, gives rise to its own challenges as the accurate simulation of large organic molecular crystals can be computationally expensive.

In DFT, weak intermolecular bonds such as H-bonds are poorly represented and an empirical correction is often included to account for them. These are called dispersion corrections and an investigation into the appropriate dispersion correction for α-Lactose Monohydrate (α-LM) was conducted. This molecule was chosen owing to its uncommonly sharp absorption peaks in this frequency range. DFT uses the harmonic approximation to calculate vibrational mode frequencies but this will inevitably remove important anharmonic effects, such as thermal expansion, from the calculation which may reduce correlation between calculated and experimental spectra. The Quasi-Harmonic Approximation (QHA) allows for thermal expansion to be incorporated into the system by applying the harmonic approximation to a range of volumes. This was used to calculate the thermodynamic properties and temperature dependent mode properties of α-LM. This in turn was used to calculate the THz absorption spectrum of α-LM at $300\,\mathrm{K}$.

The primary source of THz radiation for broadband spectroscopy is photoconductive switches. These are excited with femtosecond laser pulses that are focused onto a gap between two electrodes. An investigation into the appropriate gap-size for a photoconductive switch being excited by a $150\,\mathrm{mW}$ fibre laser was carried out, with the appropriate gap-size being determined to be $20\,\mathrm{\mu m}$.

Contents

List of Figures

List of Tables

Acronyms

αLM α-Lactose Monohydrate

ATR Attenuated Total Reflectance

BBO β-Barium Borate

BJ Becke-Johnson

BZ Brillouin Zone

CW Continuous Wave

DFPT Density Functional Perturbation Theory

DFT Density Functional Theory

DiC Dispersion Correction

EM Electromagnetic

EO Electro-Optic

FD Frequency Domain

FT Fourier Transform

FTIR Fourier-Transform Infrared Spectroscopy

FWHM Full Width at Half Maxiumum

GGA Generalised Gradient Approximation

GTO Gaussian Type Orbital

HO Harmonic Oscillator

IPA Isopropyl Alcohol

IR Infrared

LDA Local Density Approximation

LT Low Temperature Grown

MBSE Many Body Shrödinger Wavefunction

MD Molecular Dynamics

PAW Projector Augmented-Wave

PBE Perdew-Burke-Ernzerhof

PC Photoconductive

PTFE Polytetrafluoroethane

QCLs Quantum Cascade Lasers

QHA Quasi-Harmonic Approximation

RMS Root Mean Squared

SI Semi-Insulating

SNR Signal-to-Noise Ratio

STO Slater Type Orbital

TD Time Domain

THz Terahertz

THz-TDS THz Time-Domain Spectroscopy

TPI Terahertz Pulsed Imaging

TPX Polymethylpentene

TS Tkatchenko-Scheffler

UV Ultraviolet

VDOS Vibrational Density of States

VDW Van der Waals

XRD X-Ray Diffraction

Chapter 1

Introduction

Whilst chemists frequently use the near and mid-infrared (IR) regions of the Electromagnetic (EM) spectrum regularly in their research, the far-IR or terahertz (THz) region, commonly defined as 0.1–$10\,\text{THz}$ or 3–$333\,\text{cm}^{-1}$, has been comparatively underutilised. This was a result of the lack of coherent, strong sources of EM radiation in this frequency range, the so-called 'Terahertz Gap', and the location of this region between the microwave and IR regions is shown in Figure 1.1. For brevity, THz EM radiation will be referred to as THz radiation for the remainder of this document. In the previous decades, the technology behind sources and detectors for THz radiation has seen significant improvements and this has resulted in a sharp increase in the number of studies that involve THz radiation across a variety of applications [1].

1.1   Applications of Terahertz Radiation

Owing to the nature of THz radiation, it can penetrate most non-conducting and non-polar materials which can provide advantages over traditional visible and IR based imaging systems, allowing for potential applications in security screening of both people [2] and commercial packaging [3]. Whilst THz can transmit through these types of materials, it is severely attenuated by water which is a polar molecule. THz radiation is also non-ionising which means it can be used to image materials non-destructively. These properties have
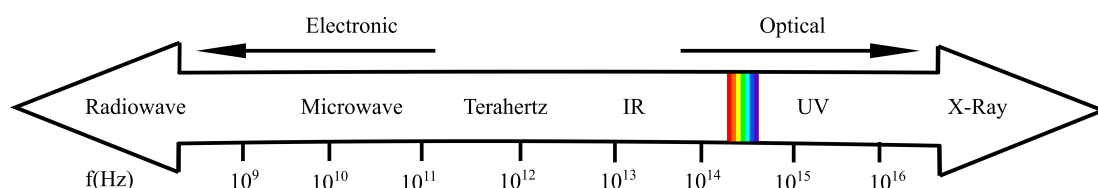
Figure 1.1: A graphic of the EM spectrum indicating the relative position of the far-IR or THz region with electronic and optical arrows indicating the traditional method of generation.

led to the development of a number of biological and medical applications [4–8]. THz radiation's sensitivity to water content has been utilised for medical applications where highly sensitive measurements of water content can be used to differentiate between different tissue types [9]. This may also be used for the detection and monitoring of certain types of cancer cells [10]. A significant commercial application of THz imaging in the pharmaceutical industry has been the investigations into tablet coatings [11]. Until recently, the methods used to investigate tablets were generally destructive or were not suitable for on-line rapid measurements [12]. Terahertz Pulsed Imaging (TPI) overcomes these issues as it is non-destructive, sensitive to small changes in the refractive index of a material owing to reflections occurring at these interfaces and can suitably penetrate most pharmaceutically active compounds and common inert tablet components such as lactose. If the refractive index of the sample is known, these reflections can be utilised to extract accurate values for the thickness of each layer even in complex sample geometries. As the wavelength of THz radiation is often longer than the particle size, scattering is minimal in these measurements compared to using conventional methods [13]. Extremely thin layers ($< 20\,\mu$m) are not suitably separated in the time-domain, and so it has been shown that TPI can be used in conjunction with other non-destructive imaging techniques such as Optical Coherence Tomography [14] to provide a complete picture of the geometry of these multi-layer systems.

Whilst THz imaging has seen significant improvements and has several important applications, the main focus and majority of technological development in this region of the EM spectrum has been on a branch of spectroscopy that has begun to come to maturity. This is called THz Time-Domain Spectroscopy (THz-TDS) and allows for the ability to probe the far-IR in a way that is not possible using traditional methods of generating IR radiation. This is owing to the increasing power of THz sources and a higher Signal-to-Noise Ratio (SNR) in this region when compared to traditional IR measurement methods such as Fourier-Transform Infrared Spectroscopy (FTIR) in this lower frequency range. The raw signals produced by this technique are shown in Figure 1.2 where it can be seen that the sample trace has been delayed and attenuated in comparison to the reference trace. These differences can be used to extract the frequency-dependent absorption coefficient and refractive index of a sample, along with its real and complex permittivity [15]. A more detailed discussion of THz-TDS will be provided in Chapter 2.

Whilst the mid-IR region corresponds to the frequency range of the vibrations of intra-molecular bonds and the near-IR region contains the combination and overtone modes of these vibrations, the phenomena in the far-IR are much more challenging to interpret. Instead of the vibrations between atoms within a molecule, the motions in the far-IR consist of inter-molecular vibrations, hindered rotations and torsions in the solid phase and free rotations in the gas phase. In the solid phase, these are extremely dependent
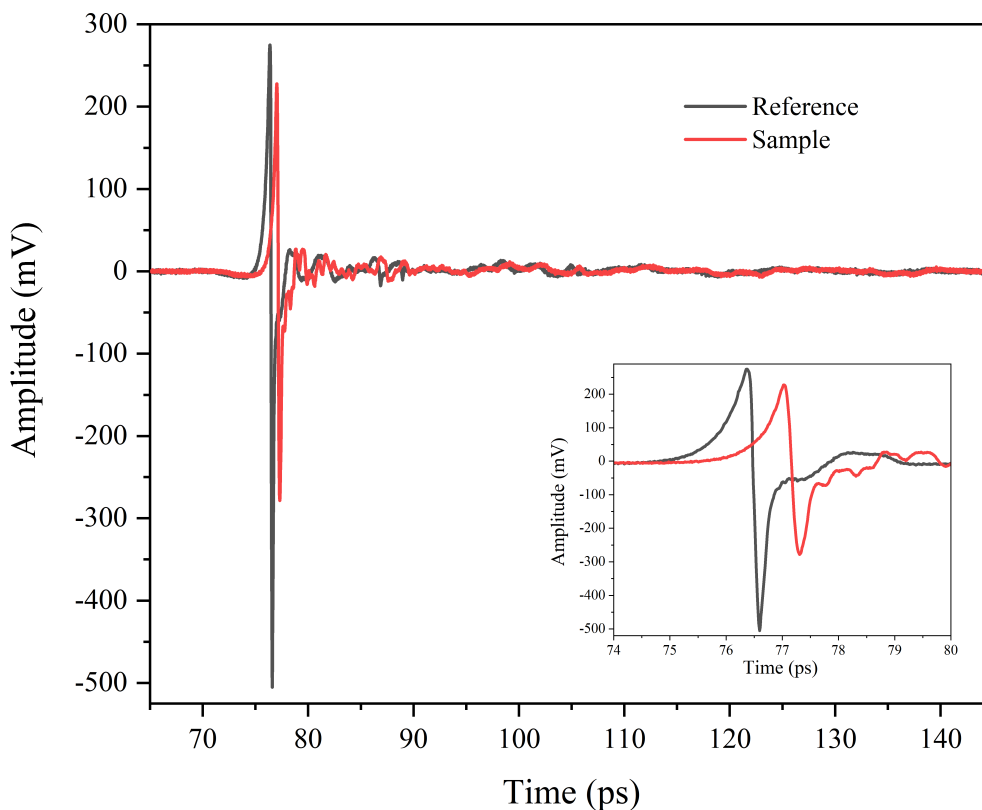
Figure 1.2: An example of two THz-TDS scans, where one has a sample placed in the beam path and the other is dry air which is used as a reference. It can be seen that the trace that represents the sample has been attenuated and delayed in time. The inset shows the same two traces but with a focus on the main pulses.

on the surrounding long-range ordering and overall chemical environment and are often referred to as phonons. Owing to the complex motions involved with these intermolecular modes, simple assignment linked to functional groups that occurs in the mid and near-IR is not possible and even clean, well resolved spectra of common organic materials can be challenging to interpret. This results in one of THz-TDS greatest strengths, which is its sensitivity to minute changes in molecular and crystalline structure and their dynamics. However, this also increases the challenge of understanding the underlying phenomena without the aid of computational modelling of the chemical environment and comparison to experimental data. A detailed discussion of these computational methods and the modelling of vibrational properties of molecules and crystals will be provided in Chapter 3.

This sensitivity to the surrounding chemical environment can be utilised in a variety of ways. As even the smallest changes in this long-range environment cause changes in the THz-TDS spectrum, it can be a powerful tool for characterising drugs and their polymorphs [16], even when X-Ray Diffraction (XRD) is incapable of distinguishing between materials [17–19]. Several studies have also been done on the interaction of THz radiation with amorphous materials and have found that THz radiation can interact with the

Vibrational Density of States (VDOS), the collective vibrational modes of non-crystalline materials. This has been shown to be useful as a probe for crystallisation, as sharp peaks begin to be identifiable on top of the broad absorption of the VDOS [20]. This broad absorption is owing to the strong dampening effect that a non-crystalline structure has on intermolecular motions [21]. This can be useful as certain new drugs are only biologically active in their amorphous forms thus their shelf life is dependent of their rate of crystallisation [22]. Owing to its non-destructive nature and the drastic changes in the spectral features for chemically and structurally similar molecules, THz-TDS radiation could potentially be used as a non-invasive way to detect dangerous materials in transport such as explosives or illegal drugs [23]. THz radiation is the appropriate energy to probe low energy inter-molecular bonds such as H-bond networks, in both liquids and solids, and their dynamics on the sub-ps timescale. Owing to this interaction, liquid water absorbs THz radiation, with two strong absorption bands at 650 and $200\,cm^{-1}$ respectively [24]. Whilst this can be a problem in most applications, it has allowed extensive study of water's role in biological processes. Many of these studies have been done on the hydration shells and dynamics of a wide range of biomolecules [25]. Through the development of these studies, the role of water, has been upgraded in its importance in many biological processes including the molecular recognition of enzymes, and protein folding and denaturing [26]. Some more recent developments have continued to provide insight into nature of solvation processes in water [27]. In water vapour there are a number of weakly absorbing modes throughout the range [28] and if these are not removed then spectral features can become obscured owing to the absorption peaks caused by the water vapour. Measurements taken in the THz frequency range are first purged with dry air or dry nitrogen to prevent this. As mentioned above, the hydrogen bond networks of solids can also be probed by THz radiation. This, alongside THz radiation's non-destructive nature, is being utilised by the pharmaceutical industry to probe the nature of organic crystalline materials [29]. $k_B T$, which is the Boltzmann constant multiplied by the temperature, is the amount of energy available to an atom or molecule at a given temperature and determines what energy levels are available. The value of $k_B T$ at room temperature corresponds to approximately 6.21 THz. This means that higher energy modes can be populated and molecules can move freely between energy states. These dynamics, including relaxation back to lower energy states and interaction between these modes, play a key role in a large proportion of chemical processes as these contribute significantly to the distribution of energy throughout a system [30, 31]. Understanding these processes and the phenomena underlying them is key to furthering our understanding of material science.

Most of the methods and applications above use THz electric field strengths that cause linear interactions in the system of interest. However, owing to advancements in THz generation efficiency, the electric field strengths have now become enough to induce non-linear behaviour in various systems [32]. The nature of these varies greatly, with

non-linear electrical carrier transport being one of the first non-linear phenomena to be observed with THz excitation [33]. Various groups have found non-linear lattice effects in crystals [32], liquids [34] and gases [35], indicating that there are many more potential applications for THz technologies as their generation efficiency and peak power increase.

1.2   Structure of Thesis and Aims of Project

The thesis will begin with Chapter 2 that will describe the theory behind the generation and detection of THz EM radiation and how this is used in various measurement techniques, with a specific focus on THz-TDS.

Chapter 3 will begin with a mathematical description of vibrational modes and then examine the process behind modelling systems of interest using Density Functional Theory (DFT) and describe the methodology of calculating and interpreting a THz-TDS spectrum.

Chapter 4 and Chapter 5 will be specifically focused on the further development of accurately modelling and analysing complex organic systems as this is one of the key challenges facing this technique. For this purpose, the molecule selected is α-Lactose Monohydrate (αLM), shown in Figure 1.3, owing to its sharp low-frequency features, particularly the peak at $0.52\,\mathrm{THz}/17\,\mathrm{cm}^{-1}$ which does not shift with temperature. αLM has recently been suggested to be an optimal candidate for a standard for both low-frequency vibrational spectroscopy and the theoretical calculation of these spectra [36]. Chapter 4 will compare the experimental THz absorption spectrum, taken at $4\,\mathrm{K}$, to calculated THz absorption spectra that have been obtained using five different dispersion corrections and attempt to provide a numerical justification for which is the most appropriate for organic systems and should be used moving forward.

(a) The molecular structure of αLM   (b) The molecular structure of βLM

Figure 1.3: The molecular structures of α and β Lactose Monohydrate. The asterisk marks the chirality centre on this molecule that determines which enantiomer is present.

Chapter 5 will examine the effect of including structural anharmonicity into the calculation process with the aim of better modelling the system. This will be tested by

attempting to produce a calculated room-temperature spectrum and comparing this to experiment. Some thermodynamic properties, such as heat capacity, are also calculated in this process and these results are also discussed.

Finally, Chapter 6 will examine the effect of the device gap size on photoconductive antennas used to generate THz EM radiation on the produced radiation and its implications for future developments. There will then be some concluding remarks and suggestions for the next phases of the work done in this thesis.

Chapter 2

Generation and Detection of Terahertz Radiation and the Methodology of Terahertz Time-Domain Spectroscopy

There are now many methods of generating and detecting significant field strengths of coherent THz radiation and these will be discussed in this chapter, with a particular focus on photoconductive (PC) switches and electro-optic (EO) crystals. The custom-built spectrometer and its variants that are used in this work will be described and the principle of THz-TDS and the process of data collection will be explained. Finally, the method behind the extraction of spectral properties of measured samples and some of the challenges associated with this will be discussed.

2.1   Terahertz Generation and Detection

With the value of $k_B T$ at room temperature being 6.21 THz, most matter emits THz radiation but these emissions are weak, incoherent and not suitable for practical use. However, these weak emissions have been used in astronomy where spectral lines in the THz region can be used for probing the composition and state of stellar objects [37].

Coherent THz radiation sources can be broadly separated into two categories: electrical and photonic. Electrical sources generate THz radiation through up-conversion of lower-frequency signals [38–40] or by utilising electron beams [41–43], whereas photonic sources generate THz radiation through down-conversion of optical and IR sources [44–47] or by direct THz emission [48, 49] and are discussed in further detail below. Whilst no electrical sources are used in this work, there are a range of these sources that are used by the wider THz community.

One significant area of development in electronic THz generation and detection has been in the area of Quantum Cascade Lasers (QCLs), which can produce both continuous wave (CW) THz and pulsed THz radiation in a narrow frequency region. In QCLs, sub-bands are developed in a material through a variety of different methods [48]. Electronic transitions between these states can be manipulated to fall inside the THz range. Quantum tunnelling allows a single electron to perform more than one of these transitions, producing the cascading effect after which the device is named [49]. This frequency can often be tuned, with one group reporting a range of $2.06 - 4.65$ THz with an output power of up to $4.2\,\mu W$ [50]. QCLs have been demonstrated to produce $2.4\,W$ in power in pulsed mode [14] and $0.23\,W$ in CW mode [51], and so a significant amount of research continues in the development of these devices for THz generation. The high power available at selective frequencies may allow pumping of phonon modes for THz pump spectroscopies. However, owing to the nature of these devices, the key limitation for this technology is the low temperatures required to operate it, resulting from the collapse of population inversion at higher temperatures [48]. The high powers demonstrated above were achieved at 10 and $15\,K$ respectively. This is problematic as techniques involving cryogens add to the complexity and cost of an overall procedure and these tend to be the main sources of temperature control. Therefore, another key area of development for QCLs has been in raising their operational temperatures. Currently, the highest operational temperature in pulsed mode is $250\,K$ [52], recently rising to $261\,K$ [53], and $129\,K$ [54] for CW, but these produce significantly less output power. Recently, it was demonstrated that thermo-electric cooling can replace cryogens for this purpose [55]. This allows low temperatures to be reached using a simpler and cheaper method, increasing the accessibility of this technique. Whilst simply operating QCLs, they only act as THz generators but through self-mixing [56], QCLs can act as detectors and a single device has been demonstrated as being able to act simultaneously as a generator and detector for the purposes of gas spectroscopy [57]. QCLs can also be used as detectors when combined with electronic components such as Schottky diodes [58]. Some modern applications of QCLs are using these devices on satellites for the study of species in the Earth's upper atmosphere layers [59], imaging [60] and wireless communication [61]. Whilst these devices show tremendous promise for the future of many THz applications, the ability of QCLs to generate radiation below $1\,THz$ is lowered as maintaining the required population inversion becomes much more difficult at lower frequencies. This has been achieved using strong magnetic fields [62] which complicates the system design significantly.

Solid-state electrical devices capable of frequency-multiplying lower-frequency signals have been pursued owing to the comparatively significant development in microwave generation technology. However, these struggle to get to frequencies above $1\,THz$ [63]. Devices like Schottky diodes which have been demonstrated to be capable of rapid sampling rates that enable real-time observation of changes to systems such as wetting or protein

unfolding [64].

The main alternative photonic sources are photomixers [44], where high frequency optical femtosecond lasers are focused and combined onto a PC switches to produce coherent CW THz radiation at a narrow frequency for applications surrounding non-linear optical effects. These devices have seen significant development using a range of materials to increase efficiency [65]. It was demonstrated that by focusing an optical beam onto the ambient gases in air a plasma is formed that emits low frequency EM radiation [66] and development in this area has resulted in a procedure where a β-Barium Borate (BBO) crystal is used to generate the second harmonic of the incident beam. The combination of these is focused onto air which will ionise and emit a broadband THz pulse with a bandwidth of up to 30 THz [45]. This technique allows coherent emission and detection throughout the IR range which is a significant improvement on most current techniques. However, an amplified laser is required which typically utilise lower repetition rates in order to generate the high powers required. With lower repetition rates comes a reduction in data samples which will decrease the SNR on the extracted data.

2.1.1 Photoconductive Switches

For spectroscopic applications, photoconductive (PC) switches [46] are widely used as a source of pulsed, coherent THz generation and as a THz detector. A PC switch, shown in Figure 2.1, consists of a semiconductor that is coated with a pair of Au electrodes, using a thin Ti layer as an adhesive to help the Au bind more cohesively. These electrodes are deposited in a way that leaves a small gap that where the size of the gap is on the order of tens to hundreds of microns. A femtosecond laser is focused onto this gap, where it generates electron-hole pairs in the semiconductor if the laser energy is larger than or equal to the bandgap of the semiconductor. A bias is applied across the gold electrodes, which accelerates the charge carriers across the gap [67]. THz radiation is generated without applying a bias through the photo-Dember effect [68] but significantly more photocurrent is generated in the semiconductor when a bias is applied. The bias is usually electrically chopped to allow for lock-in detection. This acceleration produces a transient current in the surface of the semiconductor, radiating a single-cycle coherent THz wave [69] with an amplitude, E_{THz}, proportional to the first derivative of the generated time dependent transient current $J(t)$:

$$E_{THz} \propto \frac{\delta J(t)}{\delta t} \tag{2.1.1}$$

This is proportional to both the incident optical fluence and the magnitude of the bias across the electrodes, which dictate the carrier density and velocity respectively. The generated photocurrent is defined as:
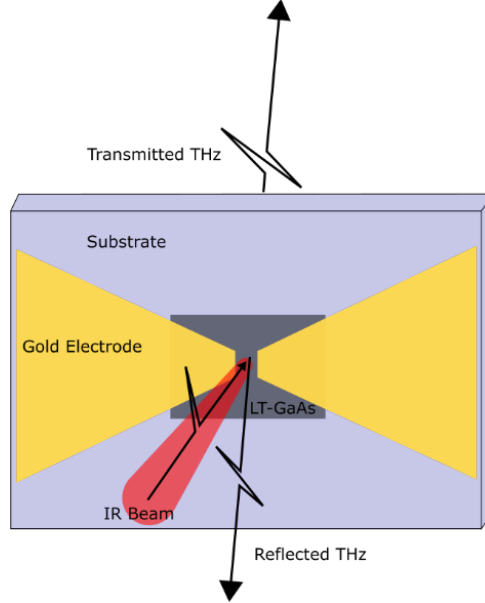
Figure 2.1: A diagram of a photoconductive switch. The gold electrodes are biased to accelerate charge carriers released upon absorption of an incident infrared pulse. These accelerating charge carriers radiate terahertz radiation in all directions which is collected using parabolic mirrors.

$$\frac{\delta J}{\delta t} = en\frac{\delta v}{\delta t} + ev\frac{\delta n}{\delta t} \tag{2.1.2}$$

Where e is the carrier charge, v is the carrier velocity and n is the carrier density. This means that the waveform of the emitted THz radiation depends on several factors including both the incident laser pulses and the characteristics of the material used for the semiconducting layer. As shown in Figure 1.2, the THz signals measured in the time domain (TD) in this work consist of a large positive peak followed by a large negative peak and finishing with a series of oscillations. The laser pulsewidth and intensity control the magnitude of the positive peak, owing to the initial production and acceleration of charge carriers only occurring during illumination. The subsequent peak's magnitude and shape is related to the substrate composition, such as its resistivity, breakdown voltage and carrier lifetime. Having a high resistivity and breakdown voltage minimizes heating effects of dark current owing to the bias and allows for greater bias magnitudes, increasing the overall photocurrent generated across the gap [46, 70]. This is important for increasing the maximum incident optical fluence or electrical bias across the PC switch before the device breaks down. The width of the negative peak is dependent on the lifetime of the carriers, as shown in Figure 2.2. Controlling this parameter is important as the width of the peaks has a direct impact on the bandwidth available in the frequency domain (FD).

PC switches are limited in output owing to carrier screening, where the induced photocurrent generates its own electric field owing to the separation of charges, which interferes with the external electrical bias field. This results in saturation of the output THz power, and increasing the incident optical fluence further can result in critical dam-
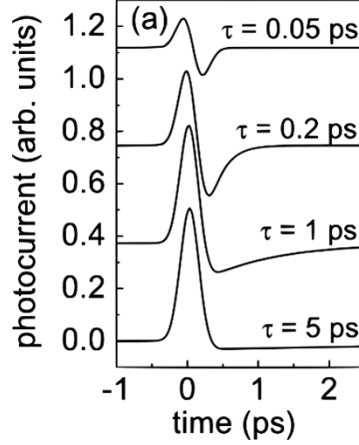
Figure 2.2: Calculated photocurrent with different carrier lifetimes. Adapted from Winnerl *et al.* [71]. Whilst the peak to peak magnitudes are similar for each pulse, their differing shape has an effect on the bandwidth in the frequency domain.
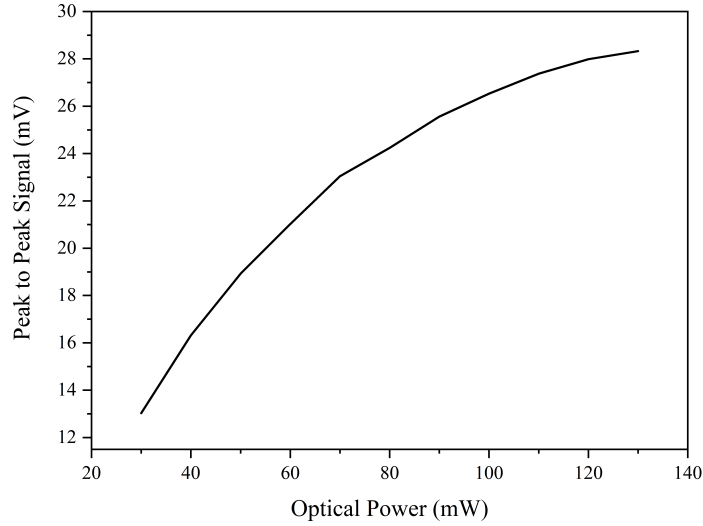
Figure 2.3: An example of saturation in a photoconductive switch as optical power is increased. Further increases in the incident optical power would result in permanent damage to the device.

age to the PC switch [72] owing to heating and electrical breakdown. This is shown in Figure 2.3 where the flattening of the curve indicates that the PC switch is close to breakdown and further increases in optical power will result in permanent damage and effective destruction of the PC switch.

These PC switches can also be used in reverse as detectors which involves the same femtosecond optical source as for generation but with no external bias across the gap, as the incoming THz field provides the field to accelerate the generated charge carriers. The induced photocurrent is proportional to the strength of the THz electric field at a given time and by using a mechanical delay line, that alters the length of the optical pulse path, the field strength across the whole THz waveform can be measured. This results in a high signal-to-noise (SNR) ratio owing to the coherent nature of the incoming THz.

The semiconductor used in this work is Low Temperature Grown (LT)-GaAs, but
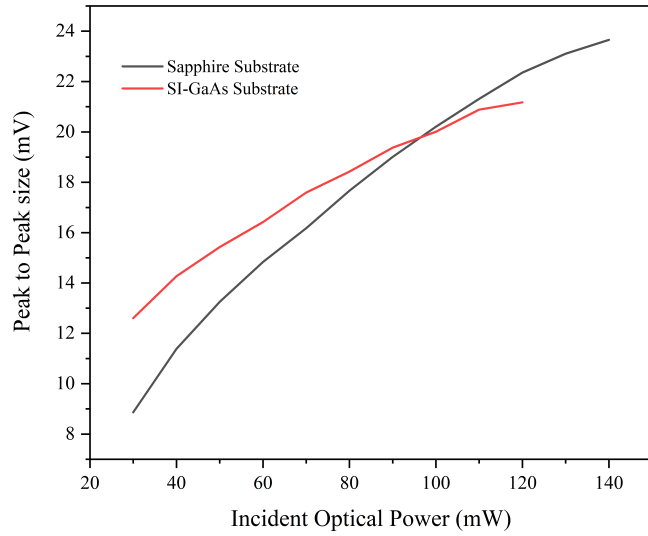
(a) *The peak to peak amplitudes of the sampled waveforms with increasing incident optical power for 20 μm emitters.*
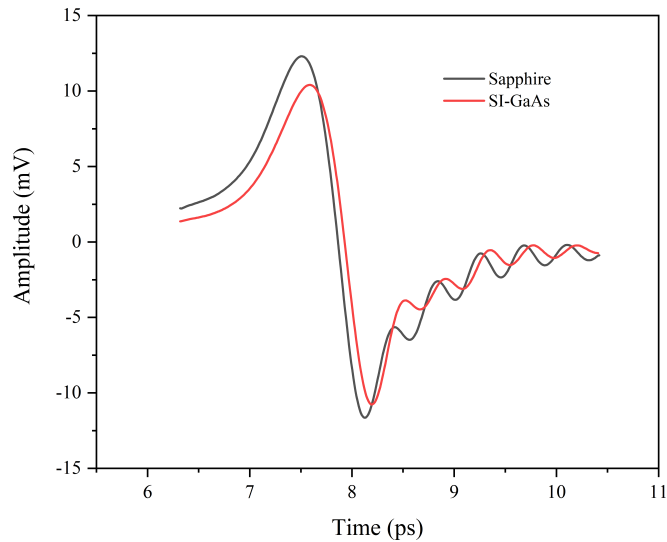
(b) *The time dependent amplitudes for each emitters at their maximum incident optical power, which was 120 and 130 mW for SI-GaAs and sapphire respectively.*

Figure 2.4: The peak to peak amplitudes of the THz waveforms and the TD waveforms for each emitters maximum power. The emitters are on sapphire and SI-GaAs substrates and the gap size for each is 20 μm. The smaller amplitude and lower tolerance for higher optical powers in the case of the SI-GaAs substrate emitter is clear to see.

(a) *Front-side illumination of a PC switch.*   **(b)** *Back-side illumination of a PC switch.*
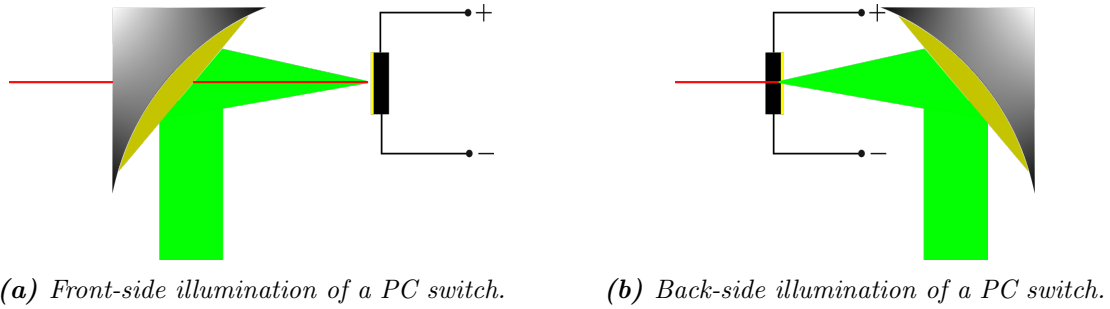
Figure 2.5: Schematic showing front and back-side illumination of a photoconductive switch.

many others have been used [69, 73–78]. LT-GaAs has been used as it contains As clusters which act as trapping sites, significantly reducing carrier lifetimes [79]. These can be increased through annealing up to $600\,°\text{C}$, which increases the size and frequency of these clusters [80]. Winnerl *et al.* [71] demonstrated that when using SI-GaAs, which has a significantly longer carrier lifetime of several hundreds of picoseconds compared to $\sim\!300\,\text{fs}$ in LT-GaAs, the second peak in the THz trace disappeared. This reduces the overall signal magnitude, resulting in a lower SNR. Originally, the LT-GaAs was grown onto a semi-insulating (SI) GaAs substrate but this did not generate particularly high electric field strengths and was vulnerable to severe damage from over-biasing [81]. This is owing to the lower electrical resistivity of the SI-GaAs substrate which resulted in a higher dark current and overheating when large biases and optical fluences are used. Several replacements have been found, including quartz [81], one of the most successful being sapphire [73, 82]. This is demonstrated in Figure 2.4, where the difference between substrates is clear. Sapphire has a much higher electrical resistivity, meaning that the switches are now less at risk of damage from higher voltages, and larger field strengths can be obtained. THz losses are much less significant than in SI-GaAs, and as it is transparent to $800\,\text{nm}$ light, "backside" illumination is now possible. This is where the optical beam travels through the sapphire to the LT-GaAs, and the produced THz radiation is collected with minimal losses through the substrate and is shown in Figure 2.5. This maximises bandwidth and SNR which, with increased field strength, are all desirable attributes for THz spectroscopy [81].

The materials themselves are not the only controlling factor for the magnitude and maximum operating parameters of a PC switch. Reducing the size of the electrode gap both increases the carrier generation efficiency [83], resulting in a higher THz signal, and decreases the breakdown voltage [84], lowering the maximum operational fluence or applicable electrial bias. Thus, a compromise is required resulting in a typical gap size on the order of 10–$100\,\mu\text{m}$, but in some cases up to $200\,\mu\text{m}$ [81].

2.1.2 Electro-Optic Crystals

Whilst PC switches were the primary method of THz generation and detection throughout this work, another method of generation and detection which was also utilised is to use an electro-optic (EO) crystal [47], such as of ZnTe, as shown in Figure 2.6. This utilises a phenomenon called the Pockel's effect [85] where an electric field induces a birefringence in the non-linear crystal. This is when a material's refractive index is dependent on the propagation direction and polarisation of incoming light. This birefringance causes the incoming linearly polarised optical beam to become slightly elliptically polarised. The transmitted beam is then directed through a quarter-wave ($\lambda/4$) plate which is rotated so that if no THz radiation is incident on the non-linear crystal, the beam transmitted through the $\lambda/4$ plate would be circularly polarised. The beam is then finally split into orthogonal x and y components a using a Wollaston prism. As the beam when no THz beam is present is circularly polarised these x and y components are equal and the difference signal between them is 0. When THz radiation is incident on the non-linear crystal this causes the transmitted beam to be elliptical and a difference is seen between the x and y components of the beam. This difference is directly proportional to the applied THz electric field and by scanning the time delay between the THz and laser probe beam the full electric field of the THz pulse can be mapped.

The difference in intensity between the two orthogonal components is detected using a pair of balanced photodiodes which are connected to a lock-in amplifier. The THz electric field can be calculated from this using:

$$I_y - I_x = \frac{I_0 \omega L}{c} n_0^3 r_{41} E_{THz} \tag{2.1.3}$$

Where I_y and I_x are the optical intensities on each diode, I_0 represents the beam intensity with no THz signal, ω is the angular frequency and n_0 is the refractive index of the crystal at $800\,\text{nm}$. L is the length of the EO crystal, r_{41} is the linear EO coefficient, which is material dependent, and c is the speed of light in a vacuum. The principle can also be used in reverse to generate THz radiation. Owing to the differing propagation speeds of different frequencies of light through a medium, the optical and THz pulses will
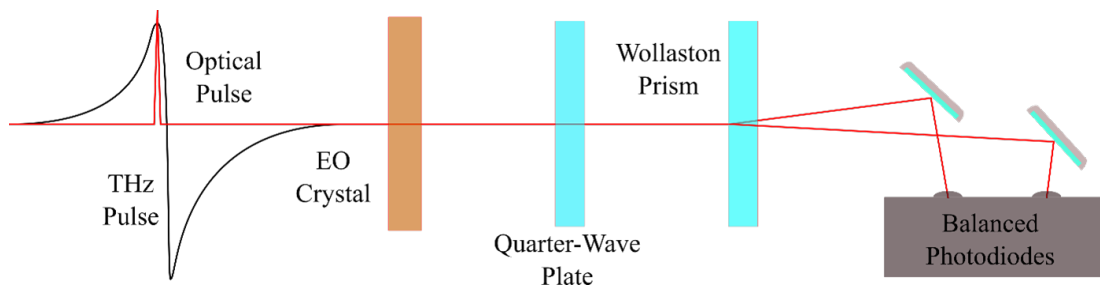
Figure 2.6: A schematic showing the process of detection using an electro-optic crystal.

14

interfere destructively if overlapping over a particular distance. This distance is called the coherence length and is dependent on the relative refractive index at the optical and THz frequencies. At higher frequencies the coherence length is shorter which results in a drop off in spectral bandwidth for thicker crystals. This can be counteracted by using thinner crystals but these are both harder to align and are more fragile. This results in a trade-off between spectral bandwidth and ease-of-use of the device when using EO crystals for broadband spectroscopic purposes and so these tend to be used for narrow-band applications [86]. They have been used in this work in Chapter 6 as detectors.

2.2 Terahertz Time-Domain Spectroscopy

2.2.1 Terahertz Time-Domain Spectroscopy Systems Used in this Work

In this work, three THz-TDS set-ups have been used and whilst there are some variations between the generation, detection and data processing methods, only one was used for producing THz-TDS spectra. This will be referred to as System 1 and will be described in the most detail and will be the example system used to describe THz-TDS in general. System 2, which was used for testing PC switches and the specifications for System 3, which is still under construction, will be described further in Chapter 6.
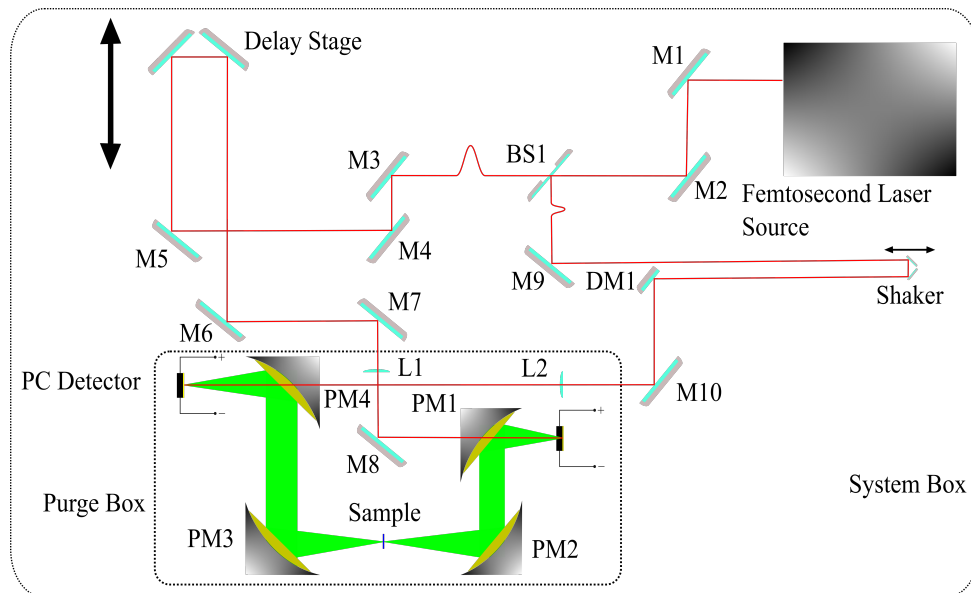
Figure 2.7: Schematic of System 1 which was used for taking the terahertz absorption spectra of α-Lactose Monohydrate.

System 1 is shown in Figure 2.7 and can be considered a typical THz-TDS set-up. The optical 800 nm pulses are provided by a mode-locked Ti:sapphire laser (Vitara, Coherent) that produces repeating 20 fs pulses, centred at 800 nm, with a repetition rate of 80 MHz.

This main pulse train was focused onto a LT-GaAs PC switch with a 5 mm thick quartz substrate and a gap size of 100 μm. This was biased at 350 V with a 7 kHz modulation frequency using a 50% duty cycle for lock-in detection. After the emitted THz radiation was collected, collimated and focused through the sample, it was recollected and focused onto another PC switch with the same parameters as the emitting PC switch. The induced current in the detecting PC switch was amplified using a gain of 20 nA V^{-1}. The time constant for the sampling rate was typically 1 ms and the sensitivity of the lock-in was typically set to 0.01 V. The spectrum was constructed from the average of 60 scans with a frequency resolution of 0.01 THz. Owing to the thickness of the emitter there were no system reflections in the selected scan range. This is owing to the primary reflection coming from the substrate containing the emitter and when this substrate is thick enough, this reflection occurs far away enough in time so as not to obscure any temporal features of the THz pulse. The sample and THz beams were kept under a dry nitrogen atmosphere. Low temperature measurements were performed by mounting the sample pellet onto a coldfinger of a continuous-flow helium cryostat (MicrostatHe, Oxford Instruments) which has a pair of polymethylpentene (TPX) windows.

2.2.2 Sample Preparation

All samples were purchased as powders rather than single crystals and were mixed, usually with a low mass ratio, with Polytetrafluoroethane (PTFE). This was compressed into a pellet with an approximate thickness of 500 μm using a mass of 10 t, which is a force of approximately 98 000 N. The true thickness of the pellet *in situ* is determined from the THz spectral measurement and this will be discussed in Section 2.3.5. This process is done owing to the significant absorption of THz radiation of a wide range of materials which reduces the effective bandwidth of the spectrum. By diluting the samples in a material such as PTFE, which is very weakly-absorbing in the THz region, the effective bandwidth of the system can be extended.

2.2.3 Challenges of Terahertz Time-Domain Spectroscopy

Owing to the nature of this detection technique, for a given position of the mechanical delay line, a discrete value of the THz waveform is sampled. By varying the length of the pump beam with respect to the probe beam, which alters the arrival time of the optical pulses, the entire waveform can be sampled. The reverse set-up, where the delay line is active on the probe beam is also possible. In this work, the delay line moves at a constant velocity and samples periodically for a given time constant. Owing to errors produced through sampling while the stage is moving at a constant velocity, a data-set that is not constantly separated in time is produced and so these values are interpolated to give a

set of values that are. As multiple scans of both the reference and the sample are taken, these are averaged in the TD. This improves SNR ratio by reducing noise with this effect increasing asymptotically with respect to the number of scans [87]. For most systems considered in this work, 60 scans has been selected as the optimum compromise between SNR and measurement time. The collected waveform is constructed by assuming that each emitted THz waveform is identical between the incident optical pulses on the emitter and that conditions are constant throughout the measurement. This assumption will not remain true if factors like laser power or humidity are not kept constant but owing to the set-up used these factors are able to be controlled or accounted for. Humidity is monitored by a hygrometer and measurements are performed at $< 1\%$ humidity, utilising a purge box pumped with dry air or nitrogen. The Ti:sapphire crystal is temperature-controlled to minimise the effects of heating on the output and is left to stabilise for at least an hour after being switched on before any measurements are taken. As THz signals can vary over several orders of magnitude in amplitude, measures must be taken to improve SNR. A widely utilised method is using a lock-in amplifier, which requires a reference frequency. The electrical bias applied to the emitter is electrically chopped using a square wave resulting in both the propagating wave and the detector output being modulated at the chopping frequency, which is widely utilised method of amplifying signals.

2.3   Extraction of Spectroscopic Parameters

Originally, the earliest function a THz transmission system could perform was detection of water vapour [88], owing to strong absorptions at these frequencies. This then progressed to using traditional methods such as the Beer-Lambert Law [89] where the absorption of the sample is related to its concentration. This section details how to extract the desired spectroscopic parameters from the sampled electric field. An overview is depicted in Figure 2.8.

The process about to be summarised was developed and described in significant detail by Greenall [90]. The first step is to average and window the TD data, upon which a discrete Fourier Transform (FT) is performed. The sample data is divided by the reference data to calculate the transfer function, H. The transfer function is a quantitative representation of the spectroscopic system. The phase component of H, $\angle H$, is used to calculate the real refractive index which in turn allows the calculation of the magnitude of the transfer function, $|H|$. Finally, this is used to calculate the absorption coefficient using the method described below [90].

2.3.1 Relationship Between Spectroscopic Parameters

The refractive index of a sample, n, is the ratio between the phase propagation velocity in the medium and in a vacuum. As frequency is held fixed, this results in changes to the wavelength of the incident wave. When a wave propagates through a sample, some of the energy of the wave is absorbed and the wave is attenuated. The degree of attenuation is described by the frequency dependent extinction coefficient, κ, which is related to n by:

$$\tilde{n} = n - i\kappa \tag{2.3.1}$$

Where $\tilde{n}$ is the complex, frequency dependent refractive index. κ describes the attenuation of the amplitude per unit length, but is used less frequently in a chemical setting than α, which is the absorption coefficient and is related to κ by:

$$\alpha = \kappa \frac{2\omega}{c} \tag{2.3.2}$$

Where ω is the angular frequency and c is the speed of light in a vacuum. A dielectric can generally be modelled as an array of charges bound in various ways to a structure. For example, in an ionic crystalline material, positive and negative ions are arranged in a fixed structure which repeats in 3D. In molecular crystals, the ions are held together with chemical bonds. When an electric field is applied to the dielectric, these charges interact with the field and will displace from their original position, straining the inter and intra-molecular forces that hold the crystal together. If this phenomenon occurs over a significant enough portion of the material, an electric dipole is induced which is proportional to the charge magnitude and displacement. This polarisation is proportional to the permittivity of the sample:
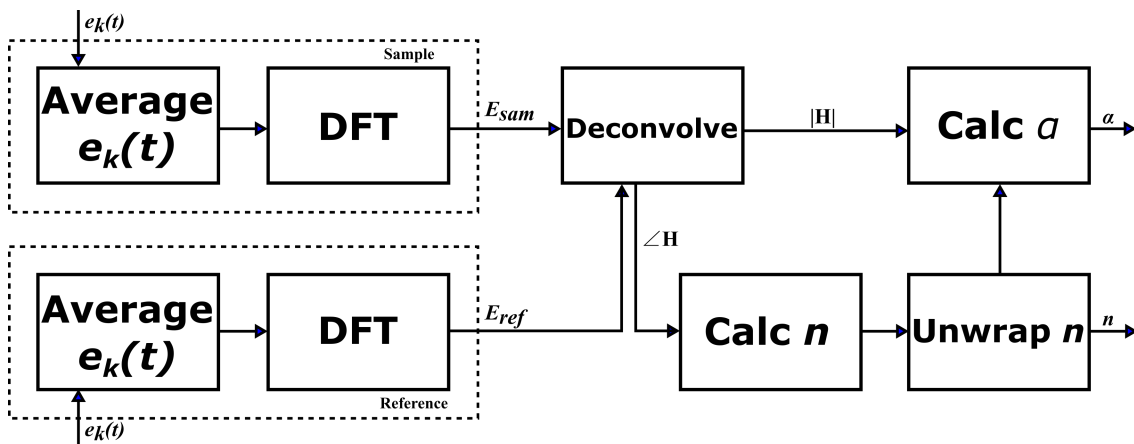
Figure 2.8: An overview of the data extraction process. Time-dependent electric time stamps can be used to calculate the refractive index and then the absorption.

18

$$P = (\tilde{\epsilon} - 1)\epsilon_0 E \tag{2.3.3}$$

Where P is the induced polarisation, $\tilde{\epsilon}$ is the complex permittivity, ϵ_0 is the permittivity of free space and E is the incident electric field. This relationship arises from the coupling of the electric wave to the polarisation of the dielectric, which impedes the wave [89]. Therefore, the complex permittivity is equal to the square of the complex refractive index and so the refractive index is dictated by the polarisation mechanisms in the sample. The relationship between refractive index and permittivity can be expanded to:

$$\tilde{\epsilon} = \tilde{n}^2 = (n - i\kappa)^2 \tag{2.3.4}$$

The complex permittivity can be split into real and imaginary parts too:

$$\tilde{\epsilon} = (\epsilon' - i\epsilon'') = (n^2 - \kappa^2) - i(2n\kappa) \tag{2.3.5}$$

Where ϵ' is the real permittivity and represents the ratio between the capacitance of a vacuum and of a dielectric. ϵ'' is the complex permittivity and describes the energy lost in coupling between the electric field and the dielectric polarisation. Substituting in using Equation (2.3.2), this expression now demonstrates the relationship between permittivity and absorption:

$$\tilde{\epsilon} = \left(n^2 - \frac{\alpha c^2}{2\omega}\right) - i\left(n\frac{\alpha c}{\omega}\right) \tag{2.3.6}$$

2.3.2 Transfer Model

To extract these parameters from the collected data, a model relating them to the transfer function of the system has been developed [91].

When a THz wave reaches an interface, such as the sample's edge, a fraction of the THz radiation is reflected whilst the rest propagates through, as shown in Figure 2.9a. The ratio between these components is the transmission coefficient, $T_{1,2}$, and is dictated by the relative refractive indices of the two mediums, $\tilde{n}_1$ and $\tilde{n}_2$. This is calculated by:

$$T_{1,2} = \frac{2\tilde{n}_2}{\tilde{n}_1 + \tilde{n}_2} \tag{2.3.7}$$

The transmitted THz radiation will then propagate through the material. In most suitable materials, the THz radiation will be attenuated and will undergo a phase shift.
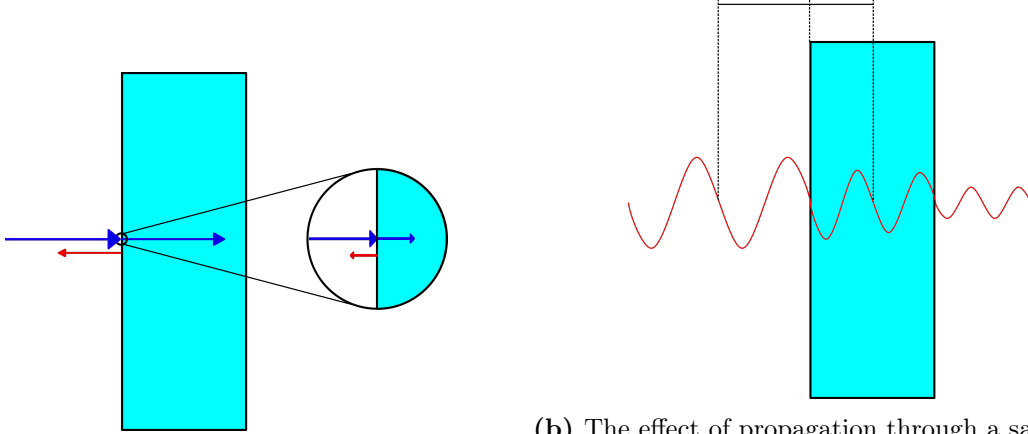
(a) A model of a THz pulse interacting with a sample's surface. Most of the pulse is transmitted but a small amount is reflected.

(b) The effect of propagation through a sample on a THz wave (depicted as a sine wave for clarity). The wavelength decreases as the wave velocity decreases and the wave is attenuated.

Figure 2.9: The process of extracting peak properties from the experimental terahertz absorption spectrum.

This can be seen in Figure 2.9b, where the incident wave has a greater amplitude and wavelength than the final wave. The ratio between the final and incident THz waves, which is often complex, is the propagation coefficient of the sample, P_s. This is thickness dependent, (where l is thickness), and is calculated by:

$$P_s = e^{-i\frac{\omega l}{c}\tilde{n}} \tag{2.3.8}$$

As both a sample and reference scan are required, a reference model is also required. An identical THz wave propagates through dry air which will be displaced by the sample. The propagation coefficient, P_A, is identical to P_S except that $\tilde{n} = 1$. These equations combine to provide a sample model:

$$E_{sam} = T_{A,S}P_S T_{S,A}E_0 H_{sys} \tag{2.3.9}$$

Where $T_{A,S}$ and $T_{S,A}$ are the air-sample and sample-air transmission coefficients respectively, E_0 is the incident THz radiation and H_{sys} is the instrument transfer function. A similar model can be produced for the reference:

$$E_{ref} = P_A E_0 H_{sys} \tag{2.3.10}$$

E_0 and H_{sys} are constant over both sample and reference measurements, and so when combined these should cancel out. In practice, this is not the case and this will be discussed further below when discussing reflections. By normalising the sample against the reference, the model transfer function, without considering reflections within the sample, will be:

$$H = \frac{E_{sam}}{E_{ref}} = T_{A,S}\frac{P_S}{P_A}T_{S,A} = \frac{4\tilde{n}}{(\tilde{n}+1)^2}e^{-i\frac{\omega l}{c}(\tilde{n}-1)} \qquad (2.3.11)$$

2.3.3   Extraction of Refractive Index and Absorption

By using simple assumptions which are valid whilst resonance does not occur in the sample, it is possible to derive expressions for the refractive index, n and extinction coefficient, κ, individually. In most relevant cases it can be assumed that the phase change over the measurement primarily occurs during propagation. This permits an expression in which the phase of the model transfer function can be equated to solely the propagation terms:

$$\angle H = \angle\frac{P_S}{P_A} = -\frac{\omega l}{c}(n-1) \qquad (2.3.12)$$

From this, n can be approximated as real and is calculated, and an expression for $|H|$ can be formed:

$$|H| = \frac{4n}{(n+1)^2}e^{-\frac{\omega l}{c}\kappa} \qquad (2.3.13)$$

This is inverted to form an expression in terms of κ, from which α can be calculated using Equation (2.3.2):

$$\kappa = \frac{-c}{\omega l}ln\left(|H|\frac{(n+1)^2}{4n}\right) \qquad (2.3.14)$$

2.3.4   Dynamic Range

As with all spectroscopic systems, there is an operating frequency range where signals below or above will not be detected. In addition to this, at frequencies close to the ends of this range, the detector noise will obscure signals owing to their low relative amplitude. This culminates in a noise floor, where detector noise completely obscures any measured signal. By normalising a reference measurement against the Root Mean Squared (RMS) of the noise floor, referred to as the dynamic range of the system, the frequency-dependent maximum absorption, α_{max}, of the system for a specific sample can be determined. This means that signals less than this maximum absorption can be considered to be accurate, but any that are greater will be distorted by detector noise, providing an effective bandwidth for the system. This is shown in Figure 2.10.
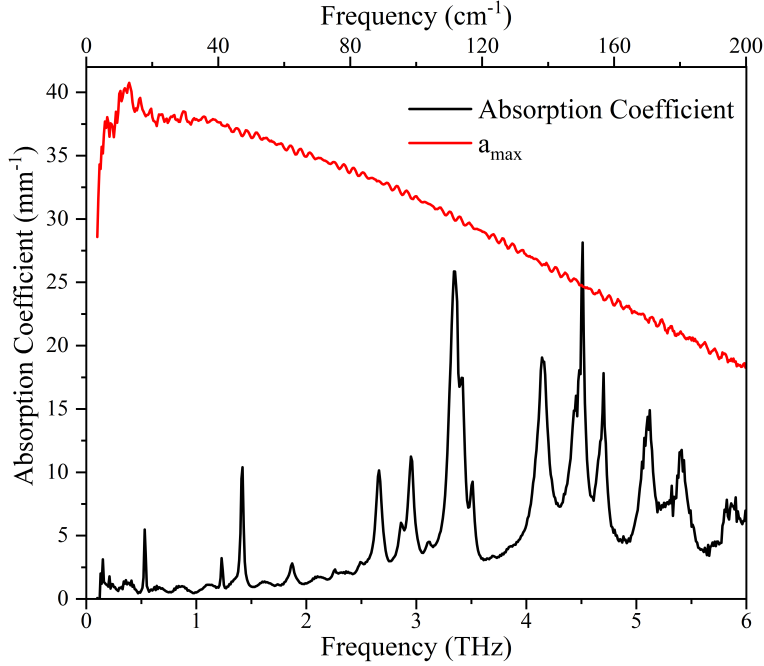
Figure 2.10: The absorption spectrum of α-Lactose Monohydrate with the corresponding maximum absorption of the system. The oscillations in the base absorption of the spectrum are called etalons. These are a consequence of reflections and will be discussed in Section 2.3.5.

2.3.5   Sample Reflections

Until this point, the model assumes that there is a single reflection that propagates in the reverse of the incident direction and does not reach the detector. This assumption can be correct if a time window is used to truncate out reflections, which can be done for thick, weakly absorbing samples. However, for a significant proportion of samples measured the first reflection can be present close enough to the main pulse that truncating them would result in either loss of frequency resolution or spectral information about the low frequency modes of the system. So spectral information is not lost, the model described above must be expanded to include these sample reflections.

If the reflection or reflections do not overlap with the oscillations from the main pulse, a window function is used to truncate the data so as to discard the reflection. In this work, a Tukey window is used which is a rectangular window function but with a cosine roll-off.

As shown in Figure 2.11, the window function allows removal of reflections whilst maximising frequency resolution. If the reflections are not removed, they produce artefacts in the measured parameters called etalons, which can be seen in Figure 2.10. As the reflection is localised in time, this results in a sinusoidal error term in the extracted refractive index that is dependent on frequency [90]. This propagates through to the rest
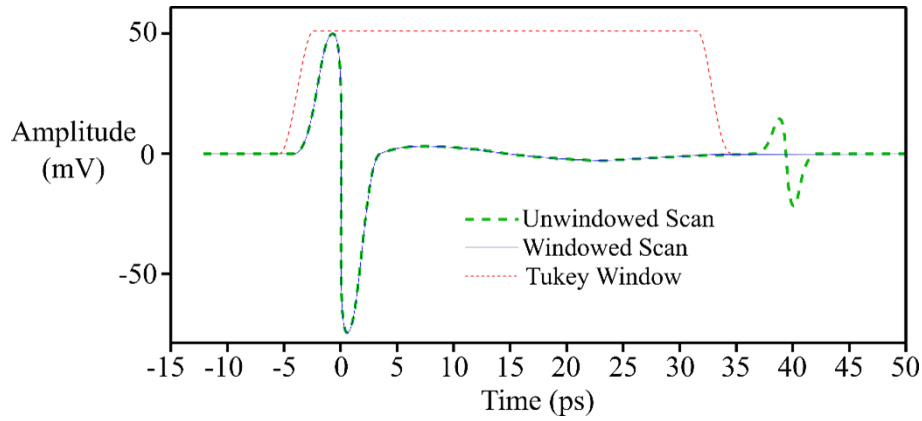
Figure 2.11: A graph depicting a Tukey window and its effect on the time-domain data.
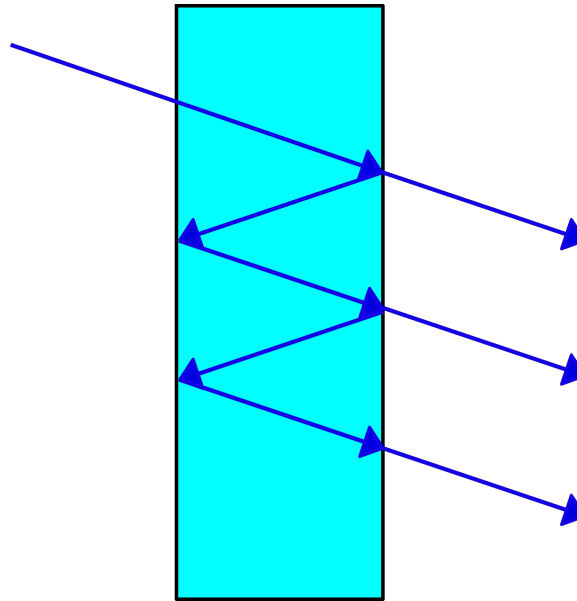
Figure 2.12: The sample model updated to include reflections. Each time a sample-air interface is reached, a reflection occurs. The incident path has been offset for clarity but should be imagined as travelling perpendicular to the sample's surface.

of the spectral parameters as they are calculated from the refractive index. The reflections can arise both from the sample or the system itself, from the emitter, detector or other optics in the beam path as each interaction with a material-air interface will cause a reflection.

Incorporating Reflections into Model

The assumptions about the sample and the beam are still held true, except that there is now a reflection each time the pulse reaches a sample-air interface. This creates a resonance within the sample, as shown in Figure 2.12, where the beam has been directed at an angle for clarity. In reality, the beam is travelling perpendicular to the sample's surface, as before. Each transmitted pulse appears as a delayed, attenuated copy of the

t
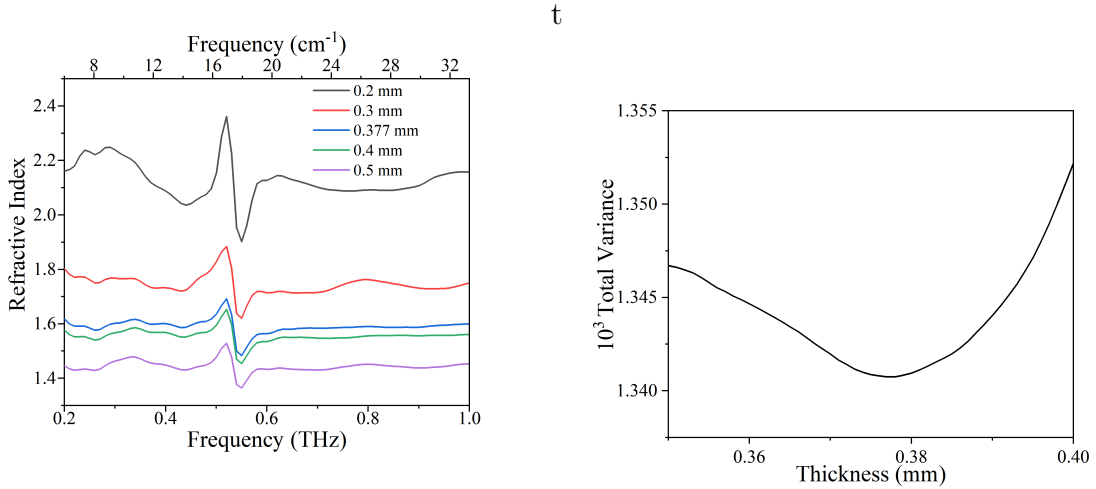
(a) *Various refractive index values at different frequencies for different simulated thicknesses.*

(b) *The Total Variance plotted against Thickness.*

Figure 2.13: The effect of different thicknesses on the refractive index values and the thickness extraction curve. In (a), a wide range has been plotted for clarity. In practice, a much smaller range of thicknesses is considered as shown in (b). The minimum corresponds to the thickness of the pellet.

original pulse, and their separation depends on the thickness and refractive index of the sample. The reflection coefficient of the system must now be considered, and is described by:

$$R_{1,2} = 1 - T_{1,2} = \frac{\tilde{n}_2 - \tilde{n}_1}{\tilde{n}_2 + \tilde{n}_1} \tag{2.3.15}$$

This can be incorporated into expression for the model derived above, producing:

$$H = T_{A,S}\frac{P_S}{P_A}T_{S,A}(1 + R_{S,A}^2 P_S^2) \tag{2.3.16}$$

Which represents the original pulse transmitting entirely through the sample and an additional pulse that has reflected off the sample-air interface and propagated through the sample twice. Adding more reflections to the model is done by multiplying by $(1 + R_{S,A}^2 P_S^2)$ for however many reflections are being considered. Whilst this model reduces etalons in the extracted parameters, they are not completely removed owing to uncertainty in the thickness measurement, and the degree of reduction is proportional to frequency.

Thickness Extraction

An additional feature of this model is that it can be used to iteratively extract the thickness of the sample itself. This is critical in circumstances where a direct measurement of the sample is not possible, such as cryogenic experiments. A starting thickness is either assumed or measured and the steps detailed above are carried out. A range of sensible thicknesses are selected and the steps above are iterated through for each thickness.

24

This produces a range of refractive index datasets, most of which will contain significant spectral artefacts.

By trying to minimise the total variance of the spectrum of the real refractive index, the optimal thickness can be selected. This corresponds to the smoothest trace in Figure 2.13a, but not all etalons can be removed this way. This method is used in Chapter 4 to extract the temperature-dependent thickness of a pellet of αLM.

2.4   Conclusion

This chapter has described a variety of THz generation and detection methods, focusing specifically on PC switches and EO crystals. Additionally, the process behind and the main system used for THz-TDS in this work was described, as was the process of extraction spectroscopic parameters and some of the challenges behind this.

Chapter 3

Density Functional Theory and its Applications for Vibrational Spectroscopy

3.1 Introduction

Owing to the complicated and varied nature of phenomena in the THz range, interpretation of the measured spectral properties requires calculation of the nature, frequency and intensity of the underlying modes. These, in turn, are calculated from the electronic ground state of the system. This is achieved by solving the many-body Schrödinger equation (MBSE), which is shown in Equation (3.1.1), and in this work this will be achieved using Density Functional Theory (DFT) [92].

$$\left(-\frac{1}{2} \sum_i \boldsymbol{\Delta}_i + \sum_i \boldsymbol{V}(\mathbf{r}_i) + \sum_{i \neq j} \frac{1}{|\mathbf{r}_i - \mathbf{r}_j|} \right) \boldsymbol{\Psi}(\mathbf{r}_1, ..., \mathbf{r}_N) = \boldsymbol{E}\boldsymbol{\Psi}(\mathbf{r}_1, ..., \mathbf{r}_N) \qquad (3.1.1)$$

$\boldsymbol{\Delta}_i$ is the Laplace Operator acting on atom i, $\boldsymbol{V}(\mathbf{r}_i)$ is the potential energy, $\mathbf{r}_i$ is the nuclear coordinates, $\boldsymbol{\Psi}$ is the wavefunction and $\boldsymbol{E}$ is the energy of the system. Initially, DFT was only used for very simple and uniform systems such as metals but development over the last few decades has enabled its use in far more complicated systems and studying chemical phenomena, such as pharmaceutically relevant compounds [93], phase transformations in crystal structures [94, 95], nanomaterial properties [96] and amino acids [97]. Other methods have been developed for attempting this and are widely used in the context of an isolated molecule in the gas phase. Whilst they can be used for periodic systems, they either tend to not match experimental data or become extremely

expensive computations that can be unfeasible for large systems.

This chapter will describe DFT and the methodology of applying it to useful chemical systems, followed by a description of the software packages, general procedure and calculation parameters used.

3.2 Density Functional Theory

3.2.1 Solving the Many Body Schrödinger Equation

Underpinning most quantum mechanical theories, DFT also uses the Born-Oppenheimer approximation which states that any motion of a nucleus is much slower than the motion of an electron. This allows for an instantaneous response by the electron to the nucleus and as such, nuclei are treated as fixed in space, reducing the number of contributions to the total energy of the system. Attempting to solve the MBSE is too complex for all but the smallest systems so a number of simplifications have been developed over the years. In particular, the electron orbitals are defined to be one-electron non-interacting orbitals where:

$$\mathbf{\Psi}(\mathbf{r}_1, ..., \mathbf{r}_N) \rightarrow \{\psi_1(\mathbf{r}), \psi_2(\mathbf{r}), ..., \psi_N(\mathbf{r})\} \tag{3.2.1}$$

$$\mathbf{\Psi}(\mathbf{r}_1, ..., \mathbf{r}_N) = \prod_i^N \psi_i(\mathbf{r}_i) \tag{3.2.2}$$

These assumptions allow the separation of the total energy of the system, $\boldsymbol{E}_{tot}$, into the following terms:

$$\boldsymbol{E}_{tot} = \boldsymbol{E}_{KE} + \boldsymbol{E}_H + \boldsymbol{E}_Z + \boldsymbol{U}_Z + \boldsymbol{E}_{XC} \tag{3.2.3}$$

where $\boldsymbol{E}_{KE}$ is the kinetic energy of the electrons, $\boldsymbol{E}_H$ is the Hartee energy which is the Coulombic potential energy, $\boldsymbol{E}_Z$ is the potential energy between the electrons and the nuclei, $\boldsymbol{U}_Z$ is the potential energy between the nuclei and $\boldsymbol{E}_{XC}$ is the correlation exchange energy between the electrons. As these electron orbitals are non-interacting, each one has its own associated coordinate system in three dimensions. This results in a calculation that increases in magnitude as more electrons were added, which meant that calculations involving large amounts of electrons slowed down dramatically. Kohn, Honenburg and Sham [92, 98] developed a method that attempted to solve this. By defining each term in Equation (3.2.3) as a functional dependent on the electron density, ρ, the number of coordinates that needed to be calculated was reduced from $3N$ to three. The total energy

of the system can now be represented as:

$$\boldsymbol{E}[\rho] = \boldsymbol{E}_{KE}[\{\psi_i[\rho]\}] + \boldsymbol{E}_H[\rho] + \boldsymbol{E}_Z[\rho] + \boldsymbol{U}_Z[\rho] + \boldsymbol{E}_{XC}[\rho] \tag{3.2.4}$$

The electron density is calculated using one electron orbitals, represented using basis sets, which are shown by:

$$\boldsymbol{\rho}(\mathbf{r}) = \sum_i^{\boldsymbol{N}} |\psi_i(\mathbf{r})|^2 \tag{3.2.5}$$

This allows orbitals to be calculated as a linear combination of atomic orbitals and this is discussed further in Section 3.2.2 and Section 3.2.3. The Kohn-Sham equation, which is a modified MBSE, is used to calculate these one electron orbitals with:

$$\left(-\frac{1}{2}\boldsymbol{\Delta} + V_z(\mathbf{r}) + V_H[\rho](\mathbf{r}) + V_{XC}[\rho](\mathbf{r}) \right) \psi_i(\mathbf{r}) = \epsilon_i \psi_i(\mathbf{r}) \tag{3.2.6}$$

Each term can be calculated exactly with the exception of the final term, $V_{XC}[\rho]$. This is the exchange correlation energy and represents the interaction between the electrons. These are described as functionals and there are many possible approximations for this, the simplest being the Local Density Approximation (LDA) [99]. This is where the electron density is assumed to be homogeneous. More complex functionals incorporate the gradient of the electron density as well and the simplest of these is called the Generalised Gradient Approximation (GGA) [100]. These can often be broken into separate exchange and correlation components that can be mixed to form new functionals such as meta-GGAs [101] and hybrid functionals such as B3LYP [102]. B3LYP is often used by the chemical community for small molecules but is computationally expensive. In this work, a version of GGA developed by Perdew *et. al.* [103] has been used throughout this work and is referred to as the Perdew-Burke-Ernzerhof (PBE) functional. This is a relatively simple functional that this group has previously shown can provide accurate results and is computationally efficient when compared to hybrid and meta functionals.

3.2.2 Periodic Systems

Whilst simplifying the MBSE drastically decreases the magnitude of the calculation, for crystals and other extended systems further simplification is needed as the number of electrons is still on the order of approximately 10^{23}. This is done by considering that the unit cell, the smallest infinitely repeating section of the crystal, must have the same orbitals at the same position in the unit cell regardless of where that is in the crystal. This is described by:

$$\psi_{n\mathbf{k}}(\mathbf{r} + \mathbf{R}) = \psi_{n\mathbf{k}}(\mathbf{r})e^{i\mathbf{k}\mathbf{R}} \tag{3.2.7}$$

$$\psi_{n\mathbf{k}}(\mathbf{r}) = u_{n\mathbf{k}}(\mathbf{r})e^{i\mathbf{k}\mathbf{R}} \tag{3.2.8}$$

$$u_{n\mathbf{k}}(\mathbf{r} + \mathbf{R}) = u_{n\mathbf{k}}(\mathbf{r}) \tag{3.2.9}$$

where $\mathbf{R}$ is any lattice vector, n is the band index and $\mathbf{k}$ is the Bloch vector, where orbitals are calculated at each Bloch vector. These Bloch vectors are described in the reciprocal lattice, u, which represents the Fourier Transform of the physical lattice. The first Brillouin Zone (BZ) represents the primitive cell in this reciprocal space and these Bloch vectors are constrained to this area. The centre of the BZ is called the 'Gamma' point, typically Γ-Point, and only phonons involved with this centre are IR-active. The most desired parameters are extracted by integrating over the BZ:

$$\rho(\mathbf{r}) = \frac{1}{\Omega_{BZ}} \sum_n \int_{BZ} f_{n\mathbf{k}} |\psi_{n\mathbf{k}}(\mathbf{r})|^2 d\mathbf{k} \tag{3.2.10}$$

where Ω_{BZ} is a constant dependent on the lattice and $f_{n\mathbf{k}}$ are the Fourier component of the integration. This is costly and unnecessary as orbitals that are close together are typically identical or very similar. This means the integral can be replaced by a weighted sum over a grid of points and these points are called k-points. In this work, each calculation used the Monkhorst-Pack [104] method for the description of k-points. The number of points required can be further reduced through symmetry operations and this reduced calculated area is called the irreducible BZ. The equation becomes:

$$\rho(\mathbf{r}) = \sum_{n\mathbf{k}} \omega_{\mathbf{k}} f_{n\mathbf{k}} |\psi_{n\mathbf{k}}(\mathbf{r})|^2 d\mathbf{k} \tag{3.2.11}$$

where $\omega_{\mathbf{k}}$ is a weighting factor. The number of these points can be reduced for calculation speed and increased for computational accuracy and the details of how these were chosen for the calculations in this thesis will be discussed in Section 3.3.1.

For single molecule calculations performed by those in the chemical community, the molecular orbitals themselves are typically represented by basis sets that are constructed from localised functions centred around each atomic nucleus [105]. These can be Slater Type Orbitals (STO), which have the form $r^n e^{-\zeta r}$ or Gaussian Type Orbitals (GTO), which have the form e^{-r}. STOs typically are better at representing the shape of the wavefunction but are more complex to integrate over whilst GTOs are worse at representing the wavefunction but the integral can be more easily calculated. These are generally
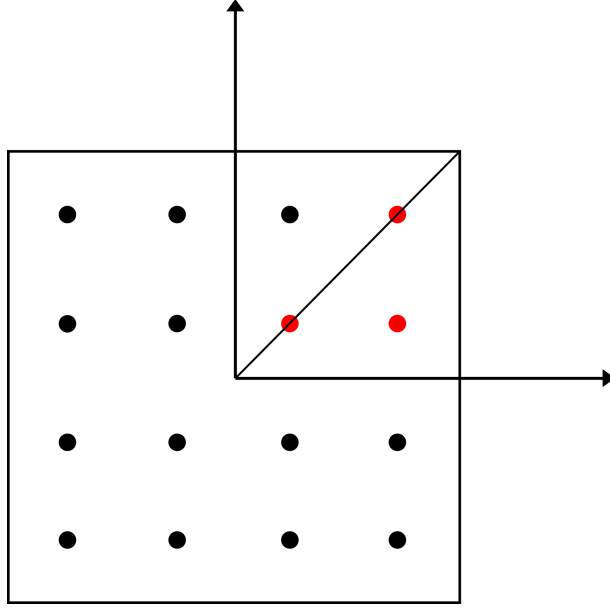
Figure 3.1: A schematic of the BZ. The black dots represent all required k-points and the red dots represent the k-points that can be mapped onto all others using symmetry operations. This is called the irreducible Brillouin Zone.

combined to give hybrid orbitals the smallest of which is STO-3G [106], which combine the advantages of both. Whilst these can be used in solid-state, these can be difficult to implement owing to translational symmetry in the solid. Despite this, these are used by CP2K [107] and Crystal17 [108] but a majority of DFT codes use plane waves. One method of circumventing this has been to use plane waves instead [98]. This gives the wavefunction the form:

$$\psi_{n\mathbf{k}}(\mathbf{r}) = \frac{1}{\Omega^{0.5}} \sum_{\boldsymbol{G}} C_{\boldsymbol{G}n\mathbf{k}} e^{i(\boldsymbol{G}+\mathbf{k})\mathbf{r}} \tag{3.2.12}$$

The reduced cost arises from the easy conversion between reciprocal and real space and the ease of calculating certain parameters in each space, such as the exchange correlation and Hartree potentials:

$$C_{\mathbf{r}n\mathbf{k}} = \sum_{G} C_{\boldsymbol{G}n\mathbf{k}} e^{i\boldsymbol{G}\mathbf{r}} \overset{FFT}{\leftrightarrow} C_{\mathbf{G}n\mathbf{k}} = \frac{1}{N_{FFT}} \sum_{\mathbf{r}} C_{\mathbf{r}n\mathbf{k}} e^{-i\boldsymbol{G}\mathbf{r}} \tag{3.2.13}$$

As with localised basis sets, an infinite number of either is required to exactly represent the wavefunction which is not practical. Whilst the localised basis sets are constructed from a pre-determined number of orbitals, plane waves are constrained by defining a cut-off energy that provides a limit to the maximum energy of any constituent plane wave. Reducing this cut-off energy reduces the accuracy of the calculation but also reduces its cost and the reverse is also true. This parameter is selected on a per-calculation basis and this is discussed further in Section 3.3.1. The key advantage is that one number can

be used to smoothly increase the accuracy of the calculation whereas this is not possible with localised basis sets.

3.2.3 Pseudopotentials

When considering systems that contain elements heavier than He, the electrons that are typically involved in covalent bonding are in outer orbitals called valence orbitals. The remaining electrons are referred to as core electrons and do not take part in any bonding processes. Whilst DFT does not model the electrons themselves, but the electron density, calculating this to a high degree of accuracy for the area in space where these core orbitals will be will not significantly improve the accuracy of the calculation but may significantly increase its computational cost as a much finer mesh of k-points will have to be used. As such, the concept of a pseudopotential was developed to model the core electrons collectively.

Traditional pseudopotentials typically take two forms; 'norm-conserving' and 'ultrasoft'. Norm-conserving pseudopotentials [109] must satisfy two conditions. Firstly, inside a specified cut-off radius, the normalisation of a pseudo-wavefunction should be equal to the normalisation of the all-electron wavefunction. The other condition is that the wavefunctions should be equal outside of this cut-off radius. Ultrasoft pseudopotentials [110] relax this constraint by not requiring that the normalisations of the wavefunctions to be exactly equal. This reduces their computational cost further but at the expense of their ability to be implemented in different chemical environments without testing their suitability. Whilst these were originally developed for localised basis sets, they are also used when modelling the wavefunction using plane waves.

Another approach to this problem is the Projector Augmented-Wave (PAW) method [111]. This works through construction of a transformation operator that can calculate the properties of the all-electron system from the pseudo-wavefunction. These are typically pre-calculated for a given atomic environment and therefore further save computational expense. PAW potentials combine the computationally efficient advantages of pseudopotentials but provide the ability to still calculate the all-electron material properties if required. This can facilitate a lower plane wave cut-off energy than available if you needed to use norm-conserving pseudopotentials. These will be used for all calculations in this work as these are available with VASP [112] and this is the code used in this work.

3.2.4 Calculation of Vibrational Modes

The frequencies and intensities of any phonon modes that are present in the system can be calculated by determining the effect of ion displacement on the energy of the system.

This can be calculated by expanding the energy as a Taylor series with the form:

$$E = E_0 + \frac{\delta E}{\delta u}.u + \frac{1}{2!}\frac{\delta^2 E}{\delta u^2}.u^2 + \frac{1}{3!}\frac{\delta^3 E}{\delta u^3}.u^3 + ... \quad (3.2.14)$$

where E is the total energy of the system, E_0 is the energy of the system at equilibrium and u is the displacement from equilibrium position. When an ion is displaced, each other ion that experiences a force will oscillate around a new equilibrium position. Whilst DFT can be used to calculated any term in Equation (3.2.14), this becomes more computationally expensive for each included term. By assuming the oscillation is harmonic, the harmonic vibrational frequencies can be extracted. The key assumption underpinning this is that at its equilibrium position, movements of an ion will result in a harmonic potential energy distribution. This assumption is called the harmonic approximation. Third order terms and higher are set to be zero in this approximation and do not have to be calculated, but contain information about any anharmonicity in the system. These can be important in a wide range of systems and conditions and this will be discussed further in Chapter 5.

At this new equilibrium position, the gradient of the potential energy is zero and so the first term in Equation (3.2.14) becomes zero. The energy now is defined as:

$$E = E_0 + \frac{1}{2}\sum u_{\alpha,\kappa}.\Phi_{\alpha,\alpha'}^{\kappa,\kappa'}.u_{\kappa',\alpha'} \quad (3.2.15)$$

where:

$$\Phi_{\alpha,\alpha'}^{\kappa,\kappa'} = \frac{\delta^2 E}{\delta u_{\alpha,\kappa}\delta u_{\alpha',\kappa'}} \quad (3.2.16)$$

where α is the Cartesian direction in which the displacement occurs, κ is the label of each atom in the considered unit cell and $\Phi_{\alpha,\alpha'}^{\kappa,\kappa'}$ is the force constant matrix of the system, which effectively represents the effect on the force experienced on an atom by moving another. One solution to this differential equation is modelling the displacement with a travelling wave:

$$u_{\alpha,\kappa} = \epsilon_{m,\alpha,\kappa,q}e^{iq.R_{\alpha,\kappa}-\omega t} \quad (3.2.17)$$

By differentiating the energy equation to get the force and substituting in the trial solution, the vibrational mode frequencies at the Γ-point can be calculated from:

$$D_{\alpha,\alpha'}^{\kappa,\kappa'}(q)\epsilon_{m,\alpha,\kappa,q} = \omega_{m,q}^2\epsilon_{m,\alpha,\kappa,q} \quad (3.2.18)$$

where:

$$D_{\alpha,\alpha'}^{\kappa,\kappa'}(q) = \frac{1}{\sqrt{m_\kappa m_{\kappa'}}}\sum \Phi_{\alpha,\alpha'}^{\kappa,\kappa'}e^{-iq.R} \quad (3.2.19)$$

$\boldsymbol{D}_{\alpha,\alpha'}^{\kappa,\kappa'}(\boldsymbol{q})$ is referred to as the dynamical matrix and is the Fourier Transform of the force constant matrix, $\Phi_{\alpha,\alpha'}^{\kappa,\kappa'}$. The eigenvalues of this equation are the vibrational mode frequencies and are calculated by taking the square root of $\omega_{m,\boldsymbol{q}}^2$ and the eigenvector $\epsilon_{m,\alpha,\kappa}$ is the atomic displacements of this mode. m refers to the mass of the atom and $\boldsymbol{q}$ is the wavevector.

There are two main methods for calculating $\boldsymbol{D}_{\alpha,\alpha'}^{\kappa,\kappa'}(\boldsymbol{q})$; numerically, using the finite displacement method and analytically, using Density Functional Perturbation Theory (DFPT) [113]. Finite displacement [114, 115] works through displacing an ion by a small distance, $\pm u$, and calculating the resulting forces on every other ion in the system for each direction of the displacement. Using the central-difference formula, the force matrix can be calculated:

$$\frac{\delta F_{\kappa,\alpha}}{\delta u} \approx \frac{F_{\kappa,\alpha}^+ - F_{\kappa,\alpha}^-}{2u} = \frac{\delta^2 E}{\delta u_{\kappa,\alpha} \delta u_{\kappa',\alpha'}} \tag{3.2.20}$$

This completes a row of $\boldsymbol{D}_{\alpha,\alpha'}^{\kappa,\kappa'}(\boldsymbol{q})$ and by displacing along the other two Cartesian coordinates, the rows associated with this atom are completed. Through repetition over each atom in the unit cell, which can be reduced through symmetry operations, the full dynamical matrix can be calculated.

DFPT determines this response through use of perturbation theory [116], which allows calculation of the dynamical matrix from an analytical expression relating the energy of the electron density to a perturbation of ionic position. This technique is not used in this work to calculate the dynamical matrix owing to the 48 hour limit on calculations run on ARC3, the University of Leeds High Performance Computing facility. As VASP [112], the main DFT software package used in this work, is currently is not able to restart this calculation after it is stopped and this work has focused on αLM, which required more than 48 hours to complete, DFPT has not been used in this work to calculate phonon frequencies.

However, it is used to calculate the Born effective charges [117]. These are the co-efficients that relate a polarisation along the unit cell in a particular direction to the corresponding displacement this causes. As, for THz-TDS, many samples are diluted using a non-absorbing medium, the production of an experimentally-comparable simulated spectrum from the frequencies and intensities of the calculated modes can be challenging. This and how intensities are extracted from the Born effective charges will be discussed in Section 3.3.2.

3.2.5 Dispersion Corrections

Whilst DFT is effective at modelling intramolecular forces, it is comparatively much weaker with intermolecular forces such as London dispersion forces [118]. This poses a problem when investigating large complex molecules as often these forces can play a significant role in these systems and the thermodynamic properties can significantly depend on them. As such, numerous empirical dispersion corrections have been created to attempt to recreate these interactions within DFT with minimal computational cost. Owing to the significant sensitivity of calculated spectral features to small fluctuations of electron density, including interactions such as London dispersion forces into the calculation is of vital importance. Most functionals, such as the PBE functional used in this work, do not tend to appropriately describe higher order electron correlational effects such as these. One method of achieving this is to add a correction term to the energy for each calculation step, often called a dispersion correction (DiC). Whilst there are alternative methods for incorporating noncovalent interactions in DFT [119], using DiCs such as those examined in this work are comparatively much less costly and these are now an easily implemented part of most quantum calculation packages. In total, five DiCs were evaluated in Chapter 4 and will be described here. The oldest and simplest was the DFT-D2 [120] DiC which corrects the energy of the system using the formula:

$$E_{D2} = -\frac{1}{2} \sum_{i=1}^{N_{at}} \sum_{j=1}^{N_{at}} \sum_{L}' \frac{C_{6ij}}{r_{ij,L}^6} f_{d,6}(r_{ij,L}) \tag{3.2.21}$$

where $f(r_{ij})$ is the damping factor and is given by:

$$f_{d,6}(r_{ij}) = \frac{s_6}{1 + e^{-d(r_{ij}/(s_R R_{0ij})-1)}} \tag{3.2.22}$$

Parameters C_{6ij} and R_{0ij} are computed using:

$$C_{6ij} = \sqrt{C_{6ii} C_{6jj}} \tag{3.2.23}$$

$$R_{0ij} = R_{0i} + R_{0j} \tag{3.2.24}$$

N_{at} is the number of atoms and L is all translations of the unit cell. When $L = 0$, $i \neq j$. C_{6ij} is the dispersion coefficient for the interaction between atom i in cell $L = 0$ and atom j in cell L. The damping factor minimises contributions from atoms that are normal bond lengths away. The parameter s_6 is specific to the selected functional for the calculation, where for PBE this value is 0.75, and the parameter s_R is usually fixed at 1.0. Finally, R_{0ij} is the sum of the atomic radii and r_{ij} is the distance between atoms i and

j. These are either recommended values from the creators or have been found through testing.

This method was revised by Grimme to give the DFT-D3 [121] DiC that allows for three atoms to be considered instead of two. This allows for geometry effects to be included as the coefficients $\boldsymbol{C}_{nij}$ are dependent on atomic coordination unlike in DFT-D2. This takes the form:

$$\boldsymbol{E}_{D3} = -\frac{1}{2} \sum_{i=1}^{\boldsymbol{N}_{at}} \sum_{j=1}^{\boldsymbol{N}_{at}} \sum_{\boldsymbol{L}}{}' \left(\boldsymbol{f}_{d,6}(\boldsymbol{r}_{ij,\boldsymbol{L}}) \frac{\boldsymbol{C}_{6ij}}{\boldsymbol{r}_{ij,\boldsymbol{L}}^6} + \boldsymbol{f}_{d,8}(\boldsymbol{r}_{ij,\boldsymbol{L}}) \frac{\boldsymbol{C}_{8ij}}{\boldsymbol{r}_{ij,\boldsymbol{L}}^8} \right) \tag{3.2.25}$$

where:

$$\boldsymbol{f}_{d,n}(\boldsymbol{r}_{ij}) = \frac{\boldsymbol{s}_n}{1 + 6(\boldsymbol{r}_{ij}/(\boldsymbol{s}_{\boldsymbol{R},n}\boldsymbol{R}_{0ij}))^{-\alpha_n}} \tag{3.2.26}$$

$$\boldsymbol{R}_{0ij} = \sqrt{\frac{\boldsymbol{C}_{8ij}}{\boldsymbol{C}_{6ij}}} \tag{3.2.27}$$

α_6, α_8, $\boldsymbol{s}_{\boldsymbol{R},8}$ and $\boldsymbol{s}_6$ are fixed at 14, 16, 1 and 1 respectively. $\boldsymbol{s}_{\boldsymbol{R},6}$ and $\boldsymbol{s}_8$ are functional dependent but are usually 1. D3 can also utilise another damping function from Becke and Johnson[122] (DFT-D3BJ) which is more computationally efficient to calculate. This takes the form:

$$\boldsymbol{f}_{d,n}(\boldsymbol{r}_{ij}) = \frac{\boldsymbol{s}_n \boldsymbol{r}_{ij}^n}{\boldsymbol{r}_{ij}^n + (\boldsymbol{a}_1 \boldsymbol{R}_{0ij} + \boldsymbol{a}_2)^n} \tag{3.2.28}$$

Here, $\boldsymbol{s}_6$ is fixed at 1 and $\boldsymbol{s}_8$, $\boldsymbol{a}_1$ and $\boldsymbol{a}_2$ are functional dependent, but also usually have a value of 1. While others have scaled these parameters, our previous work showed that scaling these parameters does not improve the correlation between calculated and experimental spectra [123]. Finally, Tkatchenko and Scheffler [124] (DFT-TS) produced a non-empirical DiC which was calculated from the electron charge-density but otherwise is formally equivalent to the DFT-D2 method. This is calculated with:

$$\boldsymbol{\alpha}_i = \boldsymbol{\nu}_i^2 \boldsymbol{\alpha}_i^{free} \tag{3.2.29}$$

$$\boldsymbol{C}_{6ii} = \boldsymbol{\nu}_i \boldsymbol{C}_{6ii}^{free} \tag{3.2.30}$$

$$\boldsymbol{R}_{0i} = \left(\frac{\boldsymbol{\alpha}_i}{\boldsymbol{\alpha}_i^{free}} \right)^{\frac{1}{3}} \boldsymbol{R}_{0i}^{free} \tag{3.2.31}$$

The quantities $\boldsymbol{\alpha}_i^{free}$, $\boldsymbol{C}_{6ii}^{free}$ and $\boldsymbol{R}_{0i}^{free}$ are the free-atomic polarisability, dispersion coefficient and atomic radii. The effective atomic volumes $\boldsymbol{\nu}_i$ are calculated with:

$$\boldsymbol{\nu}_i = \frac{\int \boldsymbol{r}^3 \boldsymbol{w}_i(\mathbf{r}) \boldsymbol{n}(\mathbf{r}) \boldsymbol{d}^3\mathbf{r}}{\int \boldsymbol{r}^3 \boldsymbol{n}_i^{free}(\mathbf{r}) \boldsymbol{d}^3\mathbf{r}} \qquad (3.2.32)$$

where $\boldsymbol{n}(\mathbf{r})$ is the total electron density and $\boldsymbol{n}_i^{free}(\mathbf{r})$ is the spherically averaged electron density of the free atom. The Hirshfeld weight $\boldsymbol{w}_i(\mathbf{r})$ is defined as:

$$\boldsymbol{w}_i(\mathbf{r}) = \frac{\boldsymbol{n}_i^{free}(\mathbf{r})}{\sum_{j=1}^{\boldsymbol{N}_{at}} \boldsymbol{n}_j^{free}(\mathbf{r})} \qquad (3.2.33)$$

The strength of the dipole-dipole dispersion coefficient is calculated by:

$$\boldsymbol{C}_{6ij} = \frac{2\boldsymbol{C}_{6ii}\boldsymbol{C}_{6jj}}{\frac{\alpha_j}{\alpha_i}\boldsymbol{C}_{6ii} + \frac{\alpha_i}{\alpha_j}\boldsymbol{C}_{6jj}} \qquad (3.2.34)$$

and the atomic radii, $\boldsymbol{R}_{0ij}$, is the same as in DFT-D2.

These corrections and their effect on both the structural optimisation and the calculation of mode frequency and intensity will be discussed further in Chapter 4.

There are some additional corrections available with the VASP calculation package. The term $\boldsymbol{w}_i$ in TS can be altered to use an iterative scheme but this is designed for ionic solids so has no benefit in this study. There are two corrections that were attempted to be used; 'Many-body Dispersion Energy' [125] and 'DDsC' [126] corrections. These either were not able to be optimised to the ground electronic state within acceptable tolerances for the calculation or took too long to do so, making them impractical for regular usage for the purposes of spectral analysis. The hardware and software that we use may improve in efficiency in the future so that these corrections may be able to be used on complex structures such as αLM. Additionally, at the time of writing, D4 [127] is now available which maybe also show promise and this should be investigated in future.

3.3 Calculation of Theoretical Spectra

3.3.1 Geometry Optimisation and Mode Calculation

Section 3.2 describes how the energy of a system is calculated, but this alone is not enough. As mentioned before, all the spectroscopic properties extracted from a DFT calculation are done so from the ground electronic state, which is calculated using an iterative self-consistent method. This requires the atomic positions within the unit cell, and the unit cell itself, to be in their lowest energy configuration which effectively represents
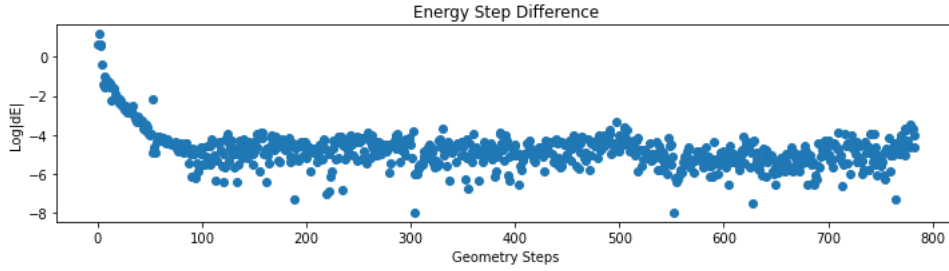
(a) *Change in Energy between Step*
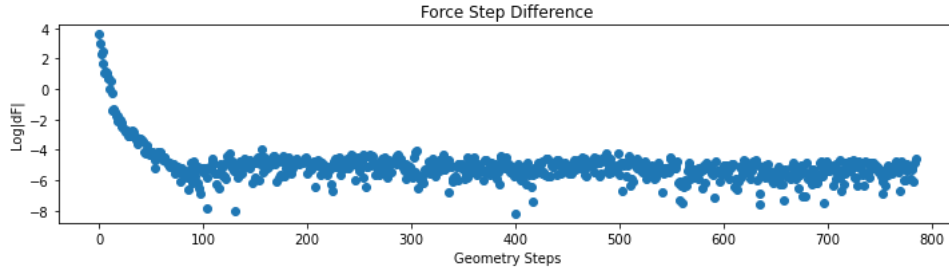
(b) *Change in Force between Step*

Figure 3.2: Changes in Energy and Force between each optimisation step. It is evident that a significant part of the optimisation is spent close to the correct solution but only achieves it after quite some time.

the system at $0\,\mathrm{K}$. As this temperature is impossible to achieve, all structures must first be optimised before its spectrum can be calculated. Both the atomic positions and the unit cell parameters may be changed systematically to lower the system's total energy and once the changes in this value are reduced to below a pre-determined tolerance, the system is considered optimised. In our group, the tolerances that have been previously found to be suitable [123] are $5.0 \times 10^{-6}\,\mathrm{eV}$ changes between steps of the self-consistency loop and $5.0 \times 10^{-5}\,\mathrm{eV}$ changes between steps of the initial optimisation of the ionic positions and unit cell dimensions. The optimisation of just the ionic positions has a electronic energy tolerance is $1.0 \times 10^{-7}\,\mathrm{eV}$ and uses the change in forces between step, with a value of $5.0 \times 10^{-4}\,\mathrm{eV}$. The changes in total energy and forces across these optimisations are demonstrated in Figure 3.2 where the difficulty in finding optimised conditions with such tight tolerances is clear.

Convergence

The number of k-points along each axis and the plane wave cut-off energy are two calculation parameters that must be optimised to find sensible values before the main calculation can begin. This occurs through increasing these parameters until no significant change of the energy of the system is detected. Figure 3.3 demonstrates this process for an αLM

37

calculation performed in this work. The Monkhurst-Pack k-points grids were 715, 826 and 937 in each reciprocal lattice coordinate respectively. Any increase from the first group resulted in a change in the energy of the system of less than $0.001\,eV$ which was deemed not enough to justify the additional computational time. The plane wave cut-off energy was varied between 600 and $1200\,eV$ and was selected to be $900\,eV$, where an increase resulted in a change of less than $0.01\,eV$ to the energy of the system.

One method of examining whether suitable parameters have been chosen is to check the first three modes. These will represent translation of the entire unit cell in each Cartesian coordinate and when the system is simulated with complete accuracy then these modes should be as close to zero frequency as possible. This is owing to the identical nature of each unit cell which means when an ion is translated to the same position in a neighbouring unit cell, it should have the same energy. In practice, this is not the case owing to the finite number of k-points used to sample the BZ. This results in small changes in the energy of the system when considering translation which manifest as non-zero frequencies. These can be projected out [128] and ignored but can serve as a useful measure of how well suited the calculation parameters were. If the k-point grid is not fine enough, then these translational modes will be large ($> 0.2\,THz$) and this is an indication that the frequencies for the vibrational modes of interest will be inaccurate. Whilst these will never be exactly zero, small values below this are generally considered acceptable [123].

Starting Structures

Starting structures are usually obtained from X-ray or neutron diffraction patterns. This means, when obtaining a structure, it is desirable to perform the measurement at as low a temperature as possible. The resulting structure will be closer to its ground state than it otherwise would have been and this reduces the likelihood of finding a local minimum instead of the global one. Neutron diffraction patterns are preferred as the accuracy of the positions of H atoms will be much higher and so the optimisation will often be quicker and more accurate. However, these are much less common and so X-Ray Diffraction (XRD) patterns tend to be used.

Packages

There are many DFT calculation and post-processing packages that can be used for this purpose [108, 129, 130] but this work will use the VASP [112] DFT package to optimise all atomic positions and unit cell dimensions for all calculations in this work. The dynamical matrix and Born effective charges were also calculated using Phonopy [131] which uses VASP as its computational engine. This group has used many packages including CASTEP [129], VASP and Crystal17 to calculate THz absorption spectra with
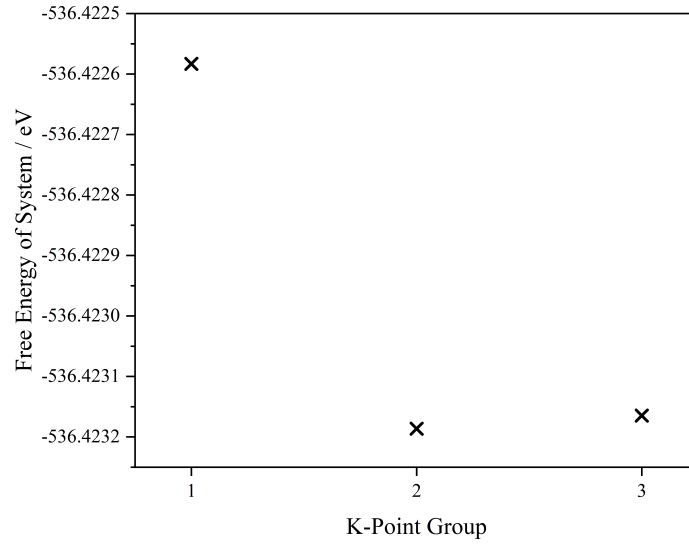
(a) K-Point Convergence
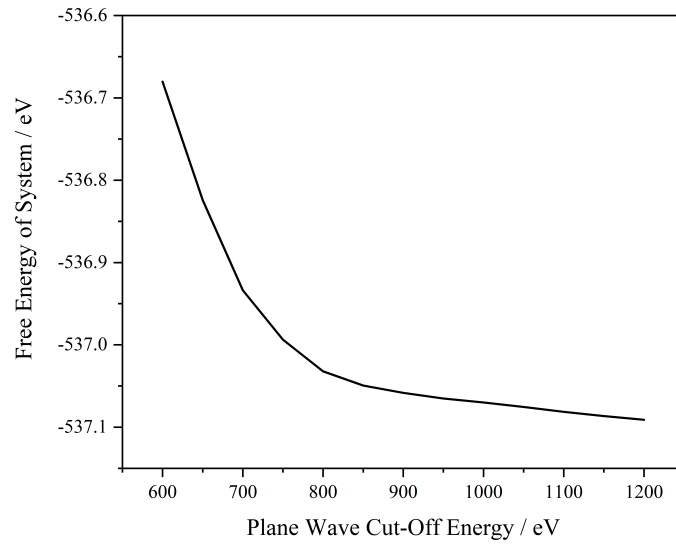
(b) Cut-Off Energy Convergence

Figure 3.3: The convergence of the plane wave cut-off energy and number of k-points for an αLM calculation. The first k-point group and $900\,\text{eV}$ were selected for all subsequent calculations on the αLM system.

success using all three packages. VASP was chosen here as the inclusion of its PAW pseudopotentials mean that a lower plane wave cut-off energy is required than the equivalent CASTEP calculation. Previous calculations have also shown VASP tends to be less sensitive to k-point grid size than some of the other codes. As such this, coupled with the ability of Phonopy to use VASP and improve the efficiency of phonon calculations makes VASP an ideal choice for calculations of these large systems.

3.3.2 Construction of the Simulated Spectrum

PDielec [132], is a DFT and molecular mechanics post-processing package for solid-state applications that enables calculation of IR and THz spectra of a material. This reads in phonon frequencies and normal modes from a wide range of codes while calculating the the mode intensities using the Born effective charges calculated for the given system. In turn the methods included also enable experimental effects such as scattering, particle size, shape and orientation along with experimental sampling method to try and improve the correlation between calculation and experiment. These methods are described in more detail by Kendrick and Burnett [123, 132, 133] but will be summarised here. The Born effective charge tensor is used to calculate the oscillator strength tensor [117]. The trace of this tensor, which is the sum across the diagonal, for a given transition is equal to the intensity of that transition. Whilst each mode is associated with a frequency and an intensity, this is not directly comparable with experiment. In vibrational spectroscopy, modes must always have a width and this width causes the absorption mode to have an inherent shape. This shape depends on the properties of the system, such as temperature. At low temperatures, peaks typically demonstrate a Lorentzian peak shape whereas as temperature increases, peak broadening of a Gaussian nature dominates. The transition intensity of the jth mode, I_j, is related to its integrated molar absorption coefficient, A_j by [134]:

$$A_j = \frac{N\pi}{3c^2 log_e 10} g_j I_j \tag{3.3.1}$$

where N is the number of molecules per unit volume, c is the speed of light and g_j is the degeneracy of the mode. This, assuming a Lorentzian shape, can be related to the peak's Full Width at Half Maxiumum (FWHM), σ_j by:

$$a_j(\bar{\nu}) = \frac{2A_j}{\pi} \frac{\sigma_j}{4(\bar{\nu} - \bar{\nu}_j)^2 + \sigma_j^2} \tag{3.3.2}$$

These peak widths are set within PDielec and can be set to all have the same value or can be individually optimised.
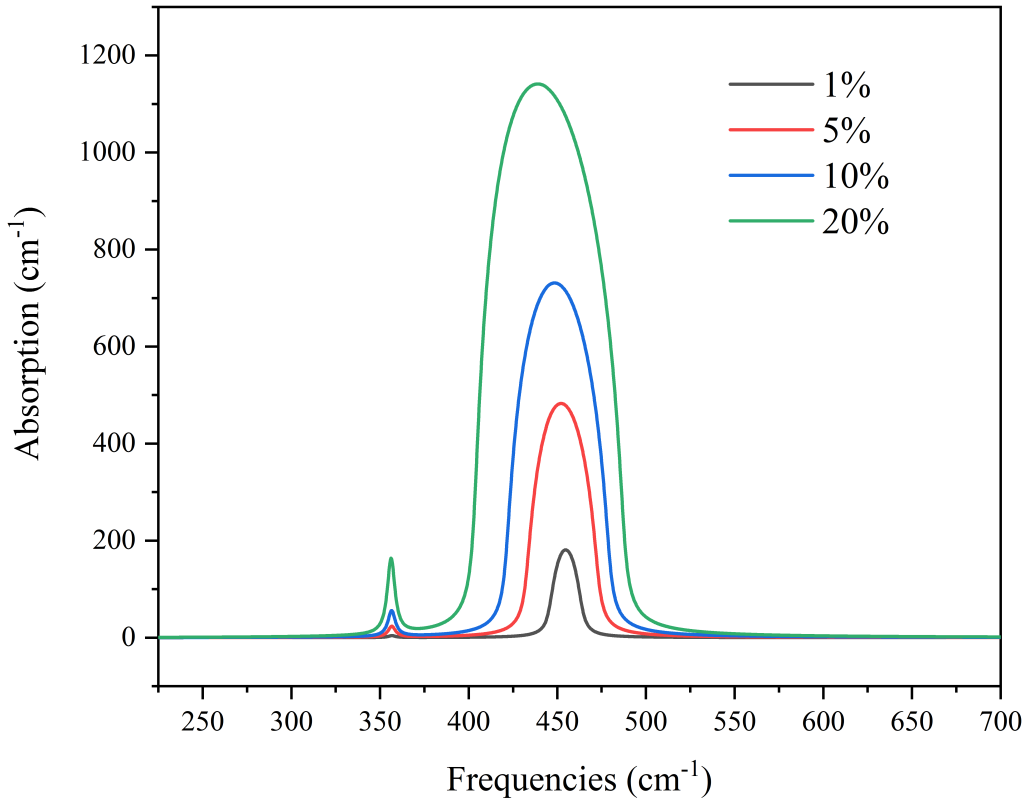
Figure 3.4: The effect of concentration on the calculated THz absorption spectrum of ZnO. The peak widths have been set to be constant so any increase is a result of the mixing model.

Owing to the powdered nature and potential dilution of the sample used to produce the experimental spectrum that the calculation is attempting to reproduce, these properties must be incorporated otherwise the intensities of the modes will be inaccurate. The dilution can be accounted for using an effective medium approximation and is shown for ZnO in Figure 3.4. These figures have been generated using calculations of ZnO provided as a simple example within the latest PDielec release [133].

The effect of not being a single crystal and the dilution medium on the absorption is also modelled through the use of effective medium theories such as the Maxwell-Garnett or Bruggerman mixing rules which allow the composite material to be treated as a homogeneous mixture. The effect of particle shape and choice of theory is depicted in Figure 3.5 where a range of combinations of crystallite shapes and effective medium theories are shown. A more detailed comparison between these theories was done by Kendrick and Burnett [123] but this arises from the interaction between the phonons and the incident radiation where charges form on the surface of the crystallites which affect the oscillation frequency of these phonons.

The effect of air trapped in the medium is significant and must be incorporated to accurately represent the experimental spectrum. This is shown in Figure 3.6, and two factors must be considered. The air void volume fraction and the air void radius. Figure 3.6 shows that the radius dominates the background absorption, especially in the region below
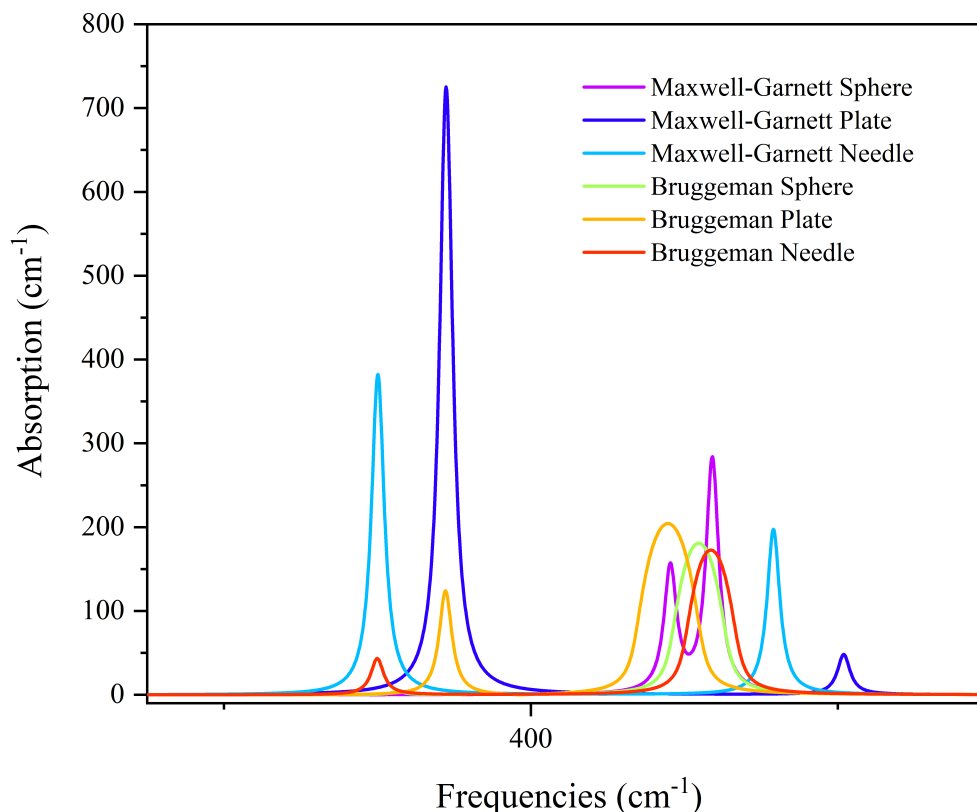
Figure 3.5: A comparison between the calculated THz absorption spectra of crystallites with different shapes using the Bruggerman and Maxwell-Garnett effective medium approximations.

$300 \, \text{cm}^{-1}$ which is currently accessible using our THz-TDS systems. PDielec is including Mie scattering to take into account the scattering of light by the air voids and this is what mostly contributes to the rising background absorption seen in the majority of the THz absorption spectra in this thesis. Further discussion of the importance of including some of these parameters when post-processing with PDielec will take place in Chapter 4.

3.3.3 Generalised Calculation Workflow

Figure 3.7 shows a detailed flowchart of the calculation process. The area in blue shows how the files were set up to begin testing for convergence. The area in green describes the convergence testing process and how parameters were iteratively increased until they were satisfactory. Finally, the area in red describes the process of optimising the unit cell and ionic positions and subsequent calculation of the dynamical matrix and Born effective charges. This is a generalised flowchart that includes a check as to whether these latter parameters could finish within 48 hours whilst using DFPT in VASP. If not, then Phonopy was used instead. The output was then processed in PDielec.
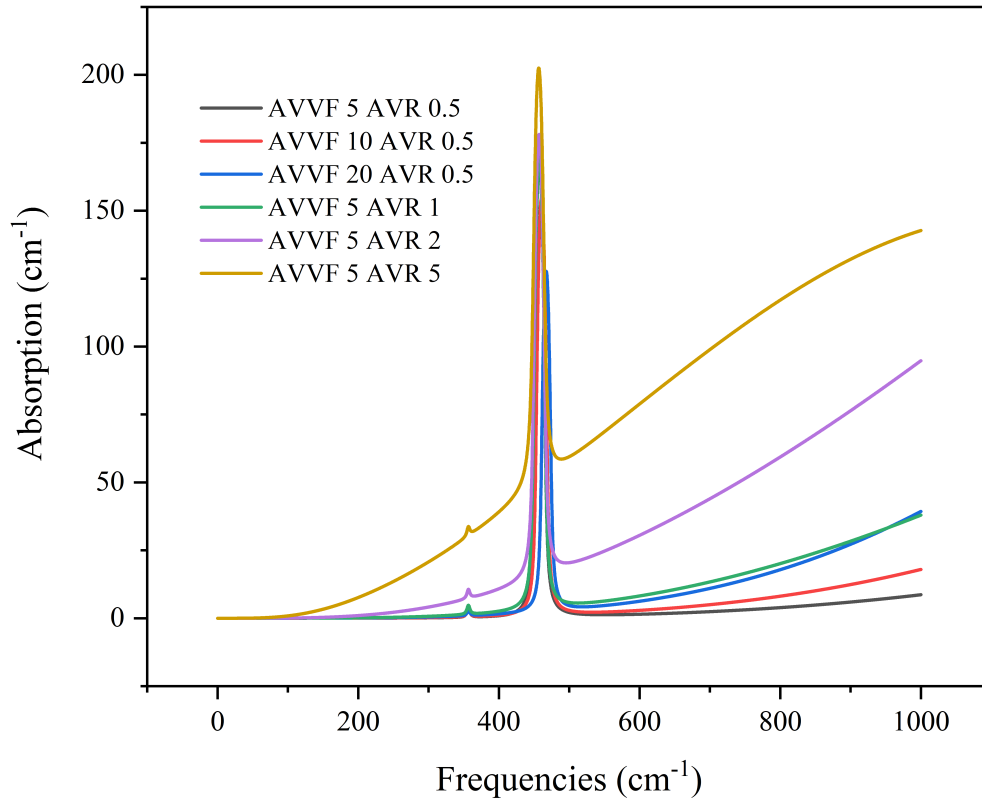
Figure 3.6: The effect of air void volume fraction and air void radius on a THz absorption spectrum.

3.4 Conclusion

This chapter described DFT and the principles and challenges behind its implementation. The process of creating a comparable theoretical spectrum was also detailed. DFT calculations are used extensively in Chapter 4 and Chapter 5 and will be discussed further there.
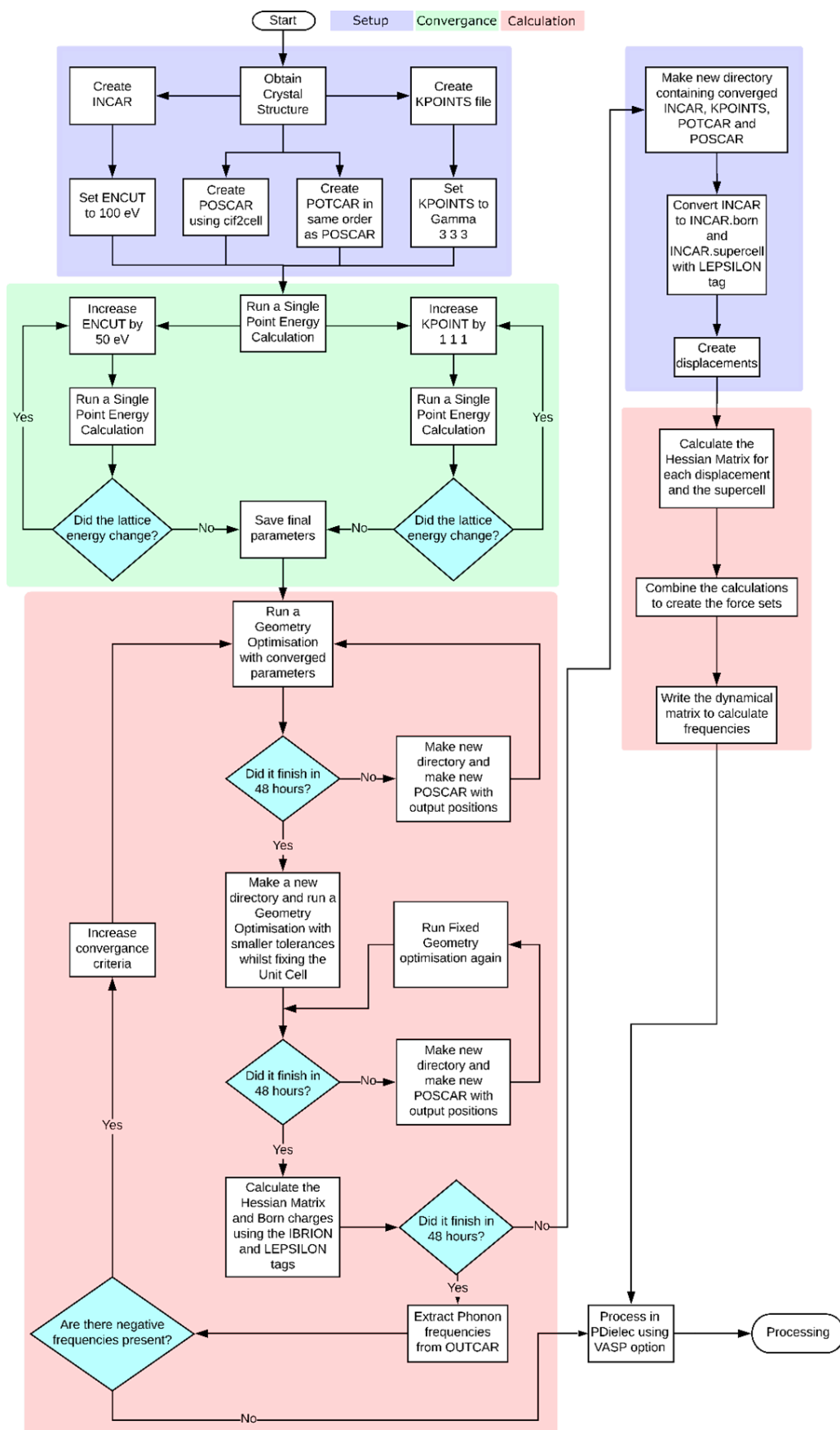
Figure 3.7: A flowchart depicting the set-up of files, convergence testing and main calculation process of a DFT calculation.

Chapter 4

The Effect of Dispersion Corrections on Calculated Terahertz Absorption Spectra

4.1 Introduction

As discussed in Section 3.2.5, intermolecular forces tend to be poorly modelled when using DFT which can pose a significant challenge to the interpretation of the spectra of organic molecular crystals. This is owing to the common presence of intermolecular bonds, such as London dispersion forces, in this type of material which can significantly alter the calculated phonon properties. These are accounted for using dispersion corrections (DiCs) but there are a range of corrections to choose from with most DFT software packages.

This chapter describes an investigation into the effects on the calculated THz absorption spectra of αLM and the underlying vibrational modes for several DiCs. Subsequently, the effect of the optimisation of the starting structure was also carried out. This had the aim of understanding how any differences in the calculated spectra might be caused by discrepancies between the final structures for each DiC. The unit cell of αLM, shown in Figure 4.1, contains two molecules of α-Lactose and two molecules of H_2O. As there are a significant amount of $O–H$ bonds present, it is critical that these are accounted for correctly as it is likely these have a significant impact on the THz absorption spectrum. These bonds and other interactions between the molecules that are present are particularly sensitive to the arrangement of both the molecules within the unit cell and the atoms in the molecules. The influence that these entities have on each other results in a complicated potential energy hypersurface which drastically affect the nature and frequencies of the calculated modes. As the intensities of vibrational modes are dictated by the magnitude of a change in dipole moment across the oscillation, these are extremely sensitive
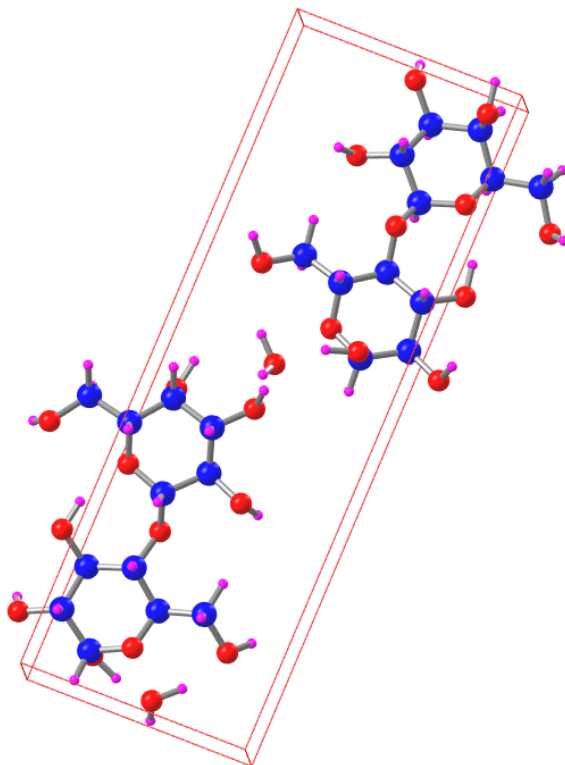
Figure 4.1: The Unit Cell of αLM. Key: C - Blue; O - Red; H - Magenta.

to the locations and motions of the point charges. This means that small changes across this potential energy landscape can have large effects on the final mode properties and this is most apparent when directly comparing the experimental and calculated spectra. The success or failure for any DFT calculation of spectral modes is determined by how comparable the mode frequencies and intensities are to their experimental counterparts.

The DiCs selected include the D2 [120], D3 [121], D3BJ [122] and TS [124] corrections which were described more completely in Section 3.2.5. Additionally, a calculation where no DiC was included has been performed for the purposes of a control and to demonstrate the necessity of such corrections to THz absorption spectra calculations. Finally, the repeatability of calculations was examined with four new calculations using the D3 correction and comparing these to each other and the original D3 calculation. As D2 is one of the oldest corrections, it is expected that it will perform better than having no correction at all but worse than the other corrections as these were created to be improvements to D2. Of the remaining three corrections, using D3 and D3BJ should provide similar results. The TS correction should produce results approximately between D2 and the D3 corrections owing to it being formally equivalent to D2 but its resultant properties are charge-density dependent which allows it to more completely account for local atomic environment which contributes greatly to non-covalent interactions. The tools developed and used for the interpretation and analysis of the vibrational motion will also be presented.

4.2 Method

4.2.1 Experimental Spectrum
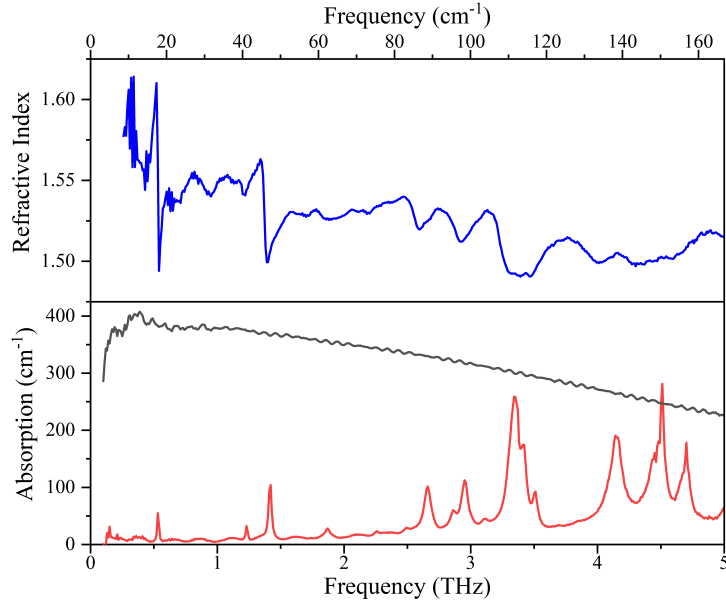
Figure 4.2: The THz absorption spectrum of an αLM pellet in a 10% mass ratio with PTFE, taken at 4 K. The dynamic range of the spectral measurement is shown and crosses the absorption at approximately 4.5 THz. Finally, the top pane shows the frequency-dependent refractive index of the sample. It can be seen that the large changes in refractive index correspond to the peaks in the absorption spectrum.

Figure 4.2 shows the experimental THz absorption spectrum and refractive index of a pellet of αLM and PTFE in a 1:9 mass ratio, along with the dynamic range of the THz measurement. This spectrum was taken at 4 K on System 1, the THz-TDS system described in Section 2.2.1. As discussed in Chapter 2, the dynamic range represents the ratio of the highest detected signal component and the noise floor of the system. This means that after the point at which the absorption and dynamic range intersect, the central frequency and maximum absorption of each peak cannot be accurately determined. Two peaks in this range have been included to determine the impact of the corrections on some higher frequency modes as updates to the THz-TDS system and its generation and detection methods will allow accurate determination of these spectral parameters in the future.

4.2.2 Density Functional Theory Calculation Parameters

As described in Chapter 3, most starting structures for these calculations are obtained from a single-crystal XRD pattern. All structural optimisations and spectral calculations were performed on the αLM structure measured at 150 K by Smith *et al.* [135], obtained

from the Cambridge Crystallographic Database [136]. The k-point grid and plane wave cut-off energy were converged using the method previously described in Chapter 3, resulting in a Monkhorst-Pack k-point grid of 715 with a total of 35 k-points and a cut-off energy of 900 eV. A separate geometry optimisation and calculation of the vibrational properties was performed for each DiC, according to the method described in Section 3.2. The post-processing of these DFT calculations to construct a vibrational absorption spectrum is performed using PDielec [132] using the settings described below. Each scan has a resolution of $0.2\,\mathrm{cm}^{-1}$ and the peak widths were matched to their experimental FWHMs. This is discussed further in Section 4.3.1.

4.3 Analysis and Results

4.3.1 Effect of Dispersion Correction on the Calculated Terahertz Absorption Spectrum

As discussed in Section 3.3.2, only the individual mode frequencies and intensities are produced in the calculation. To compare these to an experimental spectrum, the modes must be assigned a peak-width and the absorption values for the frequencies between these peaks must be interpolated. This was done using PDielec, where after trialling each effective medium theory for the best correlation with experiment, Bruggerman's [137] theory was selected in a 10% ratio by mass with PTFE. To better account for features such background absorption, which typically results from light being scattered through the sample and manifests as a slowly rising base absorption as frequency increases, air voids were included with a void radius of $13\,\mu\mathrm{m}$ and total volume of 5%. This value is in near agreement with [138] who first introduced air inclusions into calculations for similar pellets. The rising background absorption that increases with frequency is chosen with the aim of increasing calculated and experimental spectral correlation.

Figure 4.3 shows the experimental THz absorption spectrum with the background removed and the Lorentzian peaks that were used to calculate the peak widths for use in constructing the theoretical spectrum. These peak widths are shown in Table 4.1. These were obtained using Origin's Peak Finder function with the background first being removed using the Asymmetric Least Squares Smoothing algorithm where an asymmetric factor of 0.001, a threshold of 0.001, a smoothing factor of 4 and 10 iterations were used. The peaks were found using the 1st derivative method. Each experimental peak width was matched to its corresponding calculated peak and while generally, across all calculations, it was clear which experimental peak corresponded to a given calculated peak, this was sometimes challenging and so the peak was also matched using its intensity. Assignment of peaks and peak widths has been consistent across each DiCs calculation.
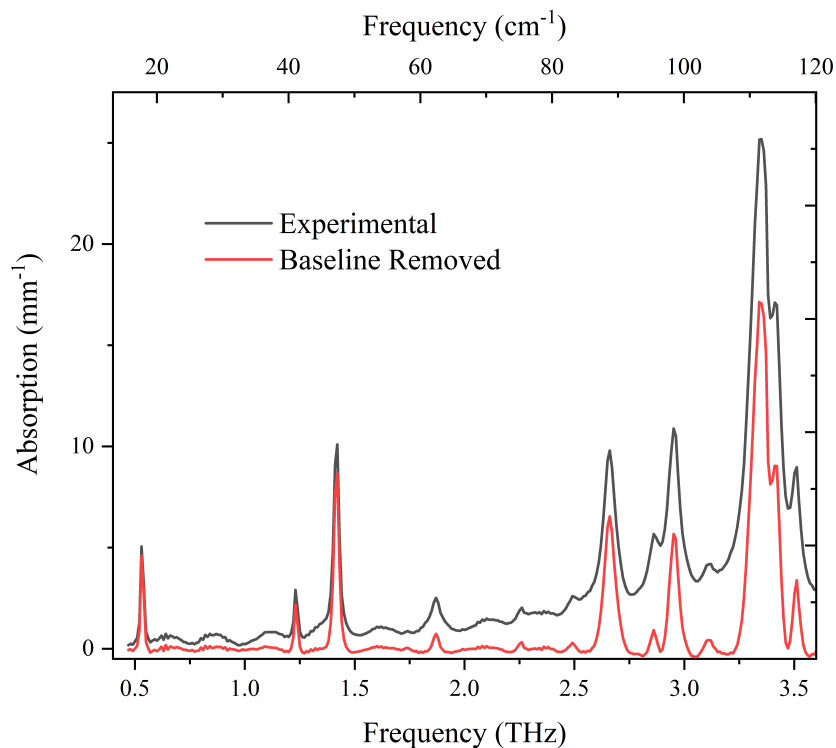
(a) Removal of background absorption for better peak analysis.
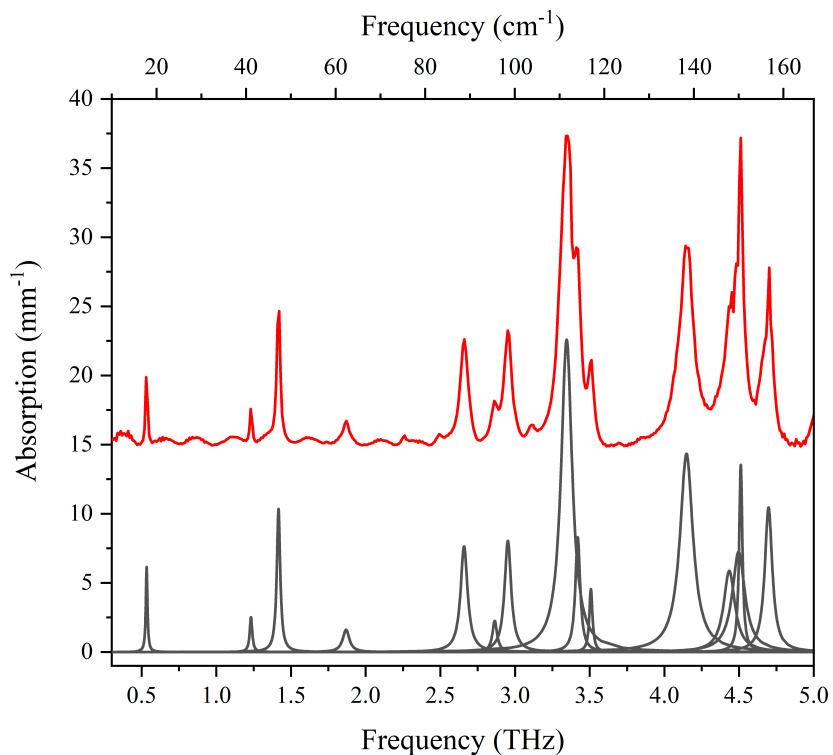
(b) The Lorentzian peaks used to model the experimental peaks and extract the FWHMs, shown in black. The experimental data with its background absorption subtracted is shown for comparison in red and is offset by $15\,\mathrm{cm}^{-1}$ for clarity.

Figure 4.3: The process of extracting peak properties from the experimental THz absorption spectrum.

| Mode	Mode Frequency / cm^{-1}	Peak Width / cm^{-1}	Peak Height / cm^{-1}
1	17.8	0.43	6.15
2	41.1	0.67	2.52
3	47.2	0.91	10.4
4	62.3	1.77	1.61
5	88.6	1.86	7.63
6	95.5	1.27	6.15
7	98.4	1.76	8.04
8	111.5	2.97	22.6
9	114.0	1.29	8.30
10	116.9	0.84	4.55
11	138.3	3.51	14.3
12	147.8	3.04	5.87
13	149.9	3.42	7.24
14	150.4	0.87	13.5
15	156.6	2.02	10.4

Table 4.1: The properties of the Lorentzian peaks used to model the experimental THz absorption peaks of α-Lactose Monohydrate shown in Figure 4.3b.

The calculated spectra both with and without a DiC are shown in Figure 4.4a. It is evident that not using a DiC drastically affects the spectral features above 3.5 THz, but below this shows some agreement with the other corrections. However, the differences that are present show that it is not acceptable to do these calculations without using a DiC if experimentally comparable results are required. The D2 correction seems to have slightly overestimated the modes above 4 THz, whilst the remaining corrections are very similar in terms of mode frequencies and shape. From initial inspection, D3 appears to match the experimental spectrum the best although the TS correction also represents the experimental reasonably well. Comparison of the positions of the first and most intense resolved peak between calculated and experimental spectra is one method of quickly assessing how well a calculation has performed and these are detailed in Table 4.2. The first peak for αLM is particularly important owing to it not shifting with temperature and its small width. Here, the D3 correction matches experiment most closely and is the only calculation to produce a mode frequency within the frequency resolution of System 1 but the TS correction produces the best experimental correlation with the largest resolved peak. The largest peak in the spectrum is not used as owing to the dynamic range of the system, the true experimental mode frequency is not known accurately. Ideally, this peak would be used as it will dominate any spectral optimisation and correlation.

The method chosen to compare experimental and calculated spectra was to calculate the normalised cross-correlation coefficient [123]. This is where the signals are normalised and one signal is shifted along an axis, in this case frequency, and the overlap between these signals is calculated for each shift using integration. The signals are normalised
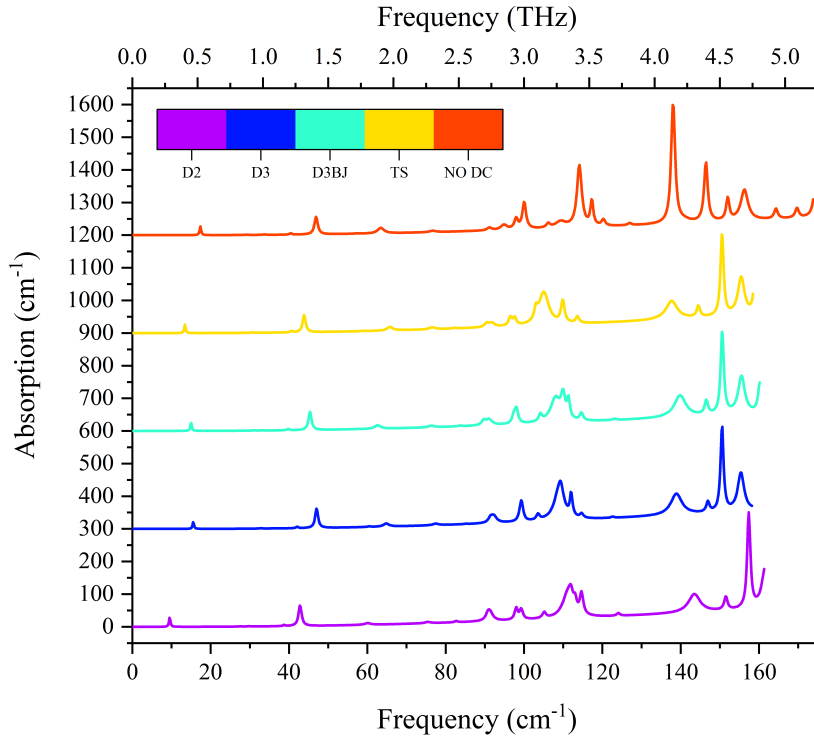
(a) *The calculated THz absorption spectrum for each correction. All of the corrections have had largely similar effects on the peak positions whereas having no correction causes a large difference in the final spectrum.*
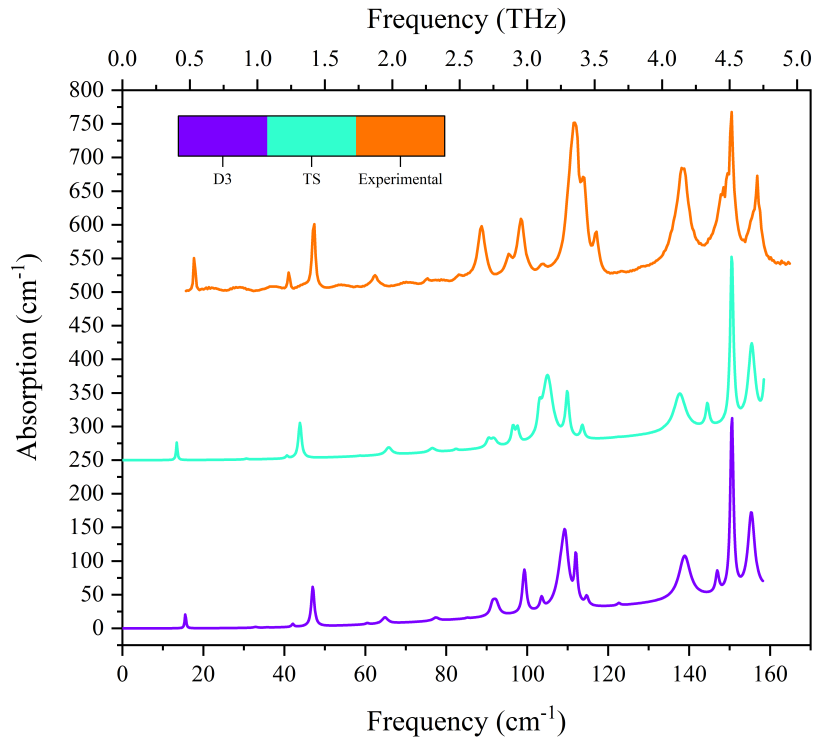
(b) *The TS and D3 spectra compared to the experimental spectrum. The D3 correction is evidently the most similar to the experimental spectrum.*

Figure 4.4: The final spectra for each correction and the experimental spectrum. As expected, the spectrum where no correction was used is not acceptable but the D3BJ correction also did not perform ideally. The D3 spectrum appears to have most of the spectral features in the correct place below the noise cutoff at 4.5 THz

Correction	First Peak Frequency / cm^{-1}	Largest Resolved Peak Frequency / cm^{-1}
None	21.54	109.96
D2	16.38	115.72
D3	18.01	113.87
D3BJ	20.08	112.68
TS	19.77	111.13
Exp	17.60	111.79

Table 4.2: The first and largest resolved calculated and experimental spectral peaks. For the first peak, the D3 correction has the closest value whilst the TScorrection has the closest value to the largest resolved peak

using the equation:

$$A_{norm}(i) = \frac{A(i) - A_{mean}}{\sqrt{n}\sigma(A)} \tag{4.3.1}$$

Where $A_{norm}(i)$ is the normalised value in row i, $A(i)$ is the un-normalised value in row i, A_{mean} is the average signal value, n is the number of rows in the dataset and σ is the standard deviation of the whole dataset. The size of this integral is recorded as a function of the value of the shift and the maximum value of this overlap indicates where the signals are most similar. This maximum can then be used to compare the relative success of each correction. The cross-correlation can take values of -1 to 1, where 0 is no correlation and a value of 1 would mean identical signals. The shift where maximum overlap occurred has also been recorded. This attempts to correct for any systematic error in the calculations but large values indicate a worse result.

PDielec also allows frequency scaling, where the mode frequencies are multiplied by a scaling factor, which is commonly used to crudely incorporate anharmonic effects into the system that is not incorporated during the calculation. For each DiC, these values were optimised to maximise correlation between experiment and calculation. The effect of these corrections is shown in Figure 4.5, where it can be seen that a majority of the peaks align better with their experimental counterparts after scaling. This can cause small over-corrections in some cases, such as for the group of three peaks at $115\,\text{cm}^{-1}$, however the overall spectrum is better represented. At these low frequencies, the frequency scaling has a much smaller effect on the correlation than the frequency shift but when considering the mid-IR as well, scaling can have a much larger effect. Additionally, the Root Mean Squared (RMS) error is also calculated which the average difference between the correlated and experimental values. An increase in correlation does not necessarily result in a decrease in RMS error. Both values for the original and optimised calculated spectra are presented in Table 4.3. It is worth noting that the inclusion of the experimental peaks past the dynamic range of the THz-TDS system is likely to reduce comparability between

experimental and calculated spectra in this region. This will likely reduce correlation and increase RMS error, however this should be consistent across all corrections.
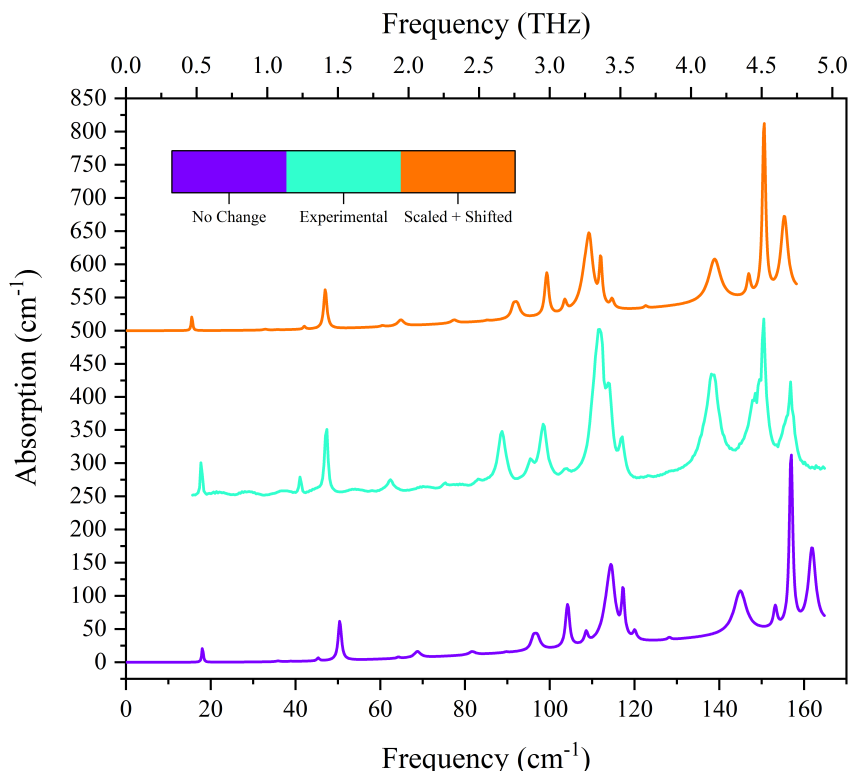
Figure 4.5: The effect of incorporating PDielec frequency scaling and shifting on the D3 calculated spectra. It can be seen that there is much better agreement with the experimental spectrum after these effects are applied.

As was indicated by inspection and brief analysis of the key mode frequencies, the D3 correction has the highest correlation value and also the lowest RMS error. It also used the lowest frequency shift to do this but was also the only correction where the optimisation process chose a frequency scaling factor of less than one. The D2 correction correlated surprisingly well but required the largest shift and scaling factor indicating the original spectrum was quite flawed. The D3BJ correction was also well correlated but did not represent the central large peaks well. Finally, although the TS spectrum performed relatively poorly when considering correlation, the spectrum could not be improved with spectral optimisation which may indicate a better representation of the real system. It is worth noting that it also has the second lowest RMS error. It is possible that slight mismatches in the higher frequency modes lowered the correlation for the TS calculation.

In Figure 4.4b, the D3 and TS are shown alongside the experimental spectrum. Whilst both bear a good resemblance, the D3 correction demonstrated a superior ability to match the features of the experimental spectrum in this case. Whilst mode frequencies and relative intensities appear to match well, the difference between absolute intensities is approximately a factor of two. The reason for this discrepancy has not yet been identified but may be a result of underestimating the magnitude of the mode's constituent oscillations.

Correction	x-Correlation	Magnitude of Shift / cm^{-1}	RMS Error	Frequency Scaling
None	0.6456	1.4	0.164	1.0000
D2	0.7173	-4.8	0.182	1.0000
D3	0.7693	-6.2	0.160	1.0000
D3BJ	0.7906	-4.6	0.158	1.0000
TS	0.7136	-6.4	0.149	1.0000
None - Scaled	0.7063	-6.2	0.208	1.0922
D2 - Scaled	0.8032	-8.0	0.175	1.0273
D3 - Scaled	0.8136	-2.0	0.138	0.9721
D3BJ - Scaled	0.7941	-5.2	0.159	1.0033
TS - Scaled	0.7142	-6.4	0.149	1.0004

Table 4.3: The calculated and experimental spectral correlation and error before and after spectral optimisation. The D3 correction performs the best for both correlation and RMS error. It was also the only run to have a scaling factor of less than one. This also shows that the optimisation process increases the spectral correlation and should be applied to each future spectrum.
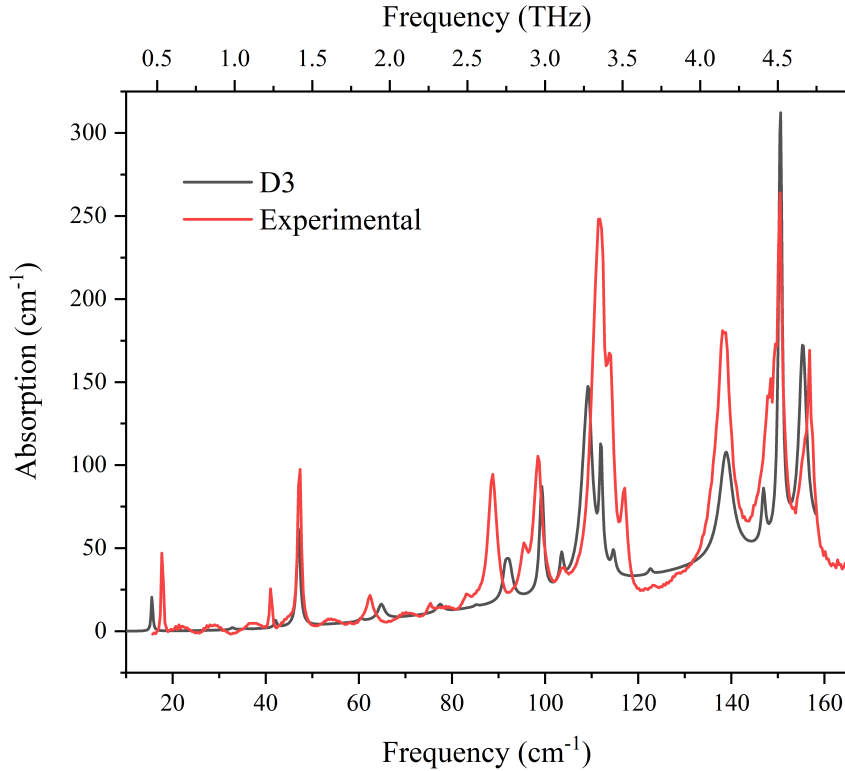
Figure 4.6: The optimised D3 THz absorption spectrum alongside the experimental spectrum presented in a manner that highlights the differences. Whilst most peaks show very agreements, some of the central peaks are slightly misaligned; particularly the mode at approximately $90\,\text{cm}^{-1}$.

However, this is much less important than the relative intensities of the peaks. In Figure 4.6, the differences between the D3 spectrum and the experimental have been made more apparent. Whilst most modes show excellent agreement, the mode at $90\,\text{cm}^{-1}$ in the calculated spectrum shows the largest discrepancy. This mode may be more anharmonic

than the other modes and this will be analysed further below and in Chapter 5.
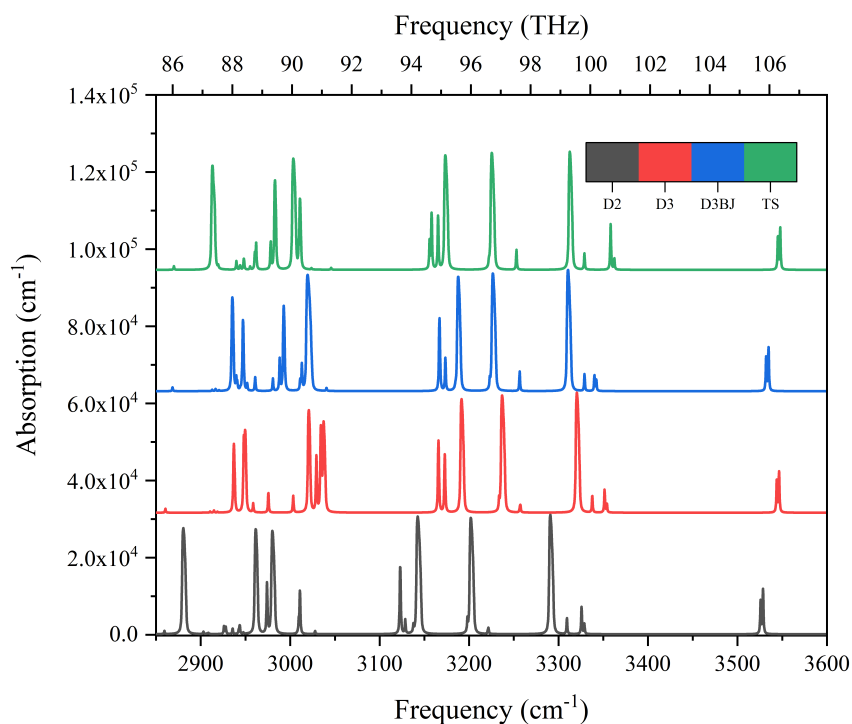
Figure 4.7: The calculated absorption spectrum in the mid-IR range that is associated with *O–H* bonds. While there are minor discrepancies, an experimental spectrum in this region would not have resolved peaks and so these differences are largely irrelevant.

As these low-frequency modes can be difficult to analyse completely, it can be useful to also examine the impact of DiCs on higher frequency modes in the mid-IR where the motions involved are easier to interpret. The mid-IR spectrum between 2800 and $3600\,\mathrm{cm}^{-1}$, the range where OH intramolecular vibrations are typically found, for each correction is shown in Figure 4.7. It is clear that whilst the largest modes are fairly close together there is still some differences on mode position and relative intensity, even at this range where the theory is well understood. However, these calculated spectra do not incorporate features such as OH group broadening, where all the peaks shown would be obscured and grouped as either one large or two slightly smaller peaks. This is owing to H-bonding between O and H which will cause the mode frequency to have a large distribution. As such, these discrepancies would be largely unimportant when comparing to a real spectrum at this frequency range.

4.3.2   Effect of Dispersion Correction on Structural Optimisation

Although the correlation between experimental and calculated spectra is extremely important, this arises from the aim of understanding the nature of the underlying modes which are much more difficult to predict in the THz region when compared to the mid-IR region. With this in mind, the effect on the structures that each correction had was also

investigated. During this investigation, a more complete method for analysing changes between starting and final structures and providing a more complete description of the final structure has been developed.

The DiCs are added to better account for Van der Waals (VDW) forces which are extremely important in the stability of organic molecular crystals such as αLM. These forces are responsible for holding the crystal together and so during the structural optimisation, as the algorithm is trying to find the system's minimum energy, it is expected that having no correction will cause the unit cell to expand whilst it will contract slightly for the optimisations with a correction. This is likely owing to the temperature the original structure was measured at and that these optimisations do not account for temperature so the small amount of thermal energy even at 150 K will alter the atomic positions and unit cell parameters. Without a correction accounting for the intermolecular forces, the energy of the system will be lowered by moving each molecule further apart which will cause the expansion. In Figure 4.8, the final values for the optimised cell parameters of the five structures that were varied are shown. As expected, the volume decreased for each optimisation with the exception of the run without a correction. With the exception of the b unit cell axis for D3, D3BJ and TS, each axis decreased. This is possibly owing to this being the longest axis by a significant margin and the molecules in the unit cell being aligned with this plane so it has the smallest degree of intermolecular bonding. The D2 correction seems to have overestimated the intermolecular forces and has significantly decreased the unit cell volume. This is also to be expected as D3, D3BJ and TS were all designed to be improvements to D2. The β angle is the angle between the a and c unit cell axes and breaks the trend for the D2 correction but owing to the comparative size of the change to the angle itself, this was not considered an issue. These results correlate with the final cell volumes shown in Figure 4.8e. Owing to the large volume of the unit cell, these changes correspond to a maximum of a 5% shift in total volume.

To ensure that no drastic change had occurred in the structures and to compare the effect of the DiC on the structure, some comparisons between the starting and final structures were made. As the starting structure for each optimisation was obtained at 150 K, the optimisation should have ideally not altered the structure to a significant degree as it should already be reasonably close to the ground state. Firstly, Pymatgen [139] was used to represent the structure as a matrix that has been normalised by a scaling factor which is proportional to the volume and number of sites. The atomic sites are then compared directly and the average RMS displacement, normalised by a factor of $(V/n_{sites})^{1/3}$, and the largest RMS displacement are extracted for every atom in the unit cell with the exception of the H atoms. This is owing to the poor resolution of light atoms in XRD, resulting in large changes in position during the optimisation that are unlikely to be chemically significant. These are tabulated in Table 4.4. When the structures

(a) *a-axis of unit cell difference.*

(b) *b-axis of unit cell difference.*

(c) *c-axis of unit cell difference.*

(d) *β angle of unit cell difference.*

(e) *Volume of unit cell difference.*

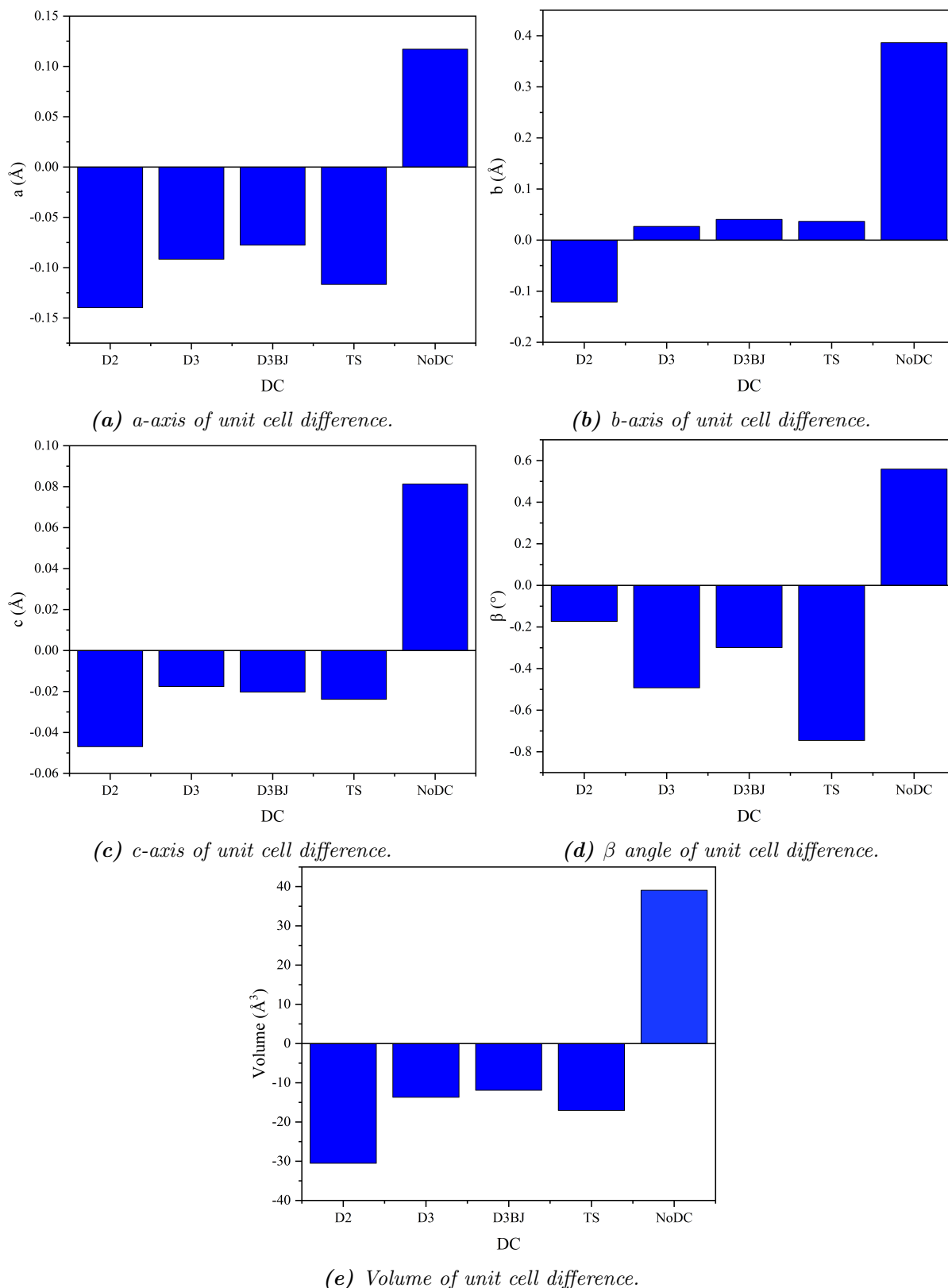**Figure 4.8:** The differences between the starting and final unit cell parameters. As expected, the volume increased for no correction and decreased too much for the D2 correction. The other corrections have had similar effects on the unit cell. The a-axis corresponds to the vertical axis, while the b-axis corresponds to the long horizontal axis and the c-axis corresponds to the short horizontal axis.

directly using these matrices, the D2 optimisation changed the structure the least whilst the TS structure was changed the most, when considering both average and maximum RMS displacement.

Correction	Average RMSD / Å (Non-H Atoms)	Maximum RMSD / Å (Non-H Atoms)	Euclidean Distance / Å (All Atoms)	Cosine Similarity (All Atoms)
None	0.0760	0.1491	0.307	0.9919
D2	0.0689	0.1288	0.358	0.9883
D3	0.0806	0.1659	0.354	0.9888
D3BJ	0.0759	0.1572	0.350	0.9889
TS	0.0858	0.1734	0.359	0.9884

Table 4.4: The values for the structural analysis metrics. The average and maximum RMS displacement values are measured on the structure itself, whereas the euclidean distance and the cosine similarity were measured on the fingerprint structures. The TS structure appears to have changed the most from the starting structure but overall, all of the structures are relatively close to the starting structure.

These are all small changes so reasonable confidence can be assumed in the success of the geometry optimisation owing to the low temperature of the starting structure. However, this is a somewhat crude method that does not account for atomic environment.

A method developed by Zimmerman [140] creates a 'fingerprint' for each atomic site in the structure which is a vector containing its coordination environment and oxidation state as well as its Cartesian and fractional positions. These can be compared through measuring the Euclidean distance and cosine similarity of these vectors, where structures that are identical are represented by a Euclidean distance of zero and a cosine similarity of one respectively. These are also tabulated in Table 4.4. These show a different trend than before but considering that coordination environment has a much larger effect, this is not necessarily disagreement. It is clear that the change was very similar for each correction as the variation between these values is much smaller than for the average and maximum RMS displacement. This also indicates that without a correction, the optimisation has changed the structure differently than with a correction. One thing that is encouraging is that the DiC 'groups' that have similar damping corrections seem to have similar effects on the structure.

To understand how these small differences in structure effect the spectra, the average values do not provide enough detail. A violin plot that shows the distribution of each atom type's total shift, along with changes in bond lengths and bond angles were produced for further analysis. Figure 4.9 demonstrates one of these differences where the D2 calculation has two O atoms that have moved significantly compared to the other calculations, which was the most significant shift present throughout all of the optimisations. However, analysis of the bond lengths and angles does not indicate any abnormalities so it assumed

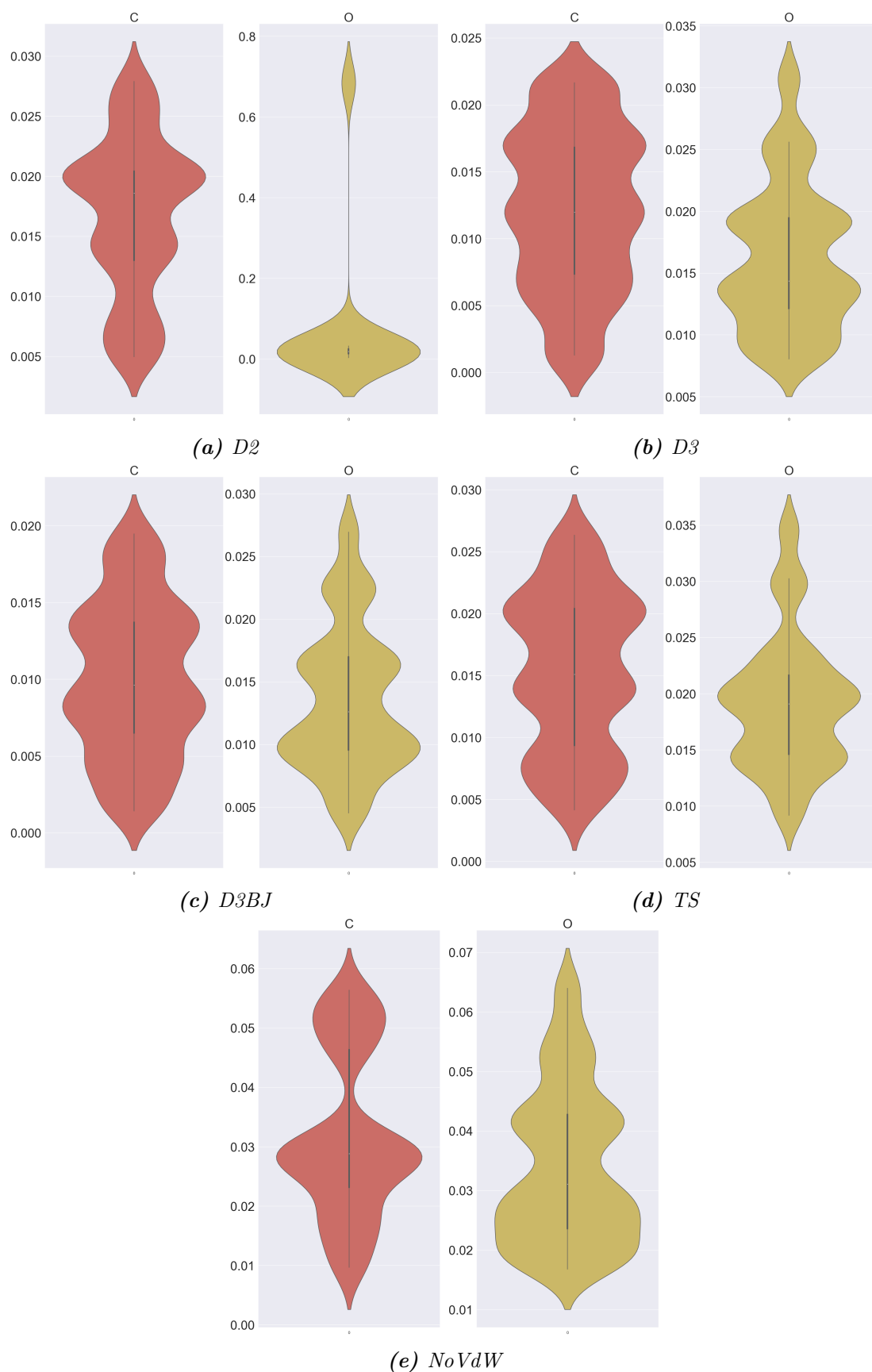**Figure 4.9:** The shift of each non-H atom for each DiC. The D3, D3BJ and TScorrections caused similar changes which is indicated by the shape and length of the plot. In the D2 optimisation the two O atoms that have shifted dramatically can be clearly seen. The distribution of the plot below zero does not indicate negative displacements but a large number of values close to 0. Key: C - Red; O - Yellow.

that this is owing to significant movement of the two water molecules present in the crystal structure. As above, the D2, D3 and TS corrections are shown to have resulted in similar structural changes when considering the overall distribution and length of each plot. Finally, the plot for the no correction shows the C and O atoms, which make up the main backbone of the structure, moved the least of any calculation. It should be noted that whilst many of the distributions of the violin plots finish below zero, this does not indicate negative displacement. Rather, it indicates a large number of values close to zero and for an optimisation that began on a low-temperature structure, such as this one taken at $150\,K$, this is a good indicator that nothing too drastic has changed. Therefore, these plots can be used as a quick test to make sure that a calculation has not changed the structure too much as well as reveal more information about the structural changes caused by the optimisation.
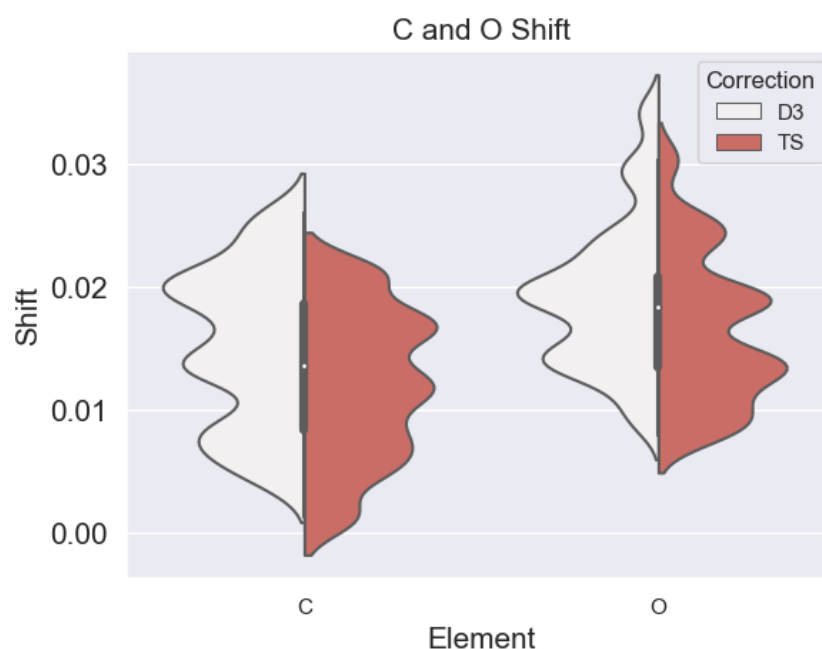
Figure 4.10: The direct comparison of the violin plots of the D3 and TS corrections. It is evident that the D3 correction caused a greater shift of atomic position but that the distribution of atoms is largely similar.

Figure 4.10 shows the violin plots of atomic shift for the D3 and TS corrections in direct comparison. It appears that the D3 correction caused the C and O atoms to shift slightly more over the course of the optimisation but that the general distribution is largely similar. This would indicate that the structures are similar in terms of relative ionic positions but appear to be shifted within the unit cell. However, these discrepancies do not appear to directly correlate to the spectral differences between the D3 and TS corrections, showcased in Figure 4.4b.

4.3.3 Mode Analysis

The complex variety of motion can be visually confusing for most modes when comparing calculations and so for most, visual comparison is not possible. However, for some it is and this is shown for the mode at $50\,\mathrm{cm}^{-1}$ for the D2/D3 comparison in Figure 4.11. Whilst the arrows are pointing in different directions, this is simply owing to them showing each half of the motion about the equilibrium position. This mode was represented well by the calculation and this seems appropriate when considering that the each molecule is moving as one entity and away from each other. These kinds of motions are probably better represented by the harmonic approximation and so match up well with experiment.
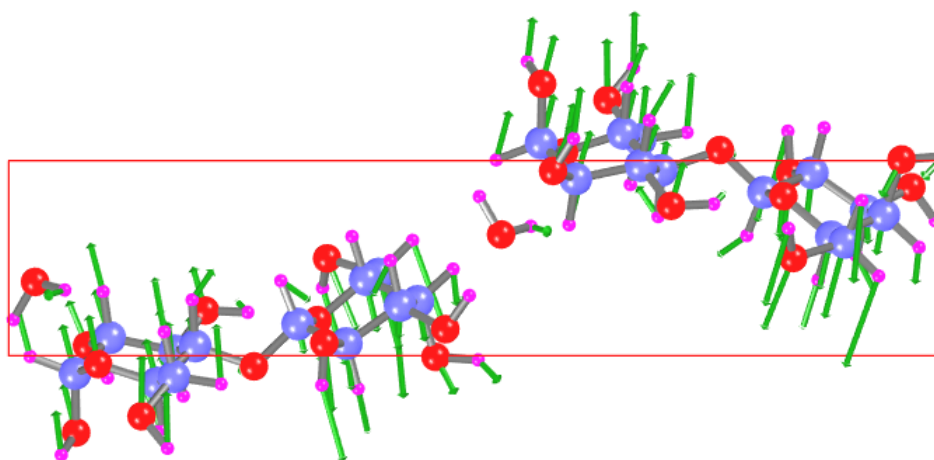
(a) D2 Mode 1
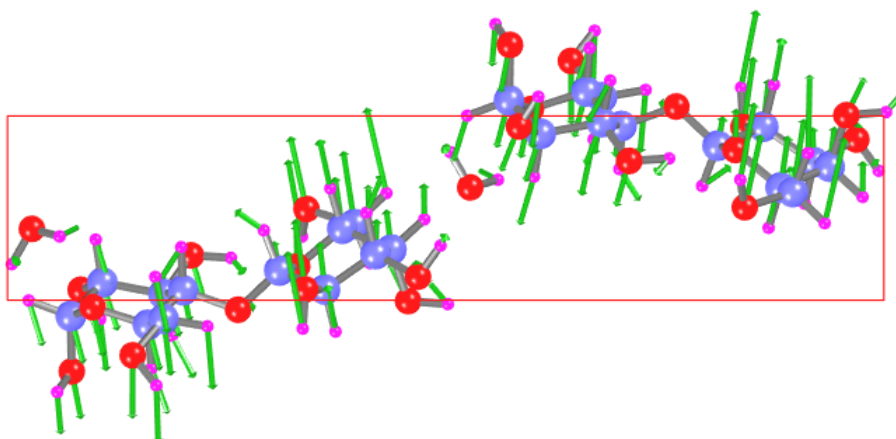
(b) D3 Mode 1

Figure 4.11: Mode 8 from the D2 and D3 correction calculations. This is to show that the mode orders have not changed around and mode motions are very similar. The opposing arrows between corrections is each side of the mode's motion from equilibrium.

When attempting to interpret the calculated modes in the THz range, it is important to define how the motions of the modes are broken down. The modes in this range do not consist of one kind of motion but are made up of varying amounts of translational, rotational and vibrational components where translational and rotational are considered
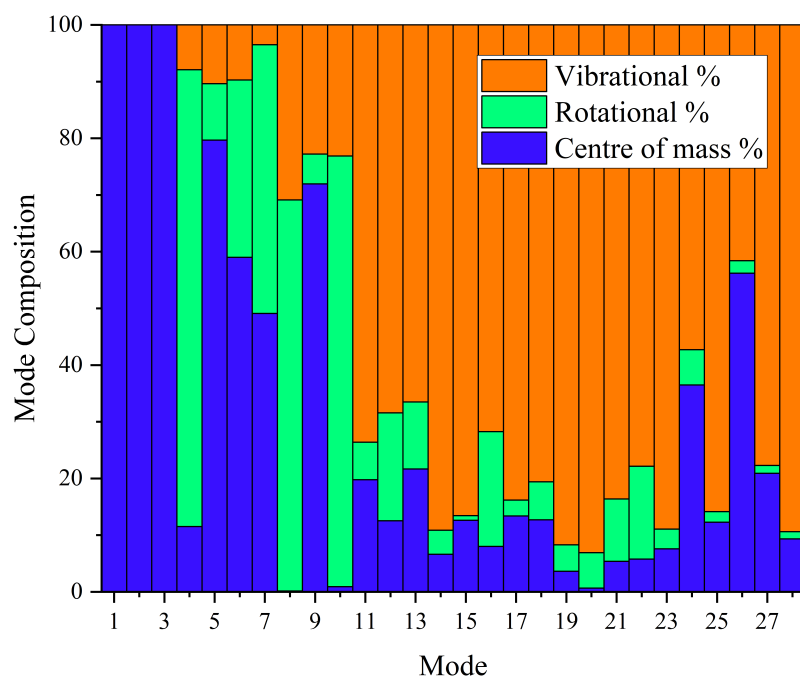
(a) D2 Mode Analysis

H
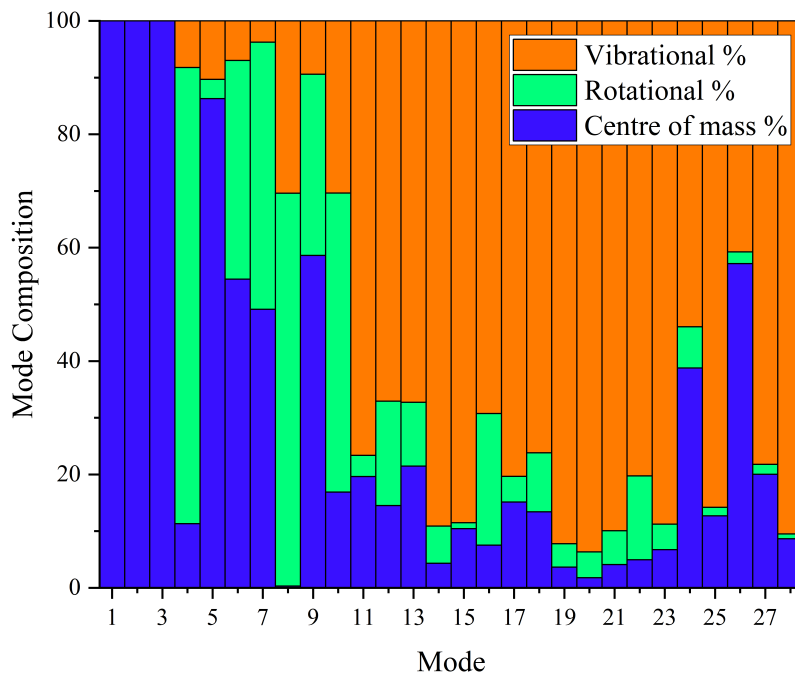
(b) D3 Mode Analysis

Figure 4.12: The mode composition of α-Lactose Monohydrate, calculated with PDielec. Both corrections produced very similar histograms indicating the underlying motions making up the modes is not particularly effected by choice of DiC.
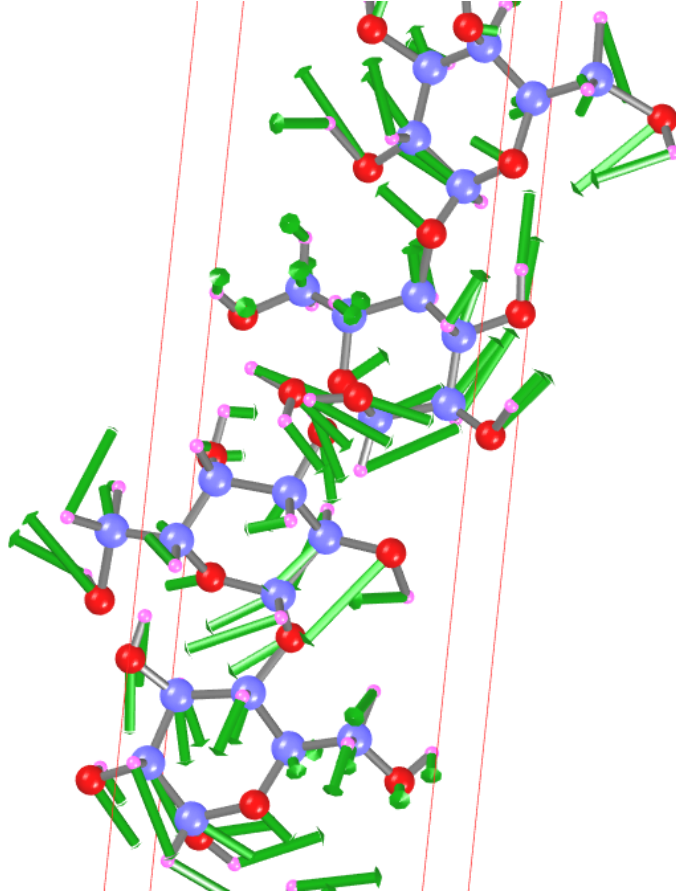
Figure 4.13: The mode at $90\,\mathrm{cm}^{-1}$ which shows the largest discrepancy between calculation and experiment. It can be seen in the top right where the OH groups are moving into each other which may not be represented well by the harmonic approximation.

to be external modes and vibrational is considered to be internal. Unlike in non-periodic systems, the internal and external modes do not have a clear separation [141] so the further breakdown is necessary. PDielec allows for the breakdown of each mode. The histograms are shown for the D2 and D3 corrections in Figure 4.12. Whilst there are some small discrepancies between them, they are largely very similar indicating that the corrections themselves did not have a significant effect on the types of phonon modes present and does not affect the order that each phonon appears on the spectrum. These graphs demonstrate the unclear boundary between internal and external modes in the THz frequency range as the lower frequency external modes all have some vibrational character and the higher frequency internal modes have some rotational and translational character. This is clearly shown by modes 24 and 26 having a significant translational component.

Whilst these histograms provide information about the breakdown between internal and external modes, they do not provide information about the breakdown of the vibrational components themselves. Using the vibanalysis [142] package provided in PDielec, where the motion of a vibrational mode is broken up and the most prominent groups of

atomic motions are presented with their respective weights. These groups are bond vibrations, angular motions between three atoms and torsional motions between four atoms. This confirmed the findings from the mode analysis of PDielec that the phonon modes themselves are very similar with only very slight differences which could contribute to the differences in frequencies. However, the findings from this package should only be used in conjunction with the other tools shown above as it was designed for the mid-IR region. In that region, there are fewer different types of motion occurring in a single mode and in the THz frequency range this calculates hundreds of contributions for each mode.

Finally, the mode at approximately $90\,\mathrm{cm}^{-1}$ shows the largest discrepancy between calculation and experiment and is shown in Figure 4.13. This could suggest that this mode has a higher degree of anharmonicity than the other modes which could be explained by the motion of the O–H groups towards each other. This will disrupt the network of H-bonds and this may not be represented well under the harmonic approximation. This mode will be examined further in Chapter 5.

4.4   Investigation into the Repeatability of Density Functional Theory Calculations

As discussed in Section 3.3.1, the ionic positions are varied until the changes between each step for the total energy and total forces of the system are below a given tolerance. Owing to the nature of how this variation is carried out, the final structure may have minute differences when several optimisations on the same structure are implemented. To ensure that this phenomenon had not impacted the comparison between DiCs, four separate optimisations and calculations of vibrational properties were performed using the D3 correction and the resulting spectra were compared to each other and to the original D3 calculation. These were performed using the same version of VASP, with identical starting structures and calculation parameters. These spectra are shown completely in Figure 4.14 where the only clear difference is the main peak at approximately $115\,\mathrm{cm}^{-1}$. However, the calculations that were performed separately from the main correction investigation show excellent agreement. This is confirmed by Figure 4.15, where the differences between each calculation are highlighted for the main group of peaks between 105 and $120\,\mathrm{cm}^{-1}$ and for the final peaks between 150 and $164\,\mathrm{cm}^{-1}$. The original calculation shows reasonable agreement with the other results below $125\,\mathrm{cm}^{-1}$ but this agreement decreases above this frequency. However, the intensities match well with the exception of the main peak at $115\,\mathrm{cm}^{-1}$. This is owing to this peak being the result of the overlap between two modes and these modes are closer together in the original calculation. However, the actual differences between these modes for the original and the new calculations are less than

$1\,\text{cm}^{-1}$ and this was determined to be satisfactory for the main DiC investigation.

Figure 4.14: The calculated THz absorption spectra of five separate optimisations using the D3 dispersion correction. With the exception of the peak at approximately $115\,\text{cm}^{-1}$, the spectra show reasonably good agreement.

4.5 Conclusion

In this chapter, the investigation into the effect of different DiCs was described. This involved performing an optimisation of the structure of αLM and calculating the THz absorption spectra using the D2, D3, D3BJ and TS corrections and determining which spectrum best matched the experimental spectrum. A numerical analysis was performed to determine which correction was most suitable for further work on materials such as αLM and other complex organic molecular crystals, and this was found to be the D3 correction although the TS correction also performed reasonably well. This was achieved through thorough direct comparison of the spectral modes and optimisation of the parameters used in PDielec to construct the spectra. The structural differences were also analysed using several methods to determine what may have caused the spectral differences. Analysis of the modes provided evidence that the dispersion only marginally changes the composition of the phonon modes which is likely the explanation for the differences in mode frequency. However, a definitive correlation between structure and mode position and intensity was not found. Finally, the repeatability of a calculation was determined through the calculation of four αLM THz absorption spectra using the

(a) *The calculated THz absorption spectra of five separate calculations using the D3 dispersion correction between 105 and* 125 cm^{-1}.

(b) *The calculated THz absorption spectra of five separate calculations using the D3 dispersion correction between 150 and* 165 cm^{-1}.
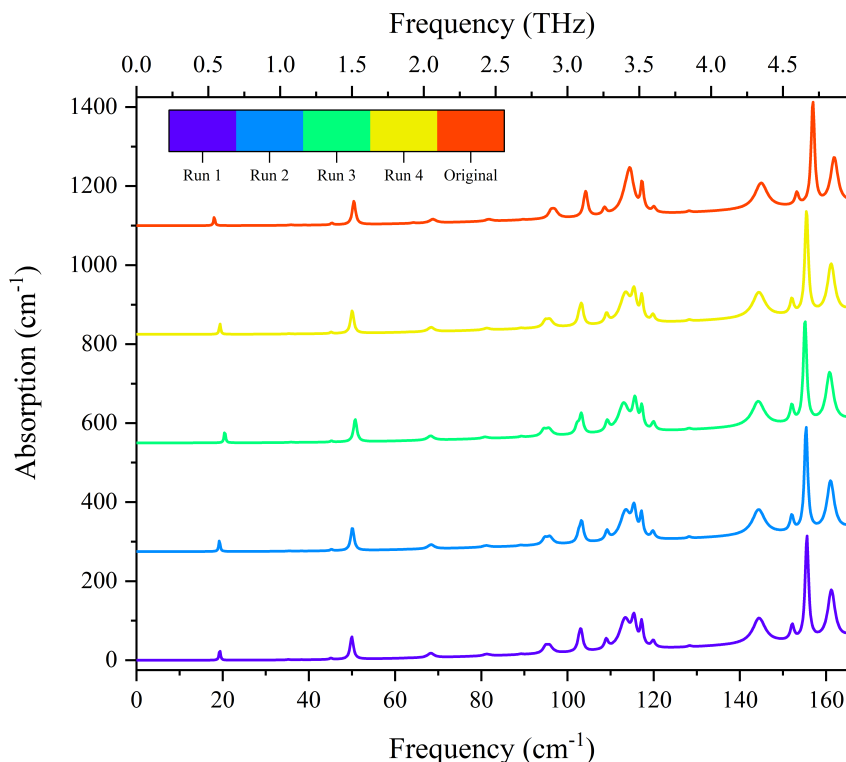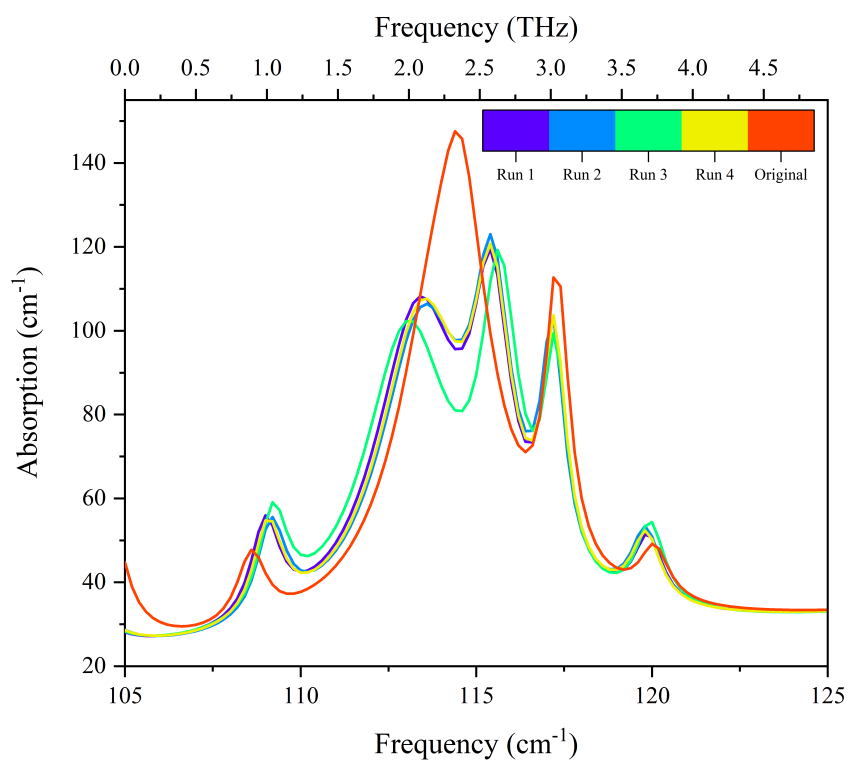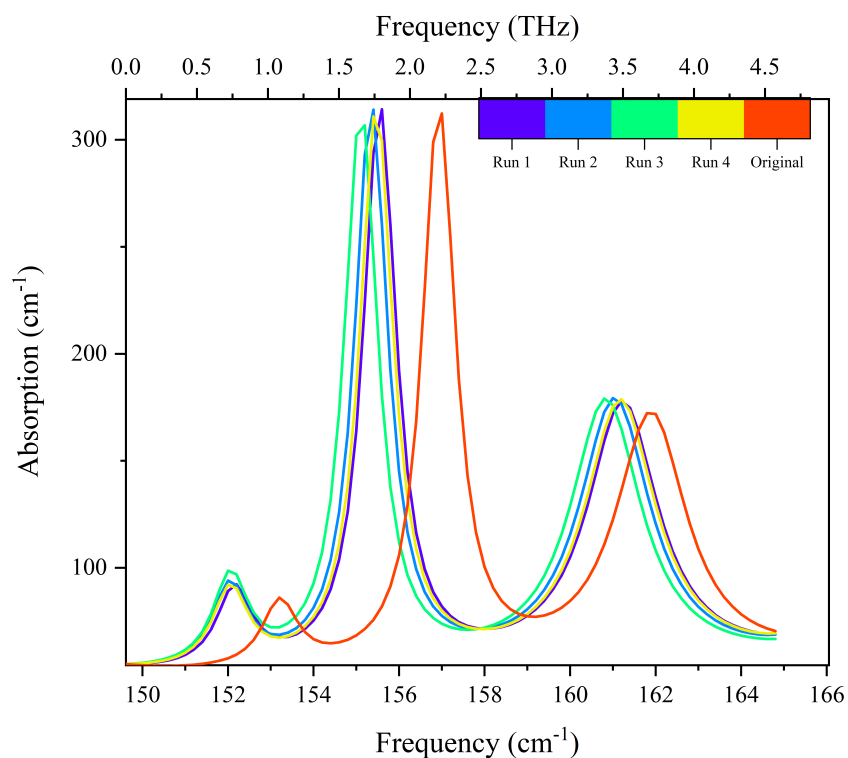
Figure 4.15: The differences between the calculated THz absorption spectra of five separate optimisations using the D3 dispersion correction.

D3 correction and these were compared to each other and to the original D3 spectrum. It was determined that below the dynamic range of the system, the differences between these calculations is tolerable.

Chapter 5

Incorporation of Anharmonicity into the Calculation of Vibrational Modes

5.1 Introduction

In Chapter 4, it was shown that it is possible to identify and analyse the modes present in a THz absorption spectrum using DFT for complex molecules such as αLM. Whilst this was mostly successful, there were some shortcomings in the calculation process that reduced comparability of the calculated and experimental spectra and demonstrated that not all the phenomena occurring in the system are being accounted for. Each mode has been modelled as a simple harmonic oscillator (HO) where the equilibrium bond lengths are independent of temperature and there is no coupling between any of these phonon modes. This simplified model of the system can be utilised when comparing to experimental spectra taken at temperatures close to $0\,\mathrm{K}$ as some of these assumptions can be considered valid in this temperature region, but without accounting for these then the complete energy landscape of the system cannot be fully understood.

Vibrations in the THz frequency range are often in excited states, even when taking spectra at low temperatures, which means that anharmonic effects should be incorporated to most accurately describe modes in this frequency range. Whilst some modes can be effectively modelled as HOs, particularly at low temperatures, this is generally an oversimplification that implies an infinite number of equally spaced vibrational energy levels. This in turn would predict that covalent bonds are stable at all temperatures which intuitively does not match experimental data. Covalent bonds have been shown to behave according to the Morse potential energy function which predicts these bonds to have a dissociation energy at which the constituent atoms overcome their mutual attraction and separate. Additionally, it also predicts that the vibrational energy level separation decreases with increasing vibrational quantum number. These predictions agree with ex-
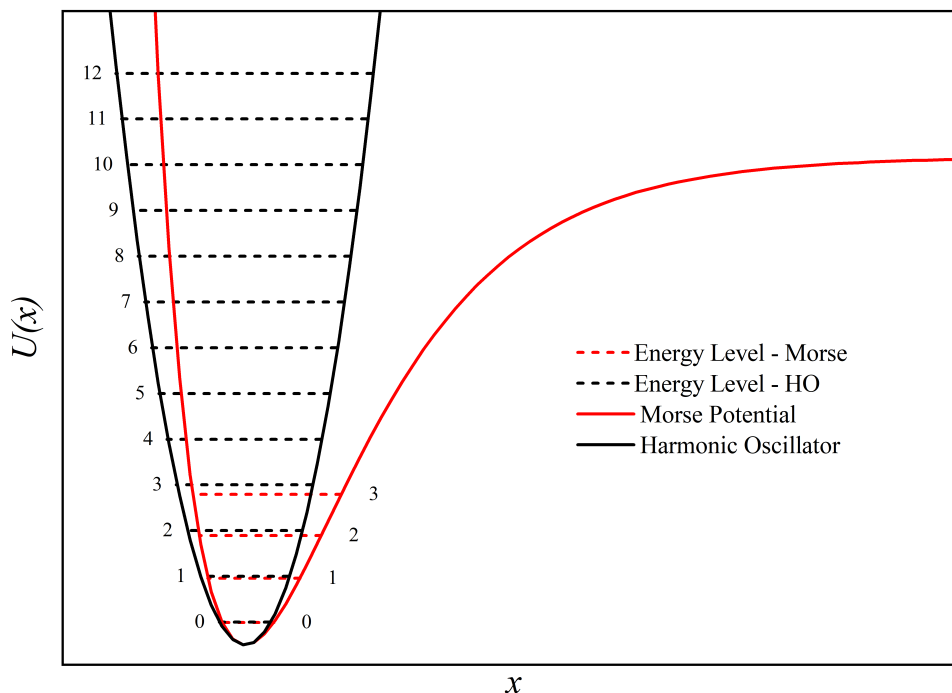
Figure 5.1: A diagram showing the vibrational energy levels of a covalent bond modelled as a harmonic oscillator and with a Morse potential. For the harmonic oscillator, the vibrational energy levels are evenly spaced and continue to infinity. When modelled with a Morse potential, the separation between energy levels gradually converges to 0 at which point the bond will dissociate.

perimentally observed phenomena and these potentials are shown for a diatomic molecule in Figure 5.1.

As described in Section 3.2.4, the energy of the system is obtained through a Taylor expansion with respect to the displacement of the nuclei from their equilibrium positions, given by:

$$\boldsymbol{E} = \boldsymbol{E}_0 + \frac{\delta \boldsymbol{E}}{\delta u}.u + \frac{1}{2!}\frac{\delta^2 \boldsymbol{E}}{\delta u^2}.u^2 + \frac{1}{3!}\frac{\delta^3 \boldsymbol{E}}{\delta u^3}.u^3 + ... \tag{5.1.1}$$

Only terms up to the term which is proportional to x^2 are usually included as this is sufficient for the calculation of the dynamical matrix. Whilst this is appropriate for approximately harmonic systems, the lack of inclusion of higher order terms removes both the inclusion of anharmonicity into the mode itself and the mode coupling that arises as a result of mode anharmonicity, as the HO model also does not incorporate interaction between modes. Without allowing for this, properties such as vibrational relaxation, phonon lifetimes and thermal conductivity will likely be incorrectly predicted. Currently, owing to the requirement of DFT for every ion to be in its ground electronic state, temperature is not incorporated which generally allows the harmonic approximation to be used. Incorporating higher order terms would allow for peak widths to be calculated from first principles rather than empirically matching to experiment. However, incorporating these higher order terms into the calculation requires using multiple unit cells which will
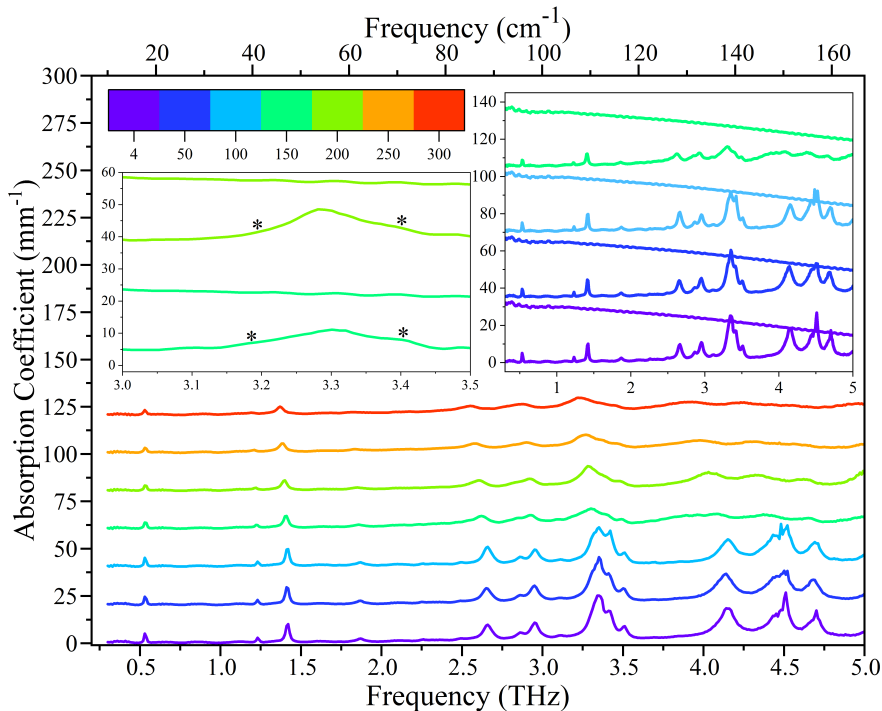
Figure 5.2: Main - The terahertz absorption spectra of α-Lactose Monohydrate between 4 and 300 K with spectra being measured in 50 K steps. Each measurement has been offset by $20\,cm^{-1}$ for clarity.

Left Inset - The absorption and maximum absorption for the 150 and 200 K measurements. Whilst it is expected that the main peak will decrease in height with increasing temperature, it is proposed that peak broadening of the starred peaks contributes to an increase in peak height for the 200 K measurement.

Right Inset - The absorption and maximum absorption for the 4 to 150 K measurements. Owing to the absorption maximum being crossed by multiple peaks, the 150 K measurement is the first measurement that can be considered completely accurate.

drastically increase the computational resources required to the point of unfeasibility for large systems with complex bonding such as αLM, but has been demonstrated for less complicated systems [143]. For isolated HOs, the mode frequencies are not dependent on interatomic distances and the equilibrium volume of a crystal does not depend on temperature. It is known that thermal expansion occurs in nearly all systems which manifests in a temperature dependence of equilibrium bond lengths and αLM also follows this trend [135, 144].

5.1.1 Terahertz Time-Domain Spectroscopy with Variable Temperature

The THz absorption spectra of αLM between 4 and 300 K are shown in Figure 5.2. This was accomplished by taking a spectrum at 300 K and then cooling the sample to 4 K where a spectrum was taken. The sample was then allowed to warm up and subsequent spectra were taken at each 50 K step, culminating in a final spectrum taken at 300 K where the best of the two was selected.

The spectra change significantly as temperature is increased, which is mostly the result of homogeneous peak broadening owing to increased thermal motion across the entire spectrum. This is a result of thermal broadening and is common for THz absorption spectra. Additionally, at $10\,\mathrm{K}$ only the first vibrational energy level will be populated but at $300\,\mathrm{K}$, $k_B T$ is approximately equal to $6.1\,\mathrm{THz}$ so multiple energy levels will be populated which leads to further peak broadening. The peak positions themselves tend to shift to lower frequencies for all peaks with the exception of the first peak, and this is shown in Figure 5.3b. The five modes shown are indicated in Figure 5.3a with an asterisk, and these peaks have been chosen owing to their visibility throughout the temperature range in question. These five peaks will be referred to as Mode 1 to Mode 5 respectively from now on, for brevity. This red-shifting of the mode frequency is a common trend for modes in the THz frequency range [145] and is believed to arise from the anharmonicity of a given mode, with some exceptions where the peak will shift to a higher frequency [21]. The stability of the first mode with temperature may demonstrate the harmonic nature of this mode. Finally, it can be seen that above $150\,\mathrm{K}$ the peak heights drastically drop and comparison becomes more challenging. For this reason, all subsequent analysis will be performed on data up to $3.5\,\mathrm{THz}$. It should be noted that only the peak heights for $150\,\mathrm{K}$ and above can be considered accurate as the maximum absorption value is reached below this temperature. The increase in peak height between 150 and $200\,\mathrm{K}$ is believed to be owing to thermal broadening as indicated by the left inset in Figure 5.2.

An additional benefit of incorporating anharmonicity allows prediction of the spectrum with temperature effects included. This can reduce the need to take experimental spectra at $4\,\mathrm{K}$ which significantly complicates the process. Reaching these temperatures requires liquid He which is costly, hazardous and increases the complexity of the experimental apparatus required. It would be beneficial to not have to use any cooling methods and perform the same degree of analysis on a spectrum taken at room temperature. Whilst the anharmonic terms of the Taylor expansion of the energy of the system is an extremely computationally costly method of understanding the full energy landscape, there are other methods that can be used to understand the effect of temperature and anharmonicity on systems. One of the most prevalent of these is molecular dynamics (MD) simulations.

5.1.2 Molecular Dynamics

MD simulations are a class of computational simulations that model the movement of particles, which can be atoms or entire molecules [146]. If the forces between particles can be calculated, this can be turned into a trajectory that the particle will move along within a given time step. This allows the dynamical behavior of a system to be studied as long as the potentials between particles is correctly modelled and the time step is similar to the time scale of the phenomena being studied. Vibrational motion can be considered
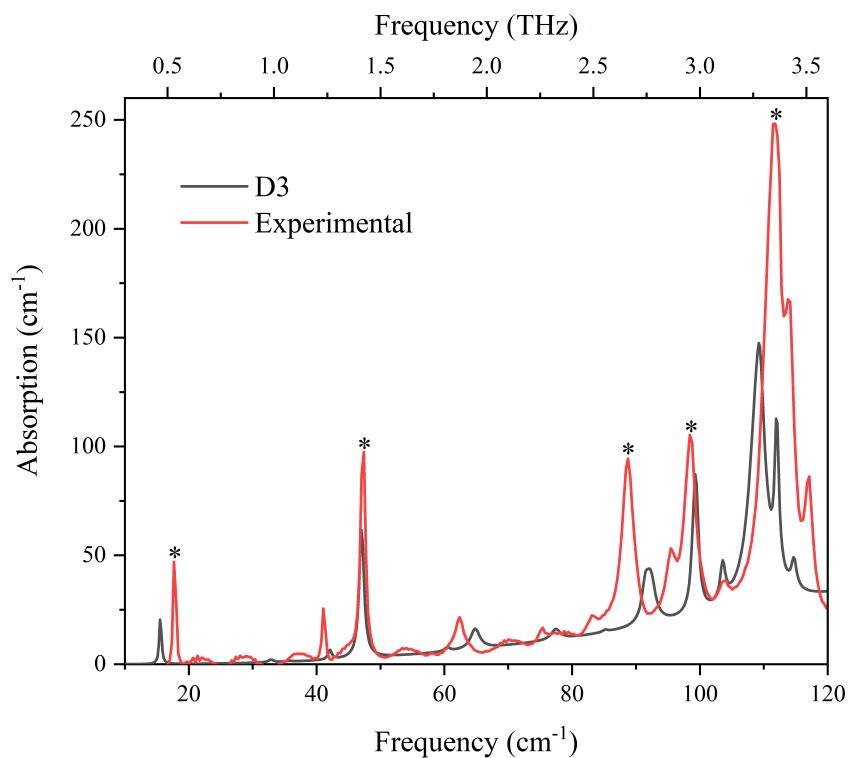
(a) *The calculated terahertz absorption spectrum using the harmonic approximation. The starred peaks are the modes selected for further investigation.*
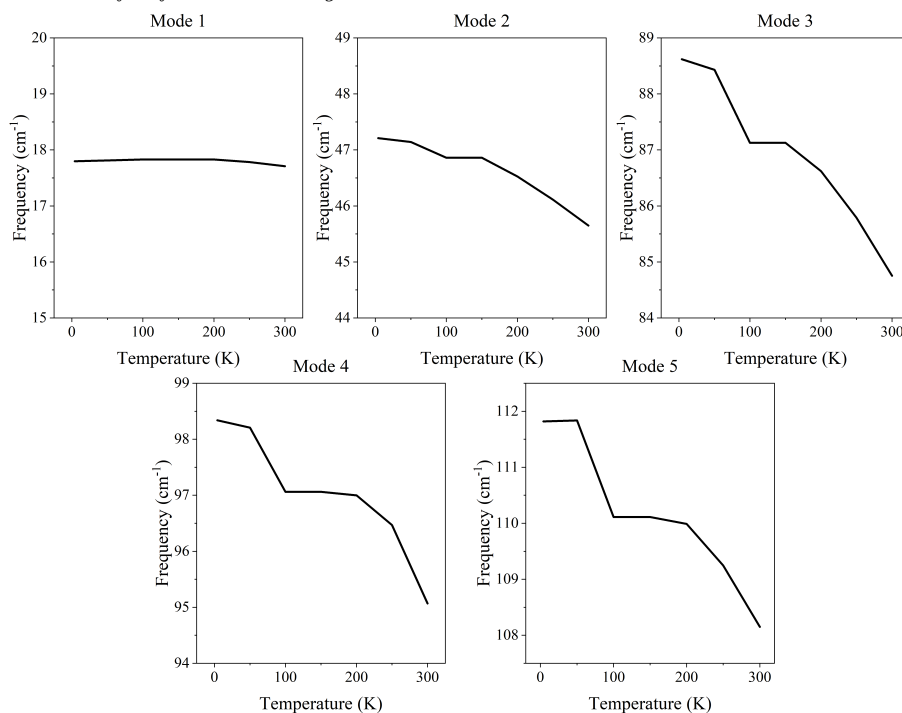
(b) *Experimental peak widths as a function of temperature for the starred peaks shown above.*

Figure 5.3: The terahertz absorption spectrum using the harmonic approximation and the temperature dependence of the experimental peak widths.

to be a collection of atoms or molecules moving along repeated trajectories and so is appropriate for study by MD.

Temperature can be calculated using both the kinetic temperature, where the temperature is a function of the total kinetic energy of the constituent particles and the canonical probability distribution function which uses the Boltzmann distribution [147]. This allows temperature to be controlled using a thermostat, which is simply an algorithm that prevents the system from leaving thermal equilibrium. There are many different variations of this algorithm, including the Nose-Hoover thermostat [148] and the Braga-Travis thermostat [149] but all suffer from some form of limitation. These have been used for predicting THz absorbance spectra [150] but this was most successful for spectra taken at temperatures close to 0 K.

One of the most significant challenges of this type of simulation is modelling the inter-particle potentials correctly and has led to the development of several sub-categories of MD. If these potentials are incorrectly modelled then any vibrational data that can be extracted will not be accurate. Traditionally, these were derived from empirical data extracted from the experimental spectra [151–153] but can also be constructed through first principles methods [154]. One method that has shown much success is *ab initio* MD [155] which uses first-principles methods such as DFT to calculate the inter-particle potentials [156]. By repeating the simulation multiple times, the statistical distribution of the possible evolutions of a system can be measured. MD simulations are able to explore the potential energy surface without the limitations of the harmonic approximation but the nature of the mode can be challenging to determine, limiting their overall utility for interpreting experimental vibrational spectra. Whilst anharmonic properties of the mode such as phonon lifetime and coupling can be determined, this is prohibitively expensive for complex organic systems such as αLM and so has not been attempted in this work.

5.2   The Quasi-Harmonic Approximation

Some degree of the anharmonic behaviour of a system can also be calculated using another method, which is by using the the Quasi-Harmonic Approximation (QHA). Phenomena such as thermal expansion cannot be reproduced using the harmonic approximation owing to the frequency of each mode being independent of temperature [157]. This method is based on the assumption that the harmonic nature of vibrational motion is valid for all values of a given lattice constant which controls the volume of a crystalline system's unit cell. This allows the volume of a system to behave as a proxy for temperature and the thermodynamical properties dependent on temperature can be extracted. Through this, the harmonic approximation that underpins most vibrational calculations holds true for each volume whilst the increased volume as temperature increases can be accounted for.

Using DFT with the method described in Section 3.3.1, where the optimisation of atomic positions was achieved using the VASP package and the dynamical matrix was

calculated using Phonopy with VASP as the computational engine. Five unit cells were generated with volumes between 766.47–781.57 Å, with differences of approximately 3.8 Å^3 between them. The volume and corresponding total energy of each cell is shown in Figure 5.4. αLM has a symmetry of P_{21} which must be conserved when expanding the unit cell. Initial cell choice ranges were 99–104% of the optimised unit cell volume. but this resulted in a volume-temperature curve which did not overlap with the optimised unit cell volume at 0 K. Smaller increments were then attempted with a range of 101.5–103.5% which were more successful. Five were chosen as this is the minimum number of volumes required but more would improve the accuracy of the calculations. However, owing to the size of the αLM unit cell this was decided to be prohibitively expensive in terms of computational resources.
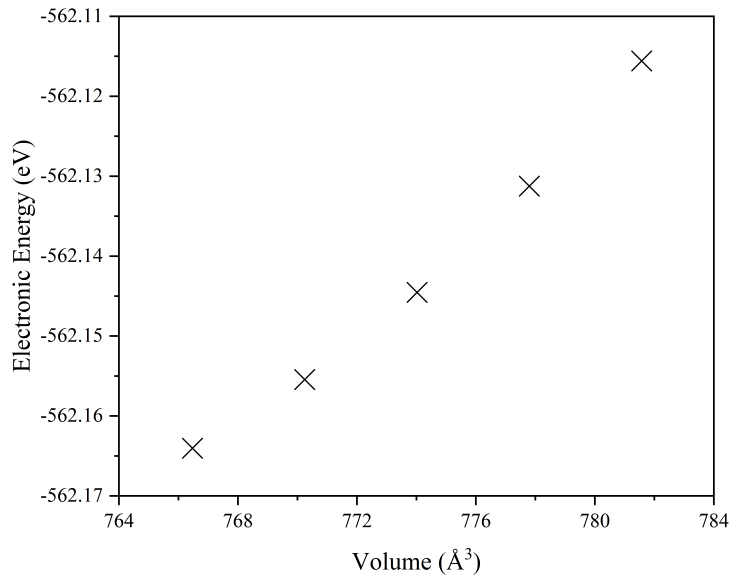
Figure 5.4: The volumes and corresponding energies of the five unit cells used to calculate the thermal properties of the system under the quasi-harmonic approximation.

Whilst keeping the cell dimensions fixed, the atoms were allowed to relax to their lowest energy state and the dynamical matrix was calculated for each volume. The phonon frequencies were extracted and these are then used to derive the thermal properties for the system by using the relationship:

$$G_{T,p} = min[U(V) + F_{phonon}(T;V) + pV] \tag{5.2.1}$$

where $G_{T,p}$ is the Gibbs free energy at constant temperature and pressure, $U(V)$ is the total internal energy at constant volume p is the pressure, V is the unit cell volume and $F_{phonon}(T;V)$ is the phonon Helmholtz free energy for a given temperature and volume. This is given by:

$$F_{phonon} = \frac{1}{2} \sum_{\mathbf{q},\nu} \hbar\omega_{\mathbf{q}} + k_B T \sum_{\mathbf{q}} ln[1 - exp(\frac{-\hbar\omega_{\mathbf{q}}}{k_B T})] \qquad (5.2.2)$$

where $\hbar$ is the reduced Planck constant, $\omega_{\mathbf{q},\nu}$ is the phonon frequency at wave vector $\mathbf{q}$ and k_B is the Boltzmann constant. By finding the minima of Equation (5.2.1) for each desired temperature, properties such as the thermal expansion of the system and heat capacity at constant pressure, $C_p(T, p)$, can be calculated using these minima and thermodynamic relations such as:

$$C_p(T, p) = -T\frac{\delta^2 G(T, p)}{\delta T^2} = T\frac{\delta V(T, p)}{\delta T}\frac{\delta S(T; V)}{\delta V}\bigg|_{V=VT,p} \qquad (5.2.3)$$

where $V(T, p)$ is the equilibrium volume at T and p.

5.3 Analysis and Results

5.3.1 Thermal Expansion

The relationship between volume and temperature is shown in Figure 5.5a and its derivative, the thermal expansion coefficient, is shown in Figure 5.5b. This gives unit cell volumes of 768.97 and 771.86 Å^3 for 150 and 300 K respectively.

(a) Temp Vol   (b) Therm Exp
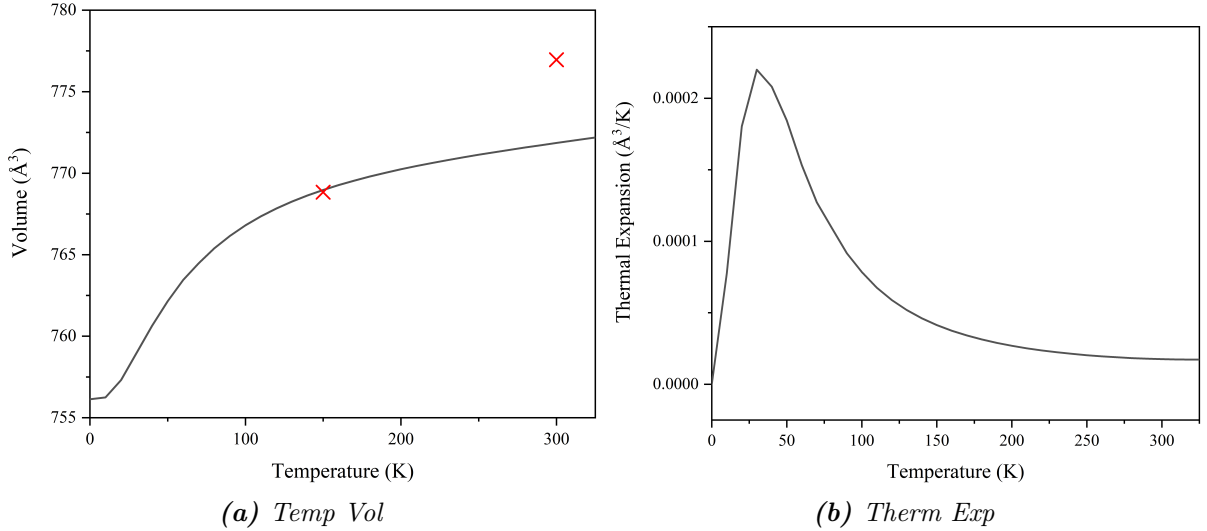
Figure 5.5: The calculated volume-temperature relationship and thermal expansion of α-Lactose Monohydrate. This curve shows reasonable agreement with experimental values, shown in red.

The experimental unit cell volume at 150 K is 768.84 Å^3 [135] which is a difference of 0.016% with the calculated value and the experimental volume at 300 K is 776.96 Å^3 [144], which is a difference of 0.66%. Both of these differences are very small so this volume

temperature curve can be assumed to be reasonably reliable up to 300 K but this difference indicates that the thermal expansion is being underestimated to some degree. This would be confirmed by more experimental measurements of the unit cell volume at different temperatures but these were not available. Synthesis of single crystals of αLM and subsequent measurements by XRD of the unit cell volume at a wider range of temperatures was attempted but was stopped owing to limited access to suitable facilities during the COVID pandemic.

5.3.2 Heat Capacity

Additionally, the heat capacity at constant pressure is shown in Figure 5.6. The heat capacity shows a mostly linear trend of increasing with temperature which is expected as nearly all systems become more difficult to heat as their temperature increases. However, the experimental value at 300 K, obtained by differential scanning calorimetry, is $1.22 \, \mathrm{JK^{-1}g^{-1}}$ [158], which shows significant disagreement with the calculated value of $2.18 \, \mathrm{JK^{-1}g^{-1}}$. This is an increase of 78.9%.

Whilst the QHA has been used to successfully calculate the heat capacities of a range of molecular crystals [159], these were all small molecules when compared to α-Lactose and the unit cell did not contain any other species such as water. These factors will complicate the calculation process and will result in larger discrepancies between calculation and experiment. Mathews *et. al.* [160] showed that the heat capacities calculated using the QHA begin to deviate from experiment at approximately 50 K for various organic hydrate ices which are more comparable to αLM which may explain the poor experimental comparability for this calculation as αLM is a hydrate and incorporating the effects of the crystalline water molecules is challenging.

5.4 Temperature Dependence of Calculated Terahertz Spectra

5.4.1 Temperature Dependence of Phonon Frequency

Now that the volume of the unit cell has been calculated as a function of temperature, it is possible to calculate the dynamical matrix, and therefore phonon properties, at different temperatures. This was done by creating structures with a unit cell volume corresponding to a particular temperature from Figure 5.5a and optimising the ionic positions. The calculated frequencies for the modes selected in Figure 5.3 as a function of temperature are shown in Figure 5.7, alongside the experimental frequencies and the
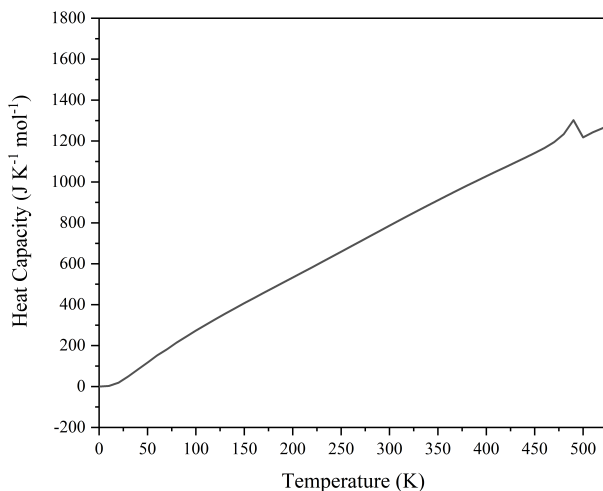
Figure 5.6: The calculated heat capacity at constant pressure of α-Lactose Monohydrate. Whilst the absolute values show discrepencies with experiment, the shape of the curve is expected for a material who's heat capacity has been calculated using the Debye model.

frequency calculated without using the QHA.

This was partially successful with the correct trend of frequency decreasing with temperature was predicted for Mode 2 to Mode 5. However, there are disagreements of up to nearly $10\,\mathrm{cm}^{-1}$ which is over 10% of the value and would be considered a large discrepancy. This discrepancy seems to increase with temperature for all modes. The large disagreement for Mode 3 is similar to that shown in Section 4.3.3 where it was also poorly represented by the HO. For Mode 1 however, these calculations were less successful. Whilst Mode 1 does not change with temperature experimentally, it has been calculated to slightly increase with temperature. The error bar shown on the red trace is the standard deviation of this mode's frequency, calculated using the calculations presented in Section 4.4 and the error bar on the blue trace is the experimental frequency resolution which is $0.33\,\mathrm{cm}^{-1}$. It is assumed that the calculated error is similar across all temperatures. For Mode 1, it is possible that this temperature shift is just within the margin of error for these calculations but if this is not the cause then this mode has been poorly modelled owing to the rarity of a positive frequency shift with temperature and this does not agree with experiment. Additionally, Mode 2 was calculated to have a very slight temperature dependence which matches experiment but is close to being within the margin of error for these calculations. All mode frequencies were overestimated when compared to their experimental values. Mode 2 through to Mode 5 have temperature dependencies that are smaller than their experimental counterparts which manifests as a shallower gradient with the possible exception of Mode 4 which has the best overall correlation with experiment.

The mode Grüneisen parameter is a quantity that describes how a given mode's frequency will change with the volume of the unit cell. When considering the harmonic

(a) *Mode 1 Temperature Dependence*

(b) *Mode 2 Temperature Dependence*

(c) *Mode 3 Temperature Dependence*

(d) *Mode 4 Temperature Dependence*

(e) *Mode 5 Temperature Dependence*
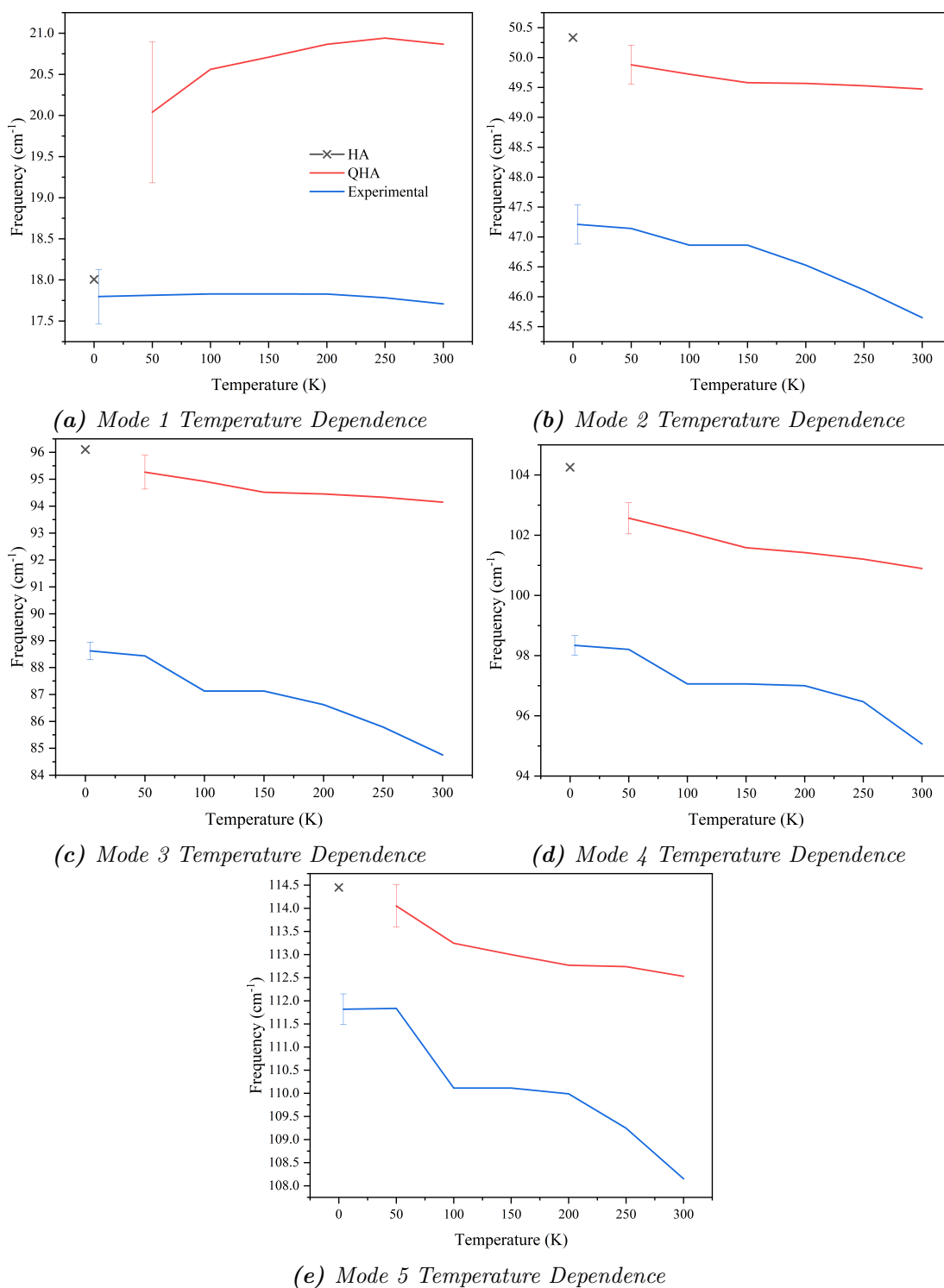
Figure 5.7: The calculated and experimental mode frequencies as a function of temperature. All modes show an expected trend of decreasing frequency with temperature with the exception of Mode 1. The error bars arise from the standard deviation of multiple identical calculations, assumed to be similar across the temperature range, and the experimental frequency resolution. The original calculation's results are marked with crosses, while the calculated results using the QHA are shown in red. Finally, the experimental results are shown in blue.

approximation, the mode Grüneisen parameter should be zero for every mode as the restoring force acting on an ion or molecule will be linear. By varying the volume and using the QHA, the mode Grüneisen parameter can be calculated and these are shown for modes up to 3.5 THz in Figure 5.8 where the modes in red "+" symbols are Mode 1 to Mode 5 for clarity. A positive value indicates that the frequency decreases with temperature and a larger value indicates that the frequency will decrease more rapidly with temperature. Conversely, a negative value indicates that the frequency will increase with temperature. These values corroborate the trends seen in Figure 5.7, with Mode 4 having the greatest frequency shift with temperature and Mode 1 having a negative mode Grüneisen parameter. The value is large owing to the low frequency in this mode and so any shift is proportionally larger.
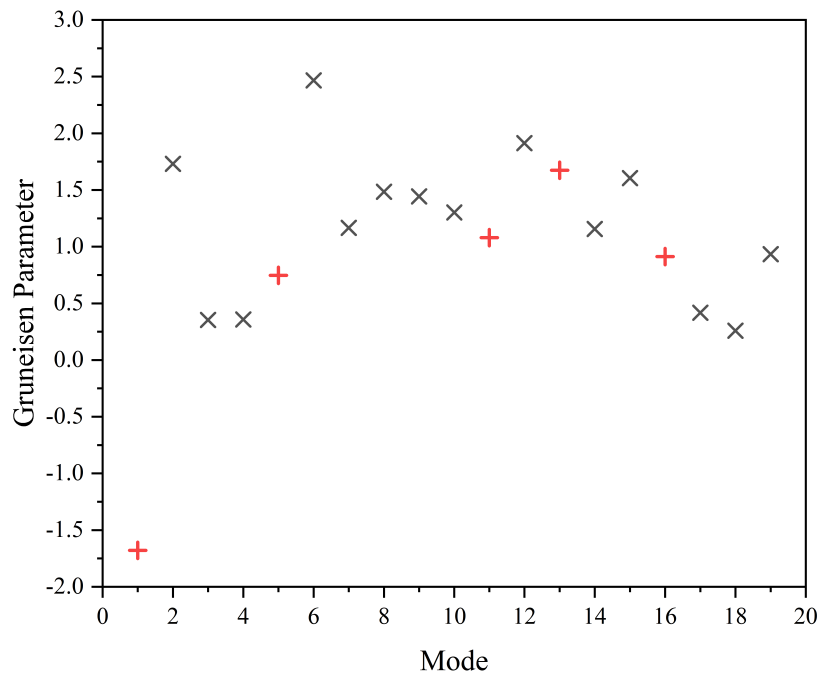
Figure 5.8: The calculated mode Grüneisen parameters for each mode of α-Lactose Monohydrate under $125\,\mathrm{cm}^{-1}$. The only mode with a negative mode Grüneisen parameter is Mode 1.

5.4.2 Calculation of Terahertz Absorption Spectrum at Room Temperature

Now that the unit-cell volume at 300 K is known, a structure that has this volume can be created. The atomic positions can then be optimised, without altering the unit-cell dimensions, and the dynamical matrix can be calculated to produce a calculated THz absorption spectrum that should more closely represent the experimental spectrum at 300 K. These are both shown in Figure 5.9, where the 300 and 4 K spectra are shown for comparison. This was achieved using experimental peak widths for the five major peaks and a default peak width of $5\,\mathrm{cm}^{-1}$, an air void radius of $10\,\mathrm{\mu m}$ and void volume

(a) *The experimental and calculated spectra at* 300 K

(b) *The experimental and calculated spectra at* 4 K
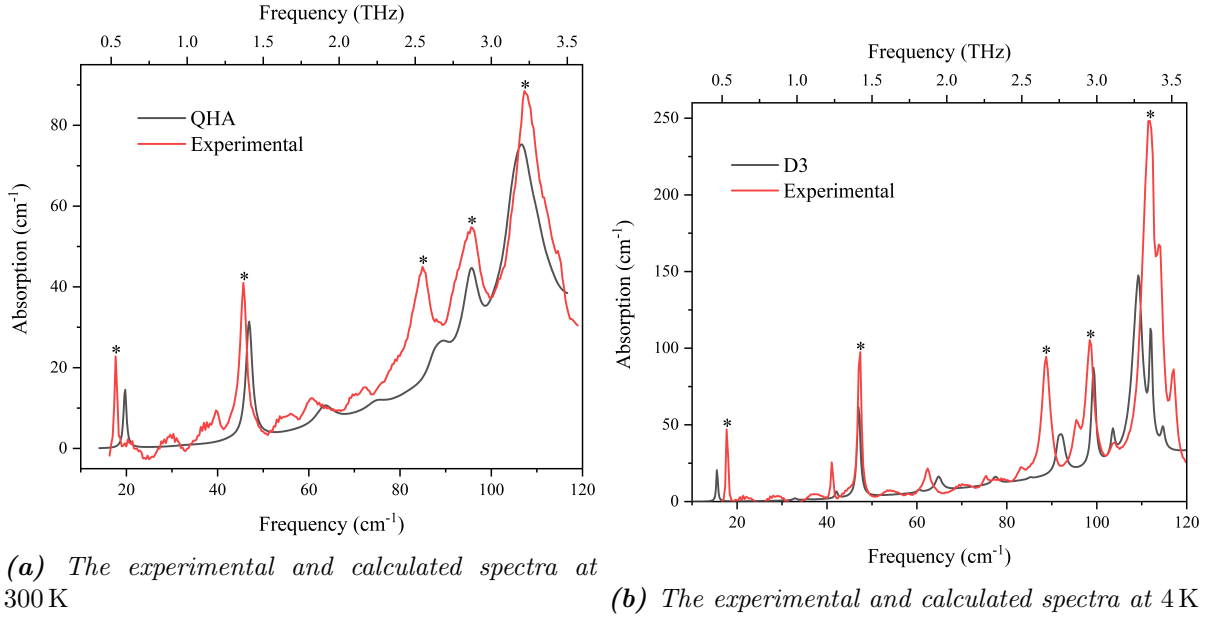
Figure 5.9: The experimental and calculated terahertz absorption spectra at 300 and 4 K respectively. The spectrum calculated at 300 K shows greater correlation with experiment than the spectrum taken at 4 K and the calculated intensities also show greater agreement.

fraction of 7%. This was selected to best match the rising background absorption at approximately 3 THz and is larger than was used in Chapter 4 but as this is at a much higher temperature, contraction of these voids owing to expansion of the PTFE and αLM may account for this. The experimental spectrum contained features that were undesirable and would reduce correlation. Issues with the reference measurement resulted in an offset that artificially increased the calculated intensities. Additionally, reflections on the cryostat window resulted in the etalons that are visible in the experimental spectra. The experimental spectra has been offset by 9 and 3.5 cm^{-1} respectively so that the etalons oscillate approximately around 0 cm^{-1}. This is with the aim of giving the fairest comparison between experiment and calculation at both temperatures.

The spectrum calculated at 300 K shows excellent agreement with experiment, having an x-correlation value of 0.9416 and an RMS error of 0.0969 with a frequency shift of $-0.2\,cm^{-1}$ and a frequency scaling value of 0.95. This is significantly better than the spectrum calculated using the harmonic approximation when comparing to the spectrum measured at 4 K which has an x-correlation of 0.8749 and an RMS error of 0.106 in this frequency range. This is likely to be caused by the much finer detail within the 4 K spectrum which would increase the complexity of exactly matching the experimental spectrum. Nearly all peaks show very good agreement across experiment and theory with the exception of the experimental peak at approximately 85 cm^{-1}. This is the mode that also showed the most disagreement at 4 K and the degree of mismatch has not increased. This means that what is causing the disagreement is either not affected by temperature or that the shift is consistent across experiment and calculation as temperature increases.
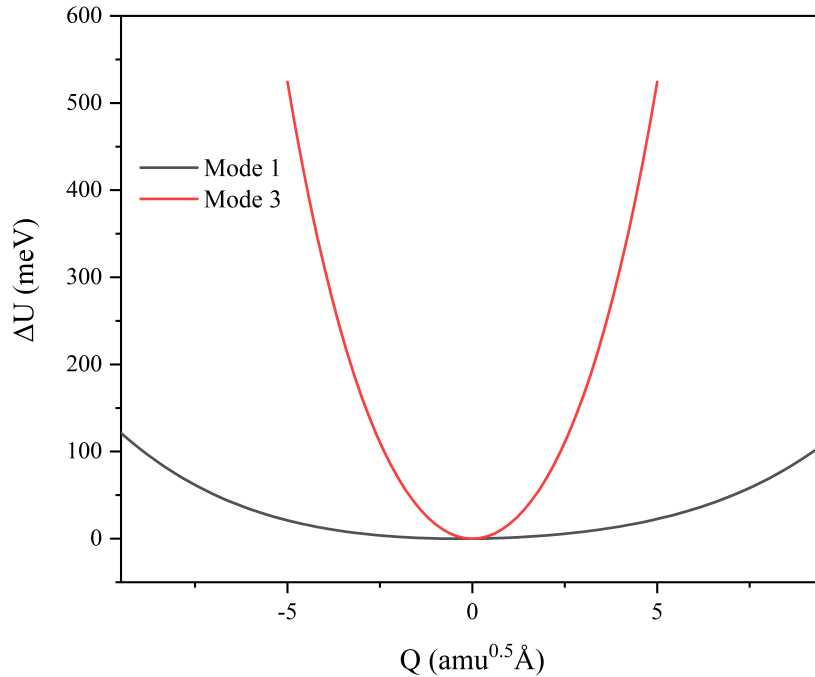
Figure 5.10: The change in the potential energy surface as Mode 1 and Mode 3 are projected along the phonon coordinates.

The ratio of intensities between experiment and calculation is also better than for $4\,K$ which may be a result of the increased background absorption at higher temperatures.

One possible explanation of the large discrepancy between the calculated and experimental frequencies of Mode 3 is the impact this mode has on the surrounding structure. As shown in Figure 4.13, Mode 3 consists of a number of $O–H$ groups oscillating close to each other. This is expected to drastically increase the change in total energy over the course of the oscillation when compared to, for example, Mode 1. This is shown in Figure 5.10, where a method developed by Skelton *et. al.* [161] allows for the mapping of the potential energy surface along a phonon coordinate and has been applied to Mode 1 and Mode 3. It is clear the potential for Mode 3 is much steeper than for Mode 1 which is expected owing to their relative motions. Mode 1 is expected to be the most harmonic mode but when projected out using this method and compared to Mode 3 this is not clear. Owing to time constraints, this phenomena and the other modes present in the spectrum were not able to be analysed.

5.5 Conclusion

In conclusion, the QHA approximation was used to calculate the thermodynamic properties and temperature-dependent phonon frequencies of αLM. This was used to calculate the THz absorption spectra at room temperature which had not previously been achieved by this group. Lastly, several modes and their trends with temperature were examined.

This investigation produced both successes and failures, with the prediction of the unit cell volume at $300\,\mathrm{K}$ being less than 1% off the experimental value. The heat capacity of the system seemed to be drastically overestimated, being over by 78.9% but this is not entirely unexpected for a system as large as αLM. However the production of the spectrum at room temperature can be considered a success owing to high degree of correlation with an experimental spectrum taken at room temperature. This should allow for simpler experimental setups that do not have to incorporate space for cryogenic apparatus and reduces the cost and risk of the measurement. However, at present this will be limited to systems where the number and environment of electrons is similar to αLM as the computational time to optimise and calculate phonon properties for all the volumes required is incredibly time-consuming. Larger systems or systems involving large numbers of electrons, such as metals, could be analysed using this method but the required computational resources would be incredibly large.

Chapter 6

Investigation into the Effect of Small Gap-Sizes on the Terahertz Output of Photoconductive Switches

6.1 Introduction

Whilst most of this project has focused on improving the interpretation of THz-TDS, this is not the only challenge for widespread utilisation of this type of spectroscopy within the chemical community. As discussed in Chapter 2, the experimental apparatus at the University of Leeds for taking these spectra tends to be bulky, complicated to set-up and come with operational and maintenance challenges. Ti:Sapphire lasers have been the primary method of generating femtosecond 800 nm pulses [162] but these can suffer from power drift and instability during operation, arising most prominently from temperature fluctuations and resulting in inconsistencies in measurements. Additionally, most sample measurements are performed in a transmission set-up which necessitates the use of non-absorbing matrix materials such as PTFE, owing to strong absorptions above the dynamic ranges of these systems when using pure samples [17, 163, 164]. This increases sample preparation complexity and introduces spectral artifacts into the measurements that increase the difficulty of interpretation. Measurements in reflection geometry can be incredibly difficult to align and creating a suitable reference measurement for spectroscopy is also challenging [163]. Finally, reflections from both emitters and detectors cause oscillations in the TD that reduce spectral resolution.

With these problems in mind, it was decided to design a new system to address some of these issues. This system is based around the use of a 150 mW Toptica Fibre laser. Fibre lasers show more temperature stability than Ti:Sapphire lasers, so there will be less power drift across separate measurements and the consistency of measurements

performed using the set-up will be increased. Initially, the system will be built with the sample in a traditional transmission geometry for ease of alignment and construction but this will be replaced with an Attenuated Total Reflectance (ATR) accessory. These are used extensively for mid-IR spectroscopy. This accessory will primarily be used to bypass issues with sample permittivity and certain types of spectral artifacts, such as Mie scattering, but eventually will also be used to allow measurements using the full IR range under identical experimental conditions. All of these improvements should drastically improve the comparability of calculated and experimental spectra and so should increase the accessibility of THz-TDS.

6.2   Investigation into the Effect of Gap Size on the output of a Photoconductive Switch

Owing to the much lower power output of the fibre laser and the corresponding smaller laser spot size, the larger 100 and 200 μm gap-size PC switches, currently in use in System 1 which is described in Section 2.2.1, would be inefficient for this purpose. These devices would have significant unilluminated portions which would significantly decrease SNR. Whilst some 10 μm devices have been used by this group in the past, it was decided that an investigation into an optimal device gap-size for lower laser power systems would be beneficial.

The sizes chosen for this study were 5, 10, 20 and 40 μm owing to the expected incident power of 65-70 mW on the emitter. This is a result of the splitting of the incident pulse into separate beams for emitter and detector and system losses before the emitter. It is estimated that the 5 μm will produce the highest output signal for a given optical power owing to the inverse relationship between gap size and generated signal, but there are other factors that should also be considered. It was decided that the device should be close to saturation at an incident power just above 70 mW, which will reduce the magnitude of fluctuations in the device's output resulting from fluctuations in laser power. Saturation, described in Section 2.1.1, is when increasing incident optical power or applied bias results in a smaller and smaller increase in device output culminating in no increase and eventual damage to the device. This occurs primarily owing to heating in the device and electrical screening from the induced photocurrent. Even with the increased stability of the fibre laser, this is a desirable property. Finally, ease-of-alignment should also be considered as the smaller gap-sizes can be challenging and time-consuming to optimally align. It should also be considered that when focused onto the emitter, the laser spot has a diameter of approximately 30–40 μm which will mean that, with the exception of the 40 μm devices, each gap will not receive 100% of the incident optical pulse. The desirable device will

have the highest output power while still being relatively easy to align and should begin to saturate around 70 mW.

6.2.1   Fabrication of Photoconductive Switches

The fabrication of efficient PC switches for use in the THz region is non-trivial and comes with many challenges. The method described below, and shown in Figure 6.1, for the fabrication of these devices onto a sapphire substrate was adapted from Bacon *et. al.* [165]. This method was also used to produce the devices with a SI-GaAs substrate but without the substrate transfer steps. For all devices, the material used to generate the THz radiation was LT-GaAs and when discussing these devices, they will be differentiated by their substrate material alone.

A 2 µm thick layer of LT-$GaAs$ was grown, using molecular beam epitaxy at 210 °C, on a 100 nm thick AlAs layer, which was itself grown on a 500 µm thick SI-GaAs wafer. This is scribed into 2.5 mm^2 pieces which were placed into a beaker containing acetone and positioned in an ultrasonic bath for 5 minutes on 10% power to avoid damage. This was repeated using isopropyl alcohol (IPA) to remove any inorganic impurities left on the surface. The final step of the cleaning process involved placing the sample onto a hot plate at 200 °C for 5 minutes which will remove any excess moisture. The sample was then placed in a rapid thermal annealer for 15 minutes at 550 °C. The LT-GaAs layer on the top of the wafer undergoes epitaxial lift-off where it is removed from the SI-GaAs substrate. AZ4562 photoresist was applied around the edges of the sample as a barrier as protective wax (Wax W, Apiezon) was melted, using a hotplate at 100 °C, onto the surface of the LT-GaAs. The sample was then placed in a sulphuric etch solution, consisting of $H_2SO_4 : H_2O_2 : H_2O$ (1:40:80 by volume), for 5 minutes to expose the AlAs layer, and then into a dilute HF solution consisting of HF:H_2O (1:9 by volume) for 24 hours at 4 °C to remove the AlAs. Once free, the LT-GaAs layer, supported by the wax, was transferred onto a clean sapphire substrate and left for approximately one week to allow the excess moisture between the layers to evaporate and bonding to occur. The wax was removed with trichloroethylene and the samples placed in a vacuum oven, for 15 hours at 250 °C and 20 mbar, which ensures the removal of any excess moisture and aid further adhesion. After the liftoff and transfer process, devices have been made using both the LT-GaAs on substrate and the original LT-GaAs on SI-GaAs and the subsequent fabrication process for both types of devices are identical.

To perform photolithography on the sample, a bi-layer resist process is used. This ensures an effective undercut which is vital for the lift-off process and owing to the S1813 photoresist's poor adhesion with the sapphire substrate. Initially, a primer layer of hexamethyldisilazane is spun onto the surface of sample for 30 s at 2000 rpm, ensuring coverage
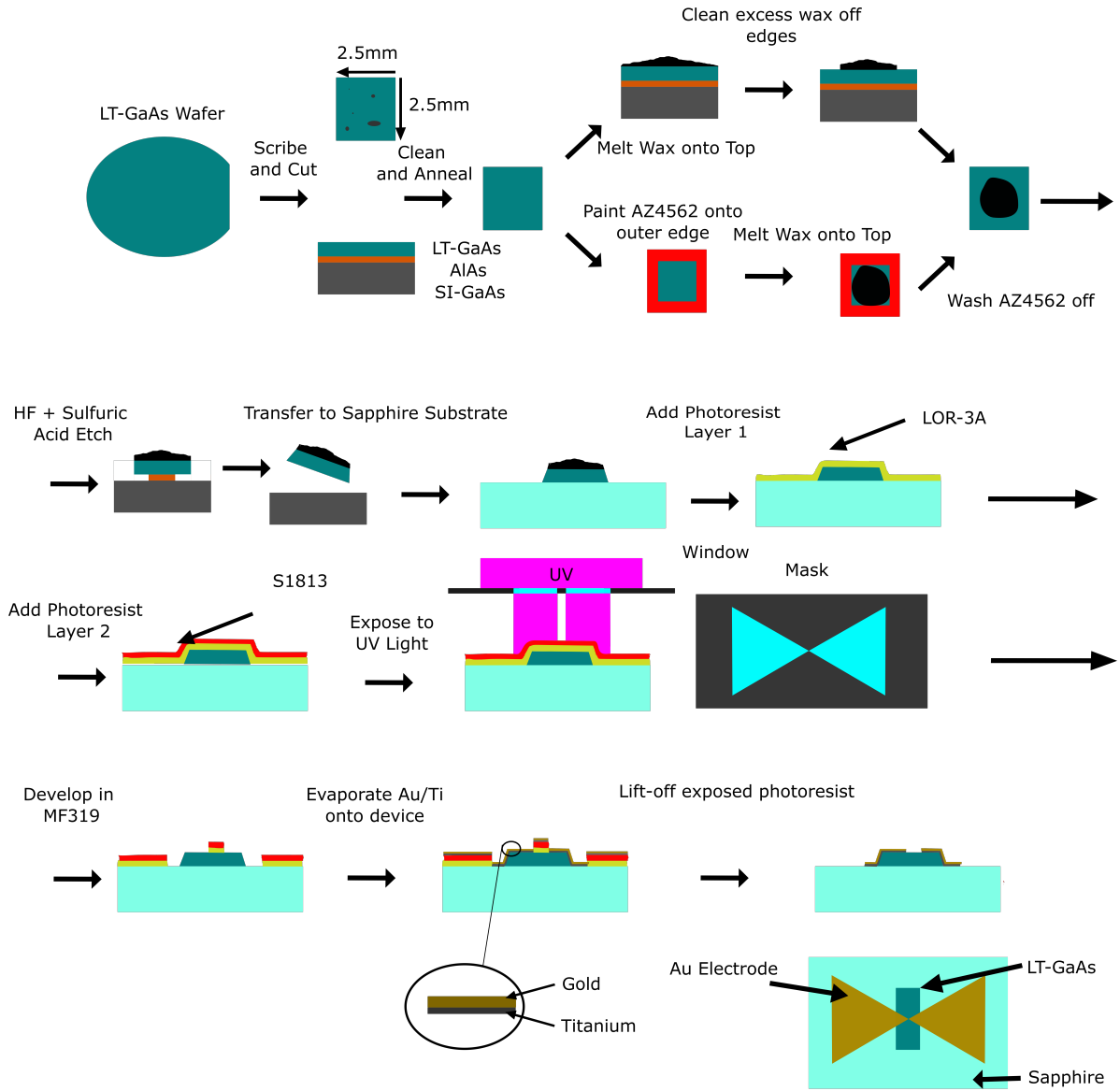
Figure 6.1: A schematic showing the fabrication process for a PC switch with a LT-GaAs substrate. This process is also the same for devices with an SI-GaAs subtrate but without the substrate transfer steps.

of both the LT-GaAs and substrate. It is then baked at $200\,°C$ for $1\,minute$ and the first layer of resist (LOR-3A) is spun on at $2000\,rpm$ for $30\,s$ which corresponds to an approximate thickness of $0.4\,µm$. This is baked once again at $200\,°C$ for $3\,minutes$. Once cooled, a second layer of photoresist (S1813) is spun onto the surface at $4000\,rpm$ for $30\,s$, corresponding to a thickness of $1.4\,µm$, followed by baking at $115\,°C$ for $4\,minutes$. These were placed into a mask-aligner (Karl Suss MJB3) where it underwent contact photolithography and was exposed to ultraviolet (UV) light, centred around $310\,nm$, through an optical mask for $15\,s$. Each sample was then developed in MF319 for $1\,minute$, before being rinsed in water and dried using a dry nitrogen gas. To ensure an undercut in the bottom layer of the photoresist, the sample is baked at $180\,°C$ to crosslink top S1813 layer of photoresist, followed by a further $30\,s$ in MF319. The sample could then be positioned upside-down

in a thermal evaporator. Using a low vacuum environment ($< 1.9 \times 10^{-6}$ mbar), approximately 10 nm of adhesive Ti and 150 nm of Au were evaporated onto the surface of the device. Once completed and cooled, the unexposed photoresist and the excess gold were removed by placing the sample back into a beaker of cyclopentanone for 5 minutes in an ultrasonic bath and dried using dry nitrogen.

As there are many steps and each can suffer from complications, devices fabricated using this method are unlikely to be identical which may explain any variation between nominally identical devices both within the same batch and from different batches.
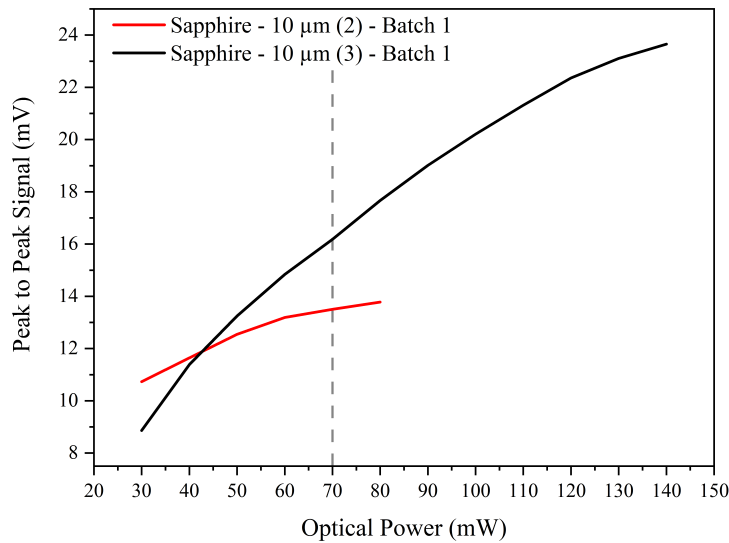
Figure 6.2: The peak to peak signal values for Sapphire Batch 1. There is little agreement between device outputs for the same incident optical power.

6.2.2 Testing of Photoconductive Switches

Using the described method for measuring THz-TDS spectra which is detailed in Chapter 6, each device had a bias of 100 V applied across it and was initially illuminated with 30 mW of incident optical power using an optical attenuator to lower the initial power of the laser. This was then increased in increments of 10 mW until the device was considered to be saturated, close to saturation or destroyed which would manifest as a decrease in the slope of the graph of produced signal versus optical power or a sudden drop in signal output. Ideally, the incident field would have been kept constant for the most ideal comparison but maintaining a constant bias simplified the experimental parameters.

These measurements were performed using a THz-TDS system that will now be referred to as System 2. A mode-locked Ti:sapphire laser (Maitai DeepSee, Spectra-Physics) was used to produce 80 fs pulses centred at 796 nm with a repetition rate of 80 MHz. These were directed at the PC switch being tested and the emissions from this were detected using a 1 mm thick ZnTe crystal and a pair of photodiodes which were balanced to 2.8 V.

The applied bias was modulated using a 7.7 kHz square wave. As no sample was present, only one scan was required for each measurement.

Initially, only devices with a sapphire substrate were fabricated but owing to alignment challenges and for a more complete understanding of the underlying processes, devices with an SI-GaAs substrate were also fabricated from the original wafer and tested. Finally, once the optimum gap size was selected, the chosen PC switches were tested using the fibre laser utilised in the THz-TDS system under construction which will be referred to as System 3. This will be described in Section 6.3.

6.2.3 Results and Discussion

A set of three 10 μm devices on sapphire substrates had been fabricated previously and these were tested first. One of these was destroyed during alignment but the results from the remaining devices are shown in Figure 6.2. This set of devices will be subsequently referred to as Sapphire Batch 1. The dotted line on each graph of peak-to-peak signal versus incident optical power is at 70 mW which is the maximum incident optical power from the fibre laser. The desired device will begin to saturate on or just after this line. As these devices should be identical, so should their output signal when illuminated with the same incident optical fluence but in this case, the outputs of each device vary considerably. Additionally, they reach saturation at different incident optical powers which is also unexpected. This is likely caused by differences in the devices created during fabrication where device 3 in Sapphire Batch 1 was particularly affected although there was no visible damage or problems with lift-off on this device which we have not previously observed when making the larger gap devices with LT-GaAs on sapphire substrates.

A second batch of devices on sapphire substrates was fabricated with the range of gap sizes described above, which will be referred to as Sapphire Batch 2. When attempting to align the 5 μm device, it was destroyed which demonstrates a complication with using these extremely small gap-size devices. The remaining devices were tested as above and the results are shown in Figure 6.3. This batch showed a reverse trend than expected as the 10 μm device produces the lowest signal and the 40 μm produces the highest. The 10 μm device begins to saturate quickly whereas the other devices follow a similar saturation pattern which is also unexpected which again suggests that there is large variation in fabrication and lack of repeatability in the fabrication of nominally identical devices.

It was decided that, for comparison, two devices for each gap size were fabricated using SI-GaAs as a substrate instead of sapphire. Whilst this is opaque to 800 nm light which only allows front-side illumination, this is frequently used as a substrate owing to the fewer steps required to fabricate these devices. These sets of devices of 5–40 μm will be referred to as GaAs Batch 1 and GaAs Batch 2 respectively. This in particular allows

measurements to be performed to determine if the inconsistencies come from problems with the LT-GaAs itself, the liftoff and transfer process or the general photolithographic steps when fabricating these small gap devices. The results for these devices are shown individually in Figure 6.4 and together in Figure 6.5. Nearly all these devices seem to follow expected trends well, with all of the 5 and 10 μm devices producing expected relative values. There is some disagreement between batches for the 20 and 40 μm devices but the 40 μm device shows the expected higher saturation tolerance in both batches. As can be seen clearly in Figure 6.5, whilst the relative values for each batch are sometimes different, the slopes for each gap size are very similar across batches. Owing to the electrical properties of SI-GaAs, the alignment of these devices was significantly easier than for the sapphire devices. This is because the photocurrent across the device is used for initial alignment and SI-GaAs generated significantly more photocurrent for a given applied bias and incident optical power, which is a proxy for the alignment of the beam spot across the devices gap. This is a result of the much higher conductivity of SI-GaAs which results in parasitic photocurrent being generated within the SI-GaAs substrate.

A final batch of emitters were fabricated using a sapphire substrate and tested as described above. These are shown in Figure 6.6 and will be referred to as Sapphire Batch 3. Owing to difficulties during alignment, both the 5 and 10 μm devices were destroyed before data could be obtained. The remaining devices show the expected signal size trends but the 40 μm device begins to saturate before the 20 μm device which does not agree with previous results. This, again, can likely be accounted for with alignment issues and fabrication defects.

The results for all the devices with gap size of 10 μm are shown in Figure 6.7. There seems to be some discrepancy within the Sapphire batches which is likely owing to dif-
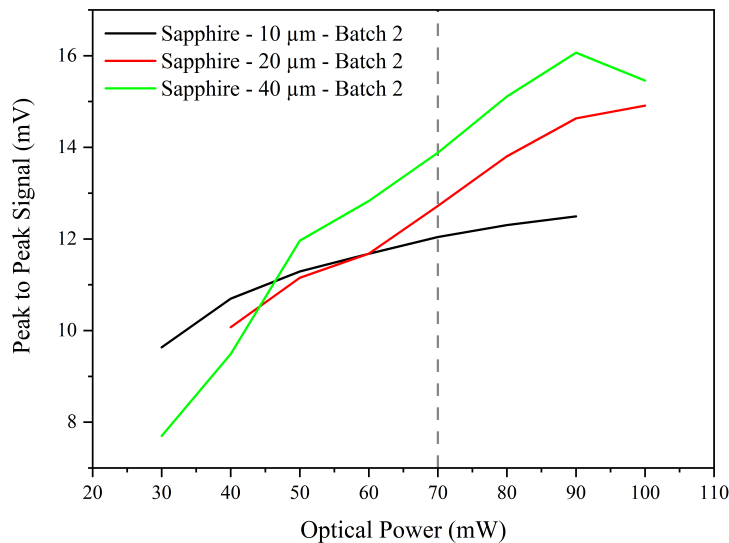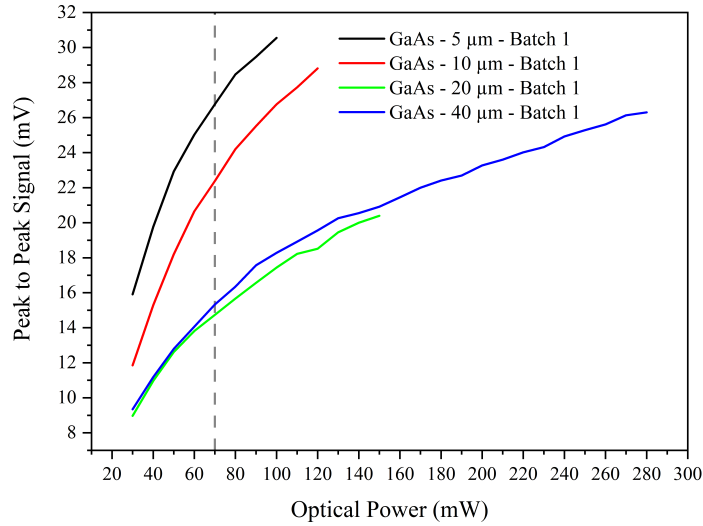

Figure 6.3: The peak to peak signal values for Sapphire Batch 2. The trend is reversed from what is expected as the 40 μm device produces the highest output.

(a) *The peak to peak signal values for GaAs Batch 1.*
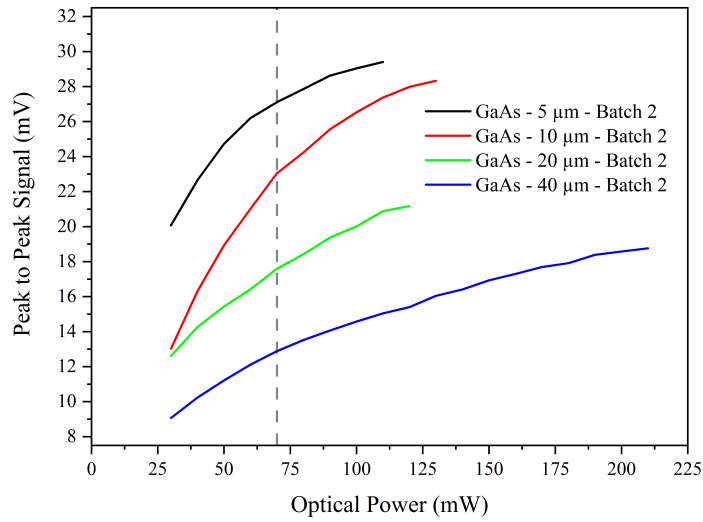
(b) *The peak to peak signal values for GaAs Batch 2.*

Figure 6.4: The peak to peak signal values for both GaAs batches. These generally follow expected trends with the exception of the 20 µm device in GaAs Batch 2 under-performing. The improved output of these devices is likely down to their increased photocurrent which improves alignment.

ficulties in aligning the Sapphire devices and defects introduced during their fabrication and the GaAs devices outperform the sapphire devices. The results of all the devices with gap size of 20 µm are shown in Figure 6.8, where the sapphire devices show quite large disagreement in both output and saturation behavior but the GaAs devices are reasonably consistent. This could also be caused by issues with the Au electrodes whereby they do not bind uniformly across the device owing to discrepancies in the photoresist coverage. Finally the results for all the devices with gap size of 40 µm are shown in Figure 6.9. The saturation behavior for these devices is radically different than expected, with the sapphire devices saturating well before the GaAs devices. A 20 µm device on sapphire at 20 V has a dark current of approximately 0.0018 µA whilst a 20 µm device on GaAs at 20 V has a dark current of approximately 0.0362 µA. This is almost a 200% increase
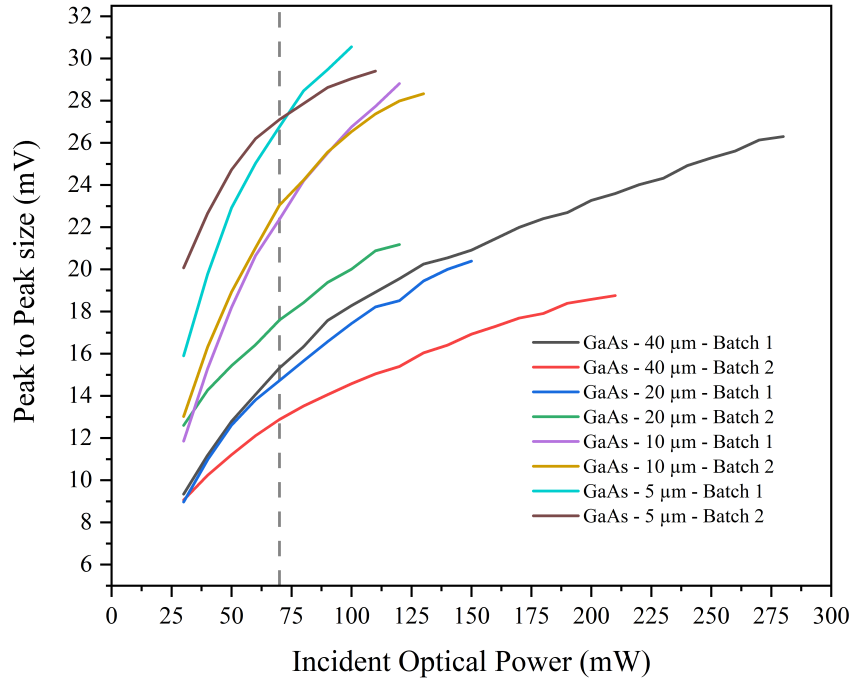
Figure 6.5: The peak to peak signal values for both GaAs batches. It can be seen that the saturation behaviour across batches is consistent.
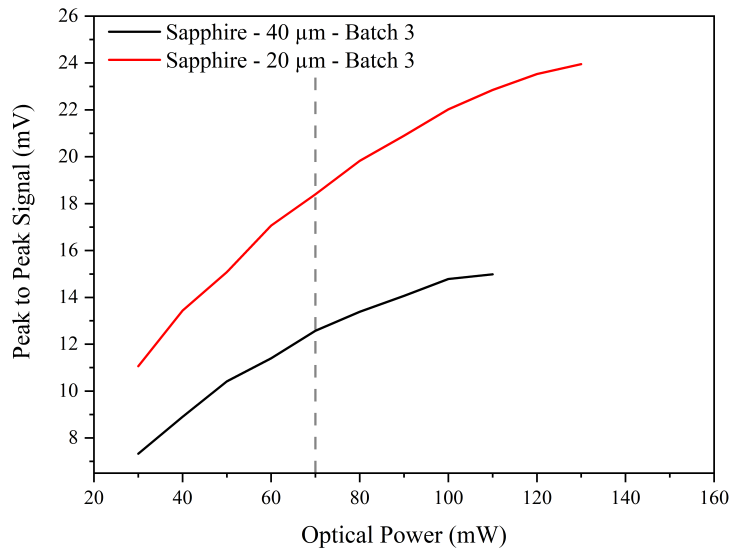
Figure 6.6: The peak to peak signal values for Sapphire Batch 3. Whilst it is expected that the 20 µm would produce a higher output, it was expected to saturate earlier which has not happened.

in the level of dark current between substrates. However, this only makes a significant difference at high applied biases [165]. The out-performance of the GaAs devices when compared to the Sapphire devices can possibly be attributed to low applied fields and incident optical powers involved.

All the results from devices fabricated using a sapphire substrate are shown in Figure 6.10. There is some significant disagreement between batches, particularly when considering the 10 µm devices but this is presumed to be fabrication issues with the sub-
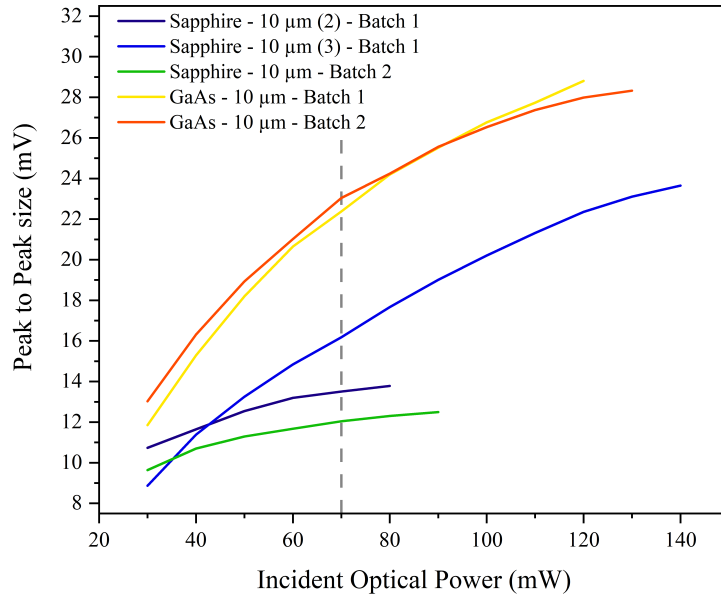
Figure 6.7: The peak to peak signal values for all devices with a gap size of 10 µm. There is disagreement between the sapphire batches but saturation behaviour and output are consistent within batches.
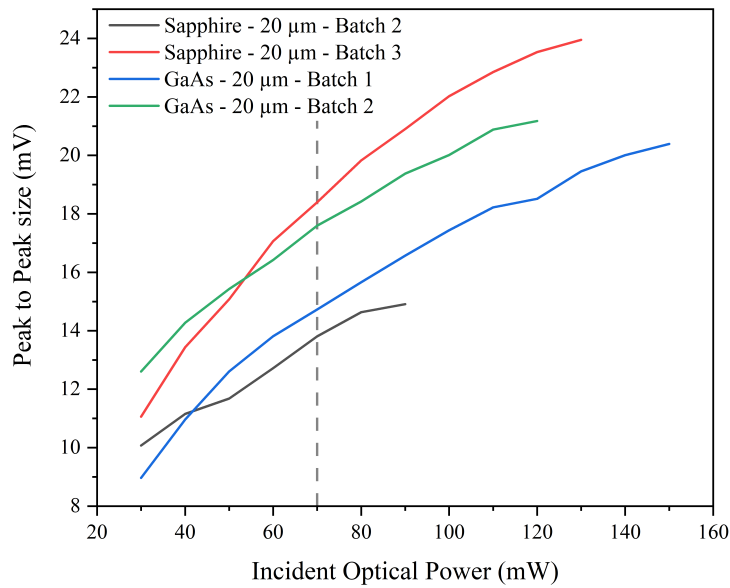
Figure 6.8: The peak to peak signal values for all devices with a gap size of 20 µm. The sapphire devices show significant disagreement.

strate transfer owing to the consistent saturation behaviour within batches. From the trends available it seems that competing factors such as alignment, saturation tolerance and generation efficiency result in the 10 and 40 µm devices producing a similar output for an incident optical power of 70 mW but the device from Batch 2 disagrees with this trend, being one of the best performing devices. Whilst there are inconsistencies, it would seem that 20 µm is the desired gap size for balancing the practicalities of alignment with the maximum power output and desired saturation power.

Figure 6.11 shows pictures of three example 20 µm devices on sapphire substrates.
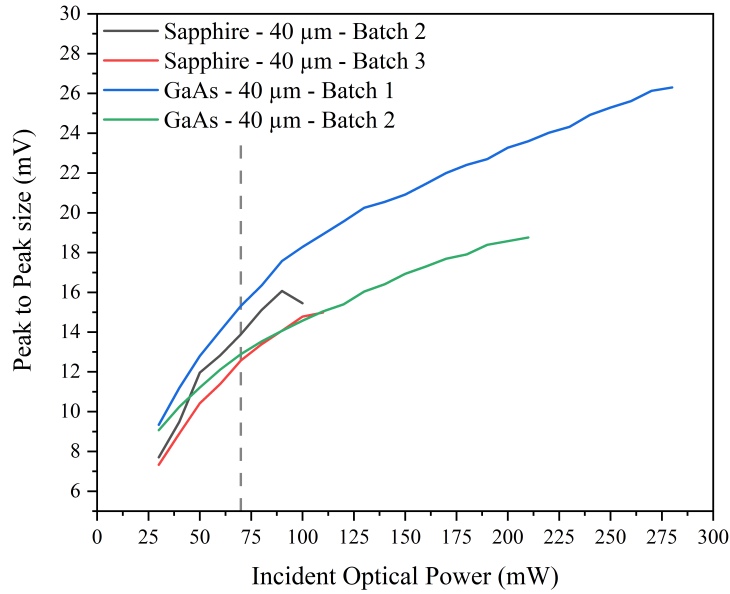
Figure 6.9: The peak to peak signal values for all devices with a gap size of 40 µm. The sapphire devices saturate much earlier than expected when compared to their GaAs counterparts.
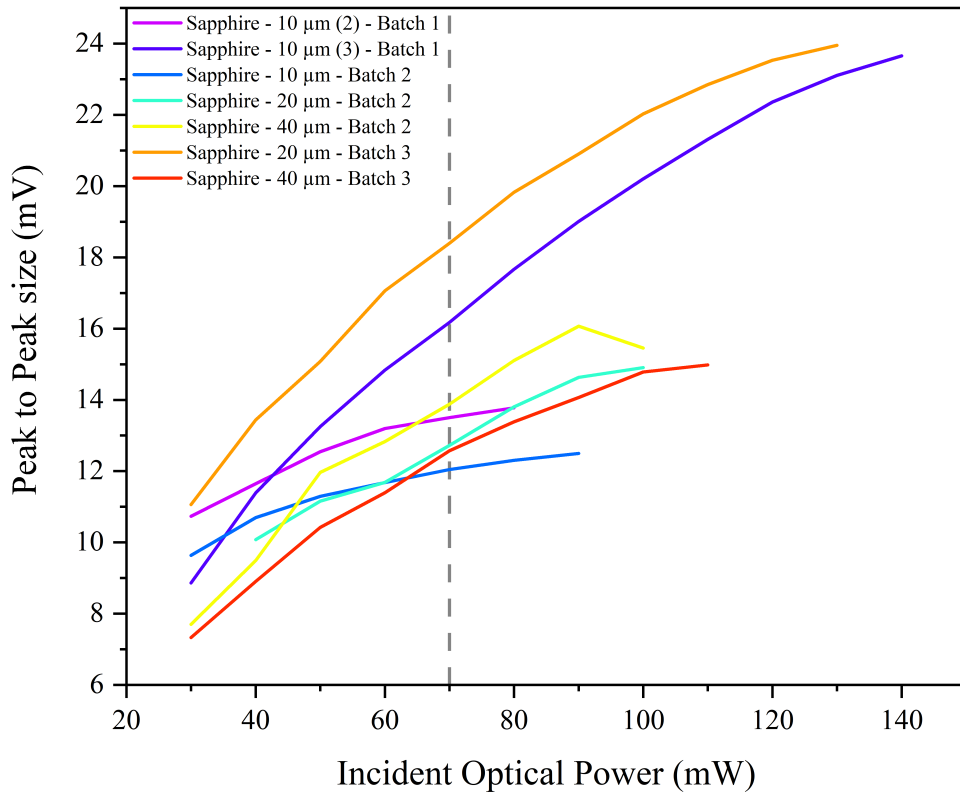
Figure 6.10: The peak to peak signal values for all Sapphire substrate devices. There are some discrepancies between and within batches but the most desirable device is the 20 µm device from Sapphire Batch 2 which has the highest output for the sapphire devices.

The pictures show the same three devices but at two different views for clarity. These devices were fabricated in one batch and so should be nominally identical but it is evident that this is not the case. The degree to which the electrodes stick to the surface varies significantly, most critically across the raised edge where the LT-GaAs begins. This edge

93

is one area that can be vulnerable to damage when a large photocurrent flows through it which is worsened with inconsistencies in electrode thickness and defects along this edge. This can be clearly seen on the middle and right devices and so it is expected that these would saturate before the device on the left. It is likely that this issue was partially responsible for inconsistencies between and within nominally identical batches.
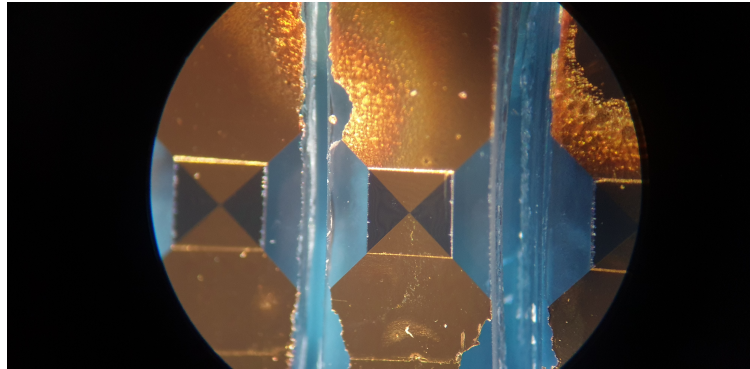
(a) Pic 1
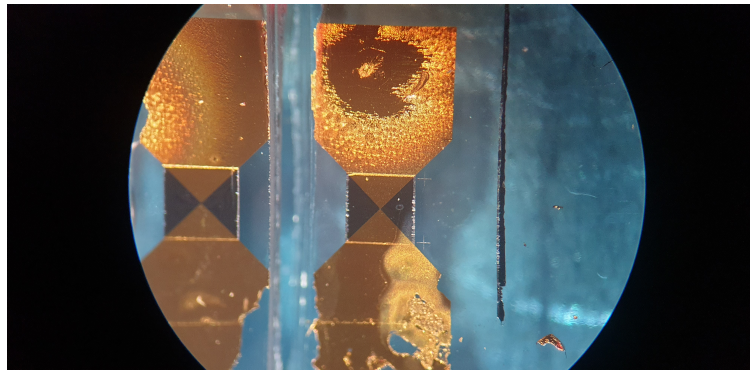
(b) Pic 2

Figure 6.11: Pictures of LT-GaAs on Sapphire substrate devices to demonstrate inconsistency in electrode coating. These devices were fabricated in one batch and so should be nominally identical but it is evident that this is not the case.

6.3 Emitter Testing with Fibre Laser

Once the 20 µm device had been selected as the optimal choice, this was then incorporated into System 3 that uses the Toptica Fibre laser. This system is still under construction and is subject to change, but the initial set-up used a 2 mm ZnTe EO crystal as a detector and applied biases were modulated using a 7 kHz square wave for lock-in detection. A series of tests were performed on the selected device in the emitter position where the optical power hitting the emitter and the EO detector were varied respectively, along with the bias applied to the emitter and the rotation of the EO crystal in its mount. The results of these tests is shown in Figure 6.12

The EO crystal's rotation was performed first and a clear maximum can be seen at

(a) *Optical Sweep - Emitter*

(b) *Optical Sweep - Detector*

(c) *Voltage Sweep - Detector*

(d) *Rotation of EO Crystal*
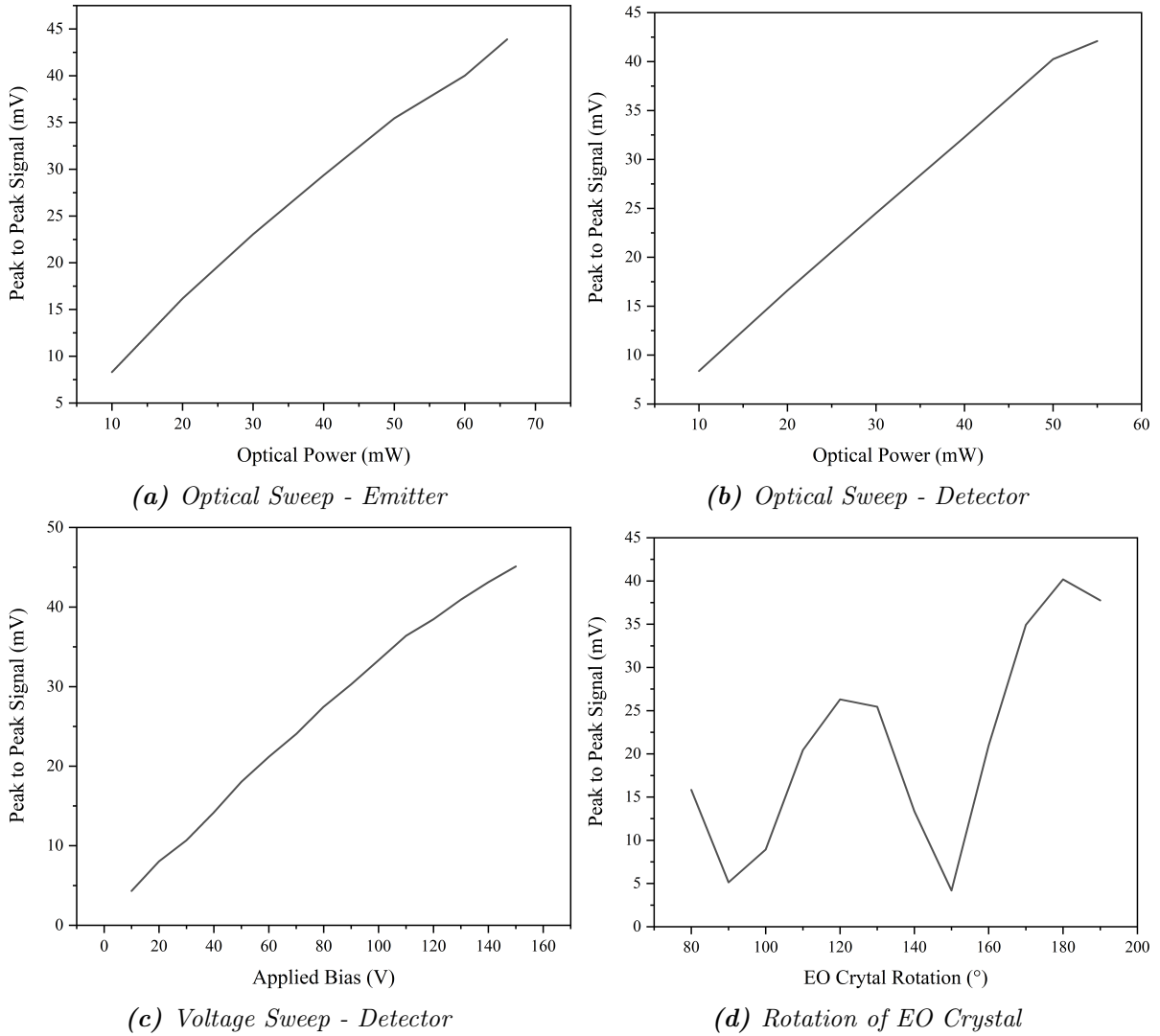
Figure 6.12: Testing of a 20 μm device on a sapphire substrate using the fibre laser in System 3.

180°. This is shown in Figure 6.12d and 180° was used for all remaining scans. The variation of the incident optical power on the emitter is shown in Figure 6.12a and the device appears to be beginning to saturate but more optical power would be required to confirm this. The saturation behavior is easier to see in Figure 6.12b but this is from a different mechanism in the EO crystal. Both these tests were performed using the maximum incident power on the emitter or detector respectively and an applied bias of 150 V. Finally, the applied bias was varied while the maximum incident power was directed to both the emitter and detector. The device begins to saturate at around 140–150 V which is reasonable. Whilst the saturation behaviour of the 20 μm device is not completely ideal, it seems the clear choice for use at the incident optical powers that System 3 will utilise, owing to it being relatively easy to align whilst producing a desirable output.

6.4 Conclusion

This chapter described the investigation into the effect of gap-size on the output of PC switches, specifically at the relatively low optical power ranges that will be utilised by System 3 which is under construction. Devices with both sapphire and GaAs substrates were tested owing to the significantly easier alignment of GaAs devices and to confirm the results of the sapphire devices. Once an optimal gap size had been selected, the device was tested in System 3 to determine its suitability.

The investigation into gap sizes produced some unexpected results whereby some GaAs devices would outperform their sapphire counterparts. This was attributed to issues with the far more complicated fabrication process, specifically the transfer of the LT-GaAs to the sapphire substrate and the application of the Au electrodes. However, System 3 will require an emitter and detector with optically transparent substrates so this slight improvement in performance has not been considered. It was determined that the 5 and 10 μm devices were too difficult to align and were not chosen. As the 20 μm device performed better than the 40 μm device, this was selected as the optimal size.

A 20 μm device was put into System 3 as an emitter and a ZnTe crystal was used as preliminary detector. The device performed satisfactorily when both the incident optical power and the applied bias was varied and the optimal parameters for the ZnTe crystal were selected. This project was significantly hampered by the pandemic whereby the multiple, lengthy closures and subsequent occupancy rules of the laboratory prevented any meaningful progress for a significant portion of the time available. Additionally, the fibre laser in System 3 required repairing and was unavailable for a number of months.

Chapter 7

Conclusions and Further Work

To conclude, this thesis began in Chapter 1 with a description of THz radiation and a brief literature review of its applications. The structure of the thesis was then outlined. In Chapter 2, various methods of generating and detecting THz radiation were described with a particular focus on PC switches and EO crystals, as these are the sources and detectors used throughout this work. The theory of THz-TDS, along with the primary experimental setup, was presented which was followed by the data extraction process and some of the challenges involved with this. DFT was introduced in Chapter 3 and the procedure for calculating a THz absorption spectrum from a crystal structure was described.

The focus of Chapter 4 was the investigation into the effect of different DiCs on the calculation of the THz absorption spectrum of αLM. This involved performing an optimisation of the structure of αLM and calculating the dynamical matrix of the structure using the D2, D3, D3BJ and TS corrections, then determining which spectrum best matched the experimental spectrum. The correlation between calculated and experimental spectra was used to determine which correction was most suitable for further work on materials similar to αLM and other complex organic molecular crystals. This was found to be the D3 correction although the TS correction also performed reasonably well. This was aided through optimisation of the parameters used in PDielec to construct the spectra. Differences between the final structures as a consequence of the DiCs were also analysed using several methods to potentially determine what may have caused the differences between calculated spectra. Analysis of the modes provided evidence that the dispersion only marginally changes the composition of the phonon modes which is likely the explanation for the relatively small differences in mode frequency.

In Chapter 5, the concept of anharmonicity and its role in vibrational spectroscopy was introduced. The challenges behind incorporating anharmonicity for complex systems such as αLM were outlined and the QHA was presented as crude solution to this problem. This

was used to calculate the thermodynamic properties and temperature-dependent phonon frequencies of αLM, which could then be utilised to calculate the THz absorption spectra at 300 K. The temperature dependence of several modes were examined and compared to experimental values along with the calculation of the mode Grüneisen parameter. Finally, a brief investigation into the mode potential energy surfaces for two modes was conducted with the aim of explaining discrepancies between the experimental and calculated spectra. In summary, this project produced both successes and failures. The heat capacity of the system was drastically overestimated, with an increase of 78.9% but this is not completely unexpected for a system as large and complex as αLM when using the QHA, in particular as it has been previously shown that it can be difficult to calculate the thermal properties of hydrate crystals. The temperature dependence of one mode was also incorrectly identified. However, the calculated unit cell volume at 300 K being less than 1% of the experimental value and the calculation of the THz absorption spectrum at 300 K can be considered successes owing to high degree of correlation with the experimental spectrum taken at 300 K, which was the first time this has been achieved in this group.

Finally, in Chapter 6, a project to build a new THz TD spectrometer was outlined. Whilst the main goals of this project were severely hampered by both hardware failures and lengthy lab closures owing to the COVID pandemic, an investigation into the effect of gap-size on the output of PC switches, specifically at the relatively low optical power ranges that are provided by a fibre laser, was undertaken. Devices constructed of LT-GaAs with both sapphire and GaAs substrates were tested, owing to the significantly easier alignment of GaAs devices and to confirm the trends shown by the sapphire devices. Once an optimal gap size had been selected, the device was tested in System 3 to determine its suitability. The investigation into gap sizes produced some unexpected results whereby some GaAs devices would outperform their sapphire counterparts. This was attributed to issues with the far more complicated fabrication process, specifically the transfer of the LT-GaAs to the sapphire substrate and the application of the Au electrodes when producing devices with gap-sizes in this range. However, System 3 will require an emitter and detector with optically transparent substrates so this slight improvement in performance has not been considered. It was determined that the 20 μm devices performed better than the 40 μm devices and proved much less challenging to align than the 10 μm devices, and so this was selected as the optimal size. A 20 μm device was put into System 3 as an emitter and a ZnTe crystal was used as preliminary detector. The device performed satisfactorily when both the incident optical power and the applied bias was varied and the optimal parameters for the ZnTe crystal were selected. These parameters can now be used to complete System 3.

7.1 Further Work

7.1.1 Chapter 4

In Chapter 4, the starting structure, which was obtained at $150\,\mathrm{K}$, was the lowest temperature structure that was available. It would be more advantageous to have a structure taken at an even lower temperature, ideally at $4\,\mathrm{K}$ which is the standard temperature that we tend to measure experimental spectra to obtain the best definition between peaks in these complex spectra. Owing to lab shutdowns because of the COVID pandemic, attempts to grow a single crystal of αLM and perform low temperature XRD were unable to be completed. Obtaining low temperature structures should reduce the required computational resources to optimise these structures into the ground electronic state and may allow for larger molecules to be studied and for spectral comparability with experiment to increase. Additionally, the THz absorption spectra of single crystals would allow for different propagation directions of the THz pulse through the crystal lattice, allowing study of polarisation specific modes. As there can be a significant degree of overlap between spectral modes, this may help to enhance spectral identification and analysis by 'turning off' some modes so others may be more visible.

As computational resources improve, some of the more expensive DiCs discussed in Chapter 4 may become viable for use in the calculation of THz absorption spectra of complex organic molecular crystals. These may prove to produce more experimentally comparable spectra although inevitably they will always be more computationally expensive. However, in applications where this is not a limiting factor, this may enable the study of even larger and more complex systems.

7.1.2 Chapter 5

By demonstrating the ability to calculate the THz absorption spectrum of αLM at $300\,\mathrm{K}$ in Chapter 5, this could allow for simpler experimental setups that do not have to incorporate space for cryogenic apparatus and reduces the cost and risk of the measurement. However, at present this will be limited to molecular structures where the number and environment of electrons is similar to αLM but this will change as computational resources improve.

It would have been desirable to measure the experimental unit cell volume at as low a temperature as possible and at as many temperature points as possible up to $300\,\mathrm{K}$. This would have allowed a better comparison between the calculated volume-temperature curve to experimental values than was achieved. The growth of single crystals of αLM would have facilitated this but this was not possible.

Five unit cells of different volumes were chosen in Chapter 5 as this was the minimum

number that was able to be used, owing the significant computational resources required to optimise and calculate the dynamical matrix for this number of structures. As resources improve, it is expected that the use of more structures will improve the accuracy of the parameters extracted using the QHA.

7.1.3   Chapter 6

System 3, described in Chapter 6, now can be built with PC devices with an appropriate gap-size for the available laser power. As these devices are produced on sapphire substrates, which is transparent to IR radiation at 800 nm, illumination of the LT-GaAs can now occur through the substrate. This should allow less dispersion and losses of the resulting THz beam, improving SNR. Once completed, the system has been designed to incorporate an ATR attachment which should remove the need for a diluting medium, such as PTFE, when measuring THz absorption spectra. Finally, as these attachments used frequently in FTIR, this should allow the full infrared spectrum to be measured on the same system.

Bibliography

[1] R. A. Lewis, "A Review of Terahertz Sources," *Journal of Physics D: Applied Physics*, vol. 47, p. 374 001, 37 2014.

[2] R. Appleby and H. B. Wallace, "Standoff detection of weapons and contraband in the 100 GHz to 1 THz region," *IEEE Transactions on Antennas and Propagation*, vol. 55, pp. 2944–2956, 11 2007.

[3] J. F. Federici, B. Schulkin, F. Huang, D. Gary, R. Barat, F. Oliveira, and D. Zimdars, "THz imaging and sensing for security applications—explosives, weapons and drugs," *Semiconductor Science and Technology*, vol. 20, S266–S280, 7 2005.

[4] L. Wu, D. Xu, Y. Wang, B. Liao, Z. Jiang, L. Zhao, Z. Sun, N. Wu, T. Chen, H. Feng, and J. Yao, "Study of in vivo brain glioma in a mouse model using continuous-wave terahertz reflection imaging," *Biomedical Optics Express*, vol. 10, p. 3953, 8 2019.

[5] G. G. Hernandez-Cardoso, L. F. Amador-Medina, G. Gutierrez-Torres, E. S. Reyes-Reyes, C. A. B. Martínez, C. C. Espinoza, J. A. Cruz, I. Salas-Gutierrez, B. O. Murillo-Ortíz, and E. Castro-Camus, "Terahertz imaging demonstrates its diagnostic potential and reveals a relationship between cutaneous dehydration and neuropathy for diabetic foot syndrome patients," *Scientific Reports*, vol. 12, pp. 1–10, 1 2022.

[6] A. Chen, A. Virk, Z. Harris, A. Abazari, R. Honkanen, and M. H. Arbab, "Non-contact terahertz spectroscopic measurement of the intraocular pressure through corneal hydration mapping," *Biomedical Optics Express, Vol. 12, Issue 6, pp. 3438-3449*, vol. 12, pp. 3438–3449, 6 2021.

[7] O. B. Osman, T. J. Tan, S. Henry, A. Warsen, N. Farr, A. M. McClintic, Y.-N. Wang, S. Arbabi, M. H. Arbab, and M. H. Arbab, "Differentiation of burn wounds in an in vivo porcine model using terahertz spectroscopy," *Biomedical Optics Express*, vol. 11, pp. 6528–6535, 11 2020.

[8] D. Ruan, E. Brown, Z. Taylor, W. Grundfest, D. B. Ennis, J. Garritano, N. Bajwa, M. C. Fishbein, S. Sung, H. Huang, D. Wang, E. Dutson, and P. Tewari, "Methods

for registering and calibrating in vivo terahertz images of cutaneous burn wounds," *Biomedical Optics Express*, vol. 10, pp. 322–337, 1 2019.

[9] D. B. Bennett, Z. D. Taylor, P. Tewari, R. S. Singh, M. O. Culjat, W. S. Grundfest, D. J. Sassoon, R. D. Johnson, J.-P. Hubschman, and E. R. Brown, "Terahertz sensing in corneal tissues," *Journal of Biomedical Optics*, vol. 16, p. 057 003, 5 2011.

[10] C. Yu, S. Fan, Y. Sun, and E. Pickwell-MacPherson, "The potential of terahertz imaging for cancer diagnosis: A review of investigations to date," *Quantitative Imaging in Medicine and Surgery*, vol. 2, pp. 335–345, 1 2012.

[11] L. Ho, R. Müller, K. C. Gordon, P. Kleinebudde, M. Pepper, T. Rades, Y. Shen, P. F. Taday, and J. A. Zeitler, "Applications of terahertz pulsed imaging to sustained-release tablet film coating quality assessment and dissolution performance," *Journal of Controlled Release*, vol. 127, pp. 79–87, 1 2008.

[12] M. D. Mowery, R. Sing, J. Kirsch, A. Razaghi, S. Béchard, and R. A. Reed, "Rapid at-line analysis of coating thickness and uniformity on tablets using laser induced breakdown spectroscopy," *Journal of Pharmaceutical and Biomedical Analysis*, vol. 28, pp. 935–943, 5 2002.

[13] K. Korasa and F. Vrečer, "Overview of PAT process analysers applicable in monitoring of film coating unit operations for manufacturing of solid oral dosage forms," *European journal of pharmaceutical sciences : official journal of the European Federation for Pharmaceutical Sciences*, vol. 111, pp. 278–292, 2018.

[14] H. Lin, Y. Dong, D. Markl, B. M. Williams, Y. Zheng, Y. Shen, and J. A. Zeitler, "Measurement of the intertablet coating uniformity of a pharmaceutical pan coating process with combined terahertz and optical coherence tomography in-line sensing," *Journal of Pharmaceutical Sciences*, vol. 106, pp. 1075–1084, 4 2017.

[15] A. D. Burnett and J. Kendrick, "Calculating the complex permittivity of powdered crystalline material at infrared and terahertz frequencies," 2016, pp. 1–2.

[16] P. Wang, J. Zhao, Y. Zhang, Z. Zhu, L. Liu, H. Zhao, X. Yang, X. Yang, X. Sun, and M. He, "The fingerprints of nifedipine/isonicotinamide cocrystal polymorph studied by terahertz time-domain spectroscopy," *International Journal of Pharmaceutics*, vol. 620, p. 121 759, 2022.

[17] J. A. Zeitler, *Pharmaceutical Terahertz Spectroscopy and Imaging*, A. Müllertz, Y. Perrie, and T. Rades, Eds. Springer New York, 2016, pp. 171–222.

[18] Z. Song, X. Liu, A. Ochani, S. Shen, Q. Li, Y. Sun, and M. T. Ruggiero, "Low-frequency vibrational spectroscopy: A new tool for revealing crystalline magnetic structures in iron phosphate crystals," *Physical Chemistry Chemical Physics*, vol. 23, pp. 22 241–22 245, 39 2021.

[19] K. Druzbicki, J. Mielcarek, A. Kiwilsza, L. Toupet, E. Collet, A. Pajzderska, and J. Wasicki, "Computationally Assisted (Solid-State Density Functional Theory) Structural (X-ray) and Vibrational Spectroscopy (FT-IR, FT-RS, TDs-THz) Characterization of the Cardiovascular Drug Lacidipine," *Crystal Growth and Design*, vol. 15, pp. 2817–2830, 6 2015.

[20] J. Zeitler, P. F. Taday, M. Pepper, and T. Rades, "Relaxation and crystallization of amorphous carbamazepine studied by terahertz pulsed spectroscopy," *Journal of Pharmaceutical Sciences*, vol. 96, pp. 2703–2709, 10 2007.

[21] M. Walther, B. M. Fischer, and P. U. Jepsen, "Noncovalent intermolecular forces in polycrystalline and amorphous saccharides in the far infrared," *Chemical Physics*, vol. 288, pp. 261–268, 2-3 2003.

[22] T. A. Shmool, P. J. Woodhams, M. Leutzsch, A. D. Stephens, M. U. Gaimann, M. D. Mantle, G. S. K. Schierle, C. F. van der Walle, and J. A. Zeitler, "Observation of high-temperature macromolecular confinement in lyophilised protein formulations using terahertz spectroscopy," *International Journal of Pharmaceutics: X*, vol. 1, p. 100 022, 2019.

[23] A. G. Davies, A. D. Burnett, W. Fan, E. H. Linfield, and J. E. Cunningham, "Terahertz spectroscopy of explosives and drugs," *Materials Today*, vol. 11, pp. 18–26, 3 2008.

[24] M. C. Bellissent-Funel, A Hassanali, M Havenith, R. Henchman, P Pohl, F Sterpone, D van der Spoel, Y Xu, and A. Garcia, "Water determines the structure and dynamics of proteins," *Chemical Reviews*, vol. 116, pp. 7673–7697, 13 2016.

[25] N. Laman, S. S. Harsha, D. Grischkowsky, and J. S. Melinger, "High-resolution waveguide thz spectroscopy of biological molecules," *Biophysical Journal*, vol. 94, pp. 1010–1020, 3 2008.

[26] B. Gompf, A. Matei, N. Drischko, M. Dressel, F. Bös, and J. Pleiss, "Protein dynamics in the THz-range," *Conference Digest of the 2004 Joint 29th International Conference on Infrared and Millimeter Waves and 12th International Conference on Terahertz Electronics*, pp. 739–740, 2004.

[27] A. D. Stephens, J. Kölbel, R. Moons, C. W. Chung, M. T. Ruggiero, N. Mahmoudi, T. A. Shmool, T. M. McCoy, D. Nietlispach, A. F. Routh, F. Sobott, J. A. Zeitler, G. Schierle, G. S. K. Schierle, A. D. Stephens, M. J. Kölbel, M. C. W. Chung, M. T. Ruggiero, T. A. Shmool, T. M. McCoy, A. F. Routh, J. A. Zeitler, G. S. K. Schierle, R Moons, F Sobott, and R. U. A. L. D. Nietlispach, "Decreased Water Mobility Contributes To Increased α-Synuclein Aggregation," *Angewandte Chemie International Edition*, 2022.

[28] D. M. Slocum, E. J. Slingerland, R. H. Giles, and T. M. Goyette, "Atmospheric absorption of terahertz radiation and water vapor continuum effects," *Journal of Quantitative Spectroscopy and Radiative Transfer*, vol. 127, pp. 49–63, 2013.

[29] Y. Zhao, Z. Li, J. Liu, C. Hu, H. Zhang, B. Qin, and Y. Wu, "Intermolecular vibrational modes and h-bond interactions in crystalline urea investigated by terahertz spectroscopy and theoretical calculation," *Spectrochimica Acta Part A: Molecular and Biomolecular Spectroscopy*, vol. 189, pp. 528–534, 2018.

[30] M. T. Ruggiero and J. A. Zeitler, "Resolving the origins of crystalline anharmonicity using terahertz time-domain spectroscopy and ab initio simulations," *J. Phys. Chem. B*, vol. 120, p. 53, 2016.

[31] H. Fujisaki and J. E. Straub, "Vibrational energy relaxation in proteins," *Proceedings of the National Academy of Sciences of the United States of America*, vol. 102, pp. 6726–6731, 19 2005.

[32] H. Y. Hwang, S. Fleischer, N. C. Brandt, B. G. P. Jr., M. Liu, K. Fan, A. Sternbach, X. Zhang, R. D. Averitt, and K. A. Nelson, "A review of non-linear terahertz spectroscopy with ultrashort tabletop-laser pulses," *Journal of Modern Optics*, vol. 62, pp. 1447–1479, 18 2015.

[33] S. Ganichev and W. Prettl, *Intense Terahertz Excitation of Semiconductors*. Oxford University Press, 2005.

[34] M. C. Hoffmann, N. C. Brandt, H. Y. Hwang, K.-L. Yeh, and K. A. Nelson, "Terahertz kerr effect," *Applied Physics Letters*, vol. 95, p. 231105, 23 2009.

[35] S. Fleischer, Y. Khodorkovsky, E. Gershnabel, Y. Prior, and I. S. Averbukh, "Molecular alignment induced by ultrashort laser pulses and its impact on molecular motion," *Israel Journal of Chemistry*, vol. 52, pp. 414–437, 5 2012.

[36] S. J. Dampf and T. M. Korter, "Crystalline molecular standards for low-frequency vibrational spectroscopies," *Journal of Infrared, Millimeter, and Terahertz Waves*, pp. 1–17, 2020.

[37] G. J. Stacey, "THz Low Resolution Spectroscopy for Astronomy," *IEEE Transactions on Terahertz Science and Technology*, vol. 1, pp. 241–255, 2011.

[38] N. Orihashi, S. Suzuki, and M. Asada, "One thz harmonic oscillation of resonant tunneling diodes," *Applied Physics Letters*, vol. 87, p. 233501, 23 2005.

[39] A. G. Davies, E. H. Linfield, and M. B. Johnston, "The development of terahertz sources and their applications," *Physics in medicine and biology*, vol. 47, pp. 3679–3689, 21 2002.

[40] S. H. Gold and G. S. Nusinovich, "Review of high-power microwave source research," *Review of Scientific Instruments*, vol. 68, p. 3945, 11 1998.

[41] W. He, C. R. Donaldson, L. Zhang, K. Ronald, P. McElhinney, and A. W. Cross, "High power wideband gyrotron backward wave oscillator operating towards the terahertz region," *Physical Review Letters*, vol. 110, p. 165 101, 16 2013.

[42] L. P. Schmidt, S. Biber, G. Rehm, and K. Huber, "THz measurement technologies and applications," *14th International Conference on Microwaves, Radar and Wireless Communications, MIKON 2002*, vol. 2, pp. 581–587, 2002.

[43] G. P. Williams, "FAR-IR/THz radiation from the Jefferson Laboratory, energy recovered linac, free electron laser," *Review of Scientific Instruments*, vol. 73, p. 1461, 3 2002.

[44] K. A. McIntosh, E. R. Brown, K. B. Nichols, O. B. McMahon, W. F. DiNatale, and T. M. Lyszczarz, "Terahertz photomixing with diode lasers in low-temperature-grown gaas," *Applied Physics Letters*, vol. 67, pp. 3844–3846, 26 1995.

[45] J. Dai, J. Liu, and X.-C. Zhang, "Terahertz wave air photonics: Terahertz wave generation and detection with laser-induced gas plasma," *IEEE Journal of Selected Topics in Quantum Electronics*, vol. 17, pp. 183–190, 1 2011.

[46] A. C. Warren, N. Katzenellenbogen, D. Grischkowsky, J. M. Woodall, M. R. Melloch, and N. Otsuka, "Subpicosecond, freely propagating electromagnetic pulse generation and detection using gaas:as epilayers," *Applied Physics Letters*, vol. 58, pp. 1512–1514, 14 1991.

[47] Q. Wu and X. Zhang, "Free-space electro-optic sampling of terahertz beams," *Applied Physics Letters*, vol. 67, pp. 3523–3525, 24 1995.

[48] B. S. Williams, "Terahertz quantum-cascade lasers," *Nature Photonics*, vol. 1, p. 517, 2007.

[49] J. Faist, F. Capasso, D. L. Sivco, C. Sirtori, A. L. Hutchinson, and A. Y. Cho, "Quantum cascade laser," *Science*, vol. 264, pp. 553–556, 5158 1994.

[50] Q. Lu, D. Wu, S. Sengupta, S. Slivken, and M. Razeghi, "Room temperature continuous wave, monolithic tunable thz sources based on highly efficient mid-infrared quantum cascade lasers," *Scientific Reports*, vol. 6, p. 23 595, 2016.

[51] X. Wang, C. Shen, T. Jiang, Z. Zhan, Q. Deng, W. Li, W. Wu, N. Yang, W. Chu, and S. Duan, "High-power terahertz quantum cascade lasers with 0.23 w in continuous wave mode," *AIP Advances*, vol. 6, p. 075 210, 7 2016.

[52] A. Khalatpour, A. K. Paulsen, C. Deimert, Z. R. Wasilewski, and Q. Hu, "High-power portable terahertz laser systems," *Nature Photonics 2020 15:1*, vol. 15, pp. 16–20, 1 2020.

[53] A. Khalatpour, M. C. Tam, S. J. Addamane, J. Reno, Z. Wasilewski, and Q. Hu, "Terahertz semiconductor laser source at -12 C," 2022.

[54] K. Biermann, M. Wienold, R. Sharma, H. T. Grahn, L. Schrottke, B. Röben, and A. Tahraoui, "High-temperature, continuous-wave operation of terahertz quantum-cascade lasers with metal-metal waveguides and third-order distributed feedback," *Optics Express*, vol. 22, pp. 3334–3348, 3 2014.

[55] M. A. Kainz, M. P. Semtsiv, G. Tsianos, S. Kurlov, W. T. Masselink, S. Schönhuber, H. Detz, W. Schrenk, K. Unterrainer, G. Strasser, and A. M. Andrews, "Thermoelectric-cooled terahertz quantum cascade lasers," 2019.

[56] J. Keeley, J. Freeman, K. Bertling, Y. L. Lim, R. A. Mohandas, T. Taimre, L. H. Li, D. Indjin, A. D. Rakić, E. H. Linfield, A. G. Davies, and P. Dean, "Measurement of the emission spectrum of a semiconductor laser using laser-feedback interferometry," *Scientific Reports*, vol. 7, pp. 1–9, 1 2017.

[57] E. H. Linfield, T. Rawlings, L. H. Li, J. Partington, R. Chhantyal-Pun, J. Keeley, A. Valavanis, N. Brewster, B. N. Ellison, M. Oldfield, R. Dong, P. Dean, A. G. Davies, O. Auriacombe, Y. J. Han, and M. Henry, "Gas spectroscopy through multimode self-mixing in a double-metal terahertz quantum cascade laser," *Optics Letters, Vol. 43, Issue 24, pp. 5933-5936*, vol. 43, pp. 5933–5936, 24 2018.

[58] M. C. Wanke, E. W. Young, C. D. Nordquist, M. J. Cich, A. D. Grine, C. T. Fuller, J. L. Reno, and M. Lee, "Monolithically integrated solid-state terahertz transceivers," *Nature Photonics 2010 4:8*, vol. 4, pp. 565–569, 8 2010.

[59] B. Swinyard, O. Auriacombe, T. Bradshaw, D. Brooks, J. Charlton, M. Crook, G. Davies, B. Ellison, M. Emes, J. Friend, D. Gerber, C. Gray, M. Henry, T. Hunt, E. Linfield, N. Navarathinam, S. Parks, T. Rawlings, S. Rea, C. Saunders, G. Savini, S. M. Tun, D. Walker, H. Wang, and B. Winter, "The low cost upper atmosphere sounder: The "elegant breadboard" programme," *2015 8th UK, Europe, China Millimeter Waves and THz Technology Workshop, UCMMT 2015*, 2016.

[60] P. Dean, A. Valavanis, J. Keeley, K. Bertling, Y. L. Lim, R. Alhathlool, A. D. Burnett, L. H. Li, S. P. Khanna, D. Indjin, T. Taimre, A. D. Rakić, E. H. Linfield, and A. G. Davies, "Terahertz imaging using quantum cascade lasers - a review of systems and applications," *Journal of Physics D: Applied Physics*, vol. 47, 37 2014.

[61] Z. Chen, Z. Y. Tan, Y. J. Han, R. Zhang, X. G. Guo, H. Li, J. C. Cao, and H. C. Liu, "Wireless communication demonstration at 4.1thz using quantum cascade laser and quantum well photodetector," *Electronics Letters*, vol. 47, pp. 1002–1004, 17 2011.

[62] A. Wade, G. Fedorov, D. Smirnov, S. Kumar, B. S. Williams, Q. Hu, and J. L. Reno, "Magnetic-field-assisted terahertz quantum cascade laser operating up to 225 k," *Nature Photonics*, vol. 3, pp. 41–45, 1 2008.

[63] N. V. Kinev and V. P. Koshelets, "Study and comparison of laboratory terahertz sources based on a backward wave oscillator, a semiconductor microwave frequency multiplier with large numbers of harmonics, and a long josephson junction," *Journal of Communications Technology and Electronics*, vol. 66, pp. 278–288, 3 2021.

[64] F Rettich, N. Vieweg, O. Cojocari, and. A. Deninger, "Field intensity detection of individual terahertz pulses at 80 mHz repetition rate,"

[65] R. Al-Mudhafar and H. A. Jawad, "Plasmonic hybrid terahertz photomixer of graphene nanoantenna and nanowires," *International Journal of Electrical and Computer Engineering (IJECE*, vol. 12, pp. 2711–2720, 3 2022.

[66] H. Hamster, A. Sullivan, S. Gordon, W. White, and R. W. Falcone, "Subpicosecond, electromagnetic pulses from intense laser-plasma interaction," *Physical Review Letters*, vol. 71, pp. 2725–2728, 17 1993.

[67] D. H. Auston, K. P. Cheung, and P. R. Smith, "Picosecond photoconducting hertzian dipoles," *Applied Physics Letters*, vol. 45, pp. 284–286, 3 1984.

[68] C. P. Vaisakh, M. K. Bhowal, S Dhar, al, K Rabia, F Meng, and M. D. Thomson, "THz emitters based on the photo-Dember effect," *Journal of Physics D: Applied Physics*, vol. 47, p. 374 002, 37 2014.

[69] N. M. Burford, M. O. El-Shenawee, and M. O. El, "Review of terahertz photoconductive antenna technology," *https://doi.org/10.1117/1.OE.56.1.010901*, vol. 56, p. 010 901, 1 2017.

[70] M. Tani, S. Matsuura, K. Sakai, and S. ichi Nakashima, "Emission characteristics of photoconductive antennas based on low-temperature-grown gaas and semi-insulating gaas," *Applied Optics*, vol. 36, p. 7853, 30 1997.

[71] S. Winnerl, F. Peter, S. Nitsche, A. Dreyhaupt, B. Zimmermann, M. Wagner, H. Schneider, M. Helm, and K. Kohler, "Generation and detection of thz radiation with scalable antennas based on gaas substrates with different carrier lifetimes," *IEEE Journal of Selected Topics in Quantum Electronics*, vol. 14, pp. 449–457, 2 2008.

[72] D. S. Kim and D. S. Citrin, "Dynamics of electric field screening in photoconductive thz sources with spatially patterned excitation," IEEE, 2005, pp. 417 –420.

[73] D. R. Bacon, J. Madéo, and K. M. Dani, "Photoconductive emitters for pulsed terahertz generation," *Journal of Optics*, vol. 23, p. 064 001, 6 2021.

[74] K. Murakumo, Y. Yamaoka, N. Kumagai, T. Kitada, and T. Isu, "Photoconductivity of Er-doped InAs quantum dots embedded in strain-relaxed InGaAs layers with 1.5 micrometre cw and pulse excitation," *Japanese Journal of Applied Physics*, vol. 55, 04EH12, 4 2016.

[75] R. J. Dietz, B. Globisch, M. Gerhard, A. Velauthapillai, D. Stanze, H. Roehle, M. Koch, T. Göbel, and M. Schell, "64 microwatts pulsed terahertz emission from growth optimized InGaAs/InAlAs heterostructures with separated photoconductive and trapping regions," *Applied Physics Letters*, vol. 103, p. 061 103, 6 2013.

[76] P. Gu, M. Tani, S. Kono, K. Sakai, and X. C. Zhang, "Study of terahertz radiation from inas and insb," *Journal of Applied Physics*, vol. 91, p. 5533, 9 2002.

[77] K. Bertulis, A. Krotkus, G. Aleksejenko, V. Pačebutas, R. Adomavičius, G. Molis, and S. Marcinkevičius, "Gabias: A material for optoelectronic terahertz devices," *Applied Physics Letters*, vol. 88, p. 201 112, 20 2006.

[78] C. M. Collier, T. J. Stirling, I. R. Hristovski, J. D. Krupa, and J. F. Holzman, "Photoconductive terahertz generation from textured semiconductor materials," *Scientific Reports*, vol. 6, pp. 1–10, 1 2016.

[79] G. Segschneider, T. Dekorsy, H. Kurz, R. Hey, and K. Ploog, "Energy resolved ultrafast relaxation dynamics close to the band edge of low-temperature grown gaas," *Applied Physics Letters*, vol. 71, pp. 2779–2781, 19 1997.

[80] I. S. Gregory, C. Baker, W. R. Tribe, M. J. Evans, H. E. Beere, E. H. Linfield, A. G. Davies, and M. Missous, "High resistivity annealed low-temperature gaas with 100 fs lifetimes," *Applied Physics Letters*, vol. 83, pp. 4199–4201, 20 2003.

[81] D. R. Bacon, "Time-resolved pump-probe investigation of the terahertz quantum cascade laser," University of Leeds, 2017.

[82] C. Russell, C. D. Wood, A. D. Burnett, L. Li, E. H. Linfield, A. G. Davies, and J. E. Cunningham, "Spectroscopy of polycrystalline materials using thinned-substrate planar goubau line at cryogenic temperatures," *Lab on a Chip*, vol. 13, pp. 4065–4070, 20 2013.

[83] M. Tani, M. Herrmann, and K. Sakai, "Generation and detection of terahertz pulsed radiation with photoconductive antennas and its application to imaging," *Measurement Science and Technology*, vol. 13, pp. 1739–1745, 11 2002.

[84] M. Stone, M. Naftaly, R. Miles, J. Fletcher, and D. Steenson, "Electrical and radiation characteristics of semilarge photoconductive terahertz emitters," *IEEE Transactions on Microwave Theory and Techniques*, vol. 52, pp. 2420–2429, 10 2004.

[85] N. C. J. van der Valk, T. Wenckebach, and P. C. M. Planken, "Full mathematical description of electro-optic detection in optically isotropic crystals," *Journal of the Optical Society of America B*, vol. 21, p. 622, 3 2004.

[86] S. Watanabe, "Terahertz polarization imaging and its applications," *Photonics*, vol. 5, p. 58, 4 2018.

[87] T. D. Popescu, "Introduction to signal processing," *Control Engineering Practice*, vol. 4, pp. 1771–1772, 12 1996.

[88] M. van Exter, C. Fattinger, and D. Grischkowsky, "Terahertz time-domain spectroscopy of water vapor," *Optics Letters*, vol. 14, p. 1128, 20 1989.

[89] S. Kasap, *Principles of electronic materials and devices*. McGraw-Hill, 2006, p. 874.

[90] N. Greenall, "Parameter extraction and uncertainty in terahertz time-domain spectroscopic measurements," University of Leeds, 2017, pp. 1–278.

[91] L. Duvillaret, F. Garet, and J.-L. Coutaz, "A reliable method for extraction of material parameters in terahertz time-domain spectroscopy," *IEEE Journal of Selected Topics in Quantum Electronics*, vol. 2, pp. 739–746, 3 1996.

[92] W. Kohn and L. J. Sham, "Self-consistent equations including exchange and correlation effects," *Physical Review*, vol. 140, A1133–A1138, 4A 1965.

[93] K. Berzins, J. J. Sutton, S. J. Fraser-Miller, T. Rades, T. M. Korter, and K. C. Gordon, "Solving the Computational Puzzle: Toward a Pragmatic Pathway for Modeling Low-Energy Vibrational Modes of Pharmaceutical Crystals," *Crystal Growth and Design*, vol. 20, pp. 6947–6955, 10 2020.

[94] M. T. Ruggiero, W. Zhang, A. D. Bond, D. M. Mittleman, and J. A. Zeitler, "Uncovering the connection between low-frequency dynamics and phase transformation phenomena in molecular solids," *Physical Review Letters*, vol. 120, p. 196 002, 19 2018.

[95] M. E. Paul, T. H. D. Silva, and M. D. King, "True polymorphic phase transition or dynamic crystal disorder? an investigation into the unusual phase behavior of barbituric acid dihydrate," *Crystal Growth and Design*, vol. 19, pp. 4745–4753, 8 2019.

[96] P. Makkar and N. N. Ghosh, "A review on the use of dft for the prediction of the properties of nanomaterials," *RSC Advances*, vol. 11, pp. 27 897–27 924, 45 2021.

[97] J. A. Hachtel, J. Huang, I. Popovs, S. Jansone-Popova, J. K. Keum, J. Jakowski, T. C. Lovejoy, N. Dellby, O. L. Krivanek, and J. C. Idrobo, "Identification of site-specific isotopic labels by vibrational spectroscopy in the electron microscope," *Science*, vol. 363, pp. 525–528, 6426 2019.

[98] P. Hohenberg and W. Kohn, "Inhomogeneous electron gas," *Physical Review*, vol. 136, B864–B871, 3B 1964.

[99] V. Sahni, K. P. Bohnen, and M. K. Harbola, "Analysis of the local-density approximation of density-functional theory," *Physical Review A*, vol. 37, p. 1895, 6 1988.

[100] J. P. Perdew and K. Burke, "Generalized gradient approximation for the exchange-correlation hole of a many-electron system," *Physical Review B*, vol. 54, p. 16 533, 23 1996.

[101] J. W. Furness, A. D. Kaplan, J. Ning, J. P. Perdew, and J. Sun, "Construction of meta-GGA functionals through restoration of exact constraint adherence to regularized SCAN functionals," *Journal of Chemical Physics*, vol. 156, 3 2021.

[102] P. J. Stephens, F. J. Devlin, C. F. Chabalowski, and M. J. Frisch, "Ab initio calculation of vibrational absorption and circular dichroism spectra using density functional force fields," *Journal of Physical Chemistry®*, vol. 98, pp. 11 623–11 627, 45 1994.

[103] J. P. Perdew, K. Burke, and M. Ernzerhof, "Generalized gradient approximation made simple," *Physical Review Letters*, vol. 77, p. 3865, 18 1996.

[104] H. J. Monkhorst and J. D. Pack, "Special points for brillouin-zone integrations," *Physical Review B*, vol. 13, pp. 5188–5192, 12 1976.

[105] S. Huzinaga, "Basis sets for molecular calculations," *Computer Physics Reports*, vol. 2, pp. 281–339, 6 1985.

[106] T. A. Halgren, D. A. Kleier, J. H. Hall, L. D. Brown, and W. N. Lipscomb4, "Speed and Accuracy in Molecular Orbital Calculations. A Comparison of CNDO/2, INDO, PRDDO, STO-3G, and Other Methods, Including AAMOM, VRDDO, and ESE MO," *Journal of the American Chemical Society*, vol. 100, pp. 6595–6608, 21 1978.

[107] T. D. Kühne, M. Iannuzzi, M. D. Ben, V. V. Rybkin, P. Seewald, F. Stein, T. Laino, R. Z. Khaliullin, O. Schütt, F. Schiffmann, D. Golze, J. Wilhelm, S. Chulkov, M. H. Bani-Hashemian, V. Weber, U. Borštnik, M. Taillefumier, A. S. Jakobovits, A. Lazzaro, H. Pabst, T. Müller, R. Schade, M. Guidon, S. Andermatt, N. Holmberg, G. K. Schenter, A. Hehn, A. Bussy, F. Belleflamme, G. Tabacchi, A. Glöß, M. Lass, I. Bethune, C. J. Mundy, C. Plessl, M. Watkins, J. VandeVondele, M. Krack, and J. Hutter, "CP2k: An electronic structure and molecular dynamics software package - quickstep: Efficient and accurate electronic structure calculations," *The Journal of Chemical Physics*, vol. 152, no. 19, p. 194 103, 2020.

[108] R. Dovesi, F. Pascale, B. Civalleri, K. Doll, N. M. Harrison, I. Bush, P. D'arco, Y. Noël, M. Rérat, P. Carbonnière, *et al.*, "The CRYSTAL code, 1976–2020 and beyond, a long story," *The Journal of chemical physics*, vol. 152, no. 20, p. 204 111, 2020.

[109] D. R. Hamann, M. Schlüter, and C. Chiang, "Norm-conserving pseudopotentials," *Physical Review Letters*, vol. 43, p. 1494, 20 1979.

[110] D. Vanderbilt, "Soft self-consistent pseudopotentials in a generalized eigenvalue formalism," *Physical Review B*, vol. 41, p. 7892, 11 1990.

[111] P. E. Blöchl, "Projector augmented-wave method," *Physical Review B*, vol. 50, p. 17 953, 24 1994.

[112] J. Hafner, "Ab-initio simulations of materials using vasp: Density-functional theory and beyond," *Journal of Computational Chemistry*, vol. 29, pp. 2044–2078, 13 2008.

[113] P. Giannozzi and S. Baroni, "Density-functional perturbation theory," *Handbook of Materials Modeling*, pp. 195–214, 2005.

[114] G. Kresse, J. Furthmüller, and J. Hafner, "Ab initio force constant approach to phonon dispersion relations of diamond and graphite," *Europhysics Letters*, vol. 32, p. 729, 9 1995.

[115] K. Parlinski, Z. Q. Li, and Y. Kawazoe, "First-Principles Determination of the Soft Mode in Cubic ZrO$_2$," *Physical Review Letters*, vol. 78, p. 4063, 21 1997.

[116] S. Baroni, S. D. Gironcoli, A. D. Corso, and P. Giannozzi, "Phonons and related crystal properties from density-functional perturbation theory," *Reviews of Modern Physics*, vol. 73, p. 515, 2 2001.

[117] X. Gonze and C. Lee, "Dynamical matrices, born effective charges, dielectric permittivity tensors, and interatomic force constants from density-functional perturbation theory," *Physical Review B*, vol. 55, p. 10 355, 16 1997.

[118] S. Kristyan and P. Pulay, "Can (semi)local density functional theory account for the London dispersion forces?" *Chemical Physics Letters*, vol. 229, pp. 175–180, 3 1994.

[119] S. Kozuch, D. Gruzman, and J. M. Martin, "DSD-BLYP: A general purpose double hybrid density functional including spin component scaling and dispersion correction," *Journal of Physical Chemistry C*, vol. 114, pp. 20 801–20 808, 48 2010.

[120] S. Grimme, "Semiempirical GGA-type density functional constructed with a long-range dispersion correction," *Journal of Computational Chemistry*, vol. 27, pp. 1787–1799, 15 2006.

[121] S. Grimme, J. Antony, S. Ehrlich, and H. Krieg, "A consistent and accurate ab initio parametrization of density functional dispersion correction (DFT-D) for the 94 elements H-Pu," *Journal of Chemical Physics*, vol. 132, p. 154 104, 15 2010.

[122] A. D. Becke and E. R. Johnson, "A density-functional model of the dispersion interaction," *Journal of Chemical Physics*, vol. 123, p. 154 101, 15 2005.

[123] J. Kendrick and A. D. Burnett, "Exploring the Reliability of DFT Calculations of the Infrared and Terahertz Spectra of Sodium Peroxodisulfate," *Journal of Infrared, Millimeter, and Terahertz Waves*, vol. 41, pp. 382–413, 4 2020.

[124] A. Tkatchenko and M. Scheffler, "Accurate Molecular Van Der Waals Interactions from Ground-State Electron Density and Free-Atom Reference Data," *Physical Review Letters*, vol. 102, p. 073 005, 7 2009.

[125] A. Tkatchenko, R. A. DiStasio, R. Car, and M. Scheffler, "Accurate and Efficient Method for Many-Body van der Waals Interactions," *Phys. Rev. Lett.*, vol. 108, p. 236 402, 23 2012.

[126] S. N. Steinmann and C. Corminboeuf, "A generalized-gradient approximation exchange hole model for dispersion coefficients," *Journal of Chemical Physics*, vol. 134, p. 044 117, 4 2011.

[127] E. Caldeweyher, C. Bannwarth, and S. Grimme, "Extension of the D3 dispersion coefficient model," *The Journal of Chemical Physics*, vol. 147, p. 034 112, 3 2017.

[128] J. D. Louck and H. W. Galbraith, "Eckart vectors, eckart frames, and polyatomic molecules," *Reviews of Modern Physics*, vol. 48, p. 69, 1 1976.

[129] S. J. Clark, M. D. Segall, C. J. Pickard, P. J. Hasnip, M. I. Probert, K. Refson, and M. C. Payne, "First principles methods using CASTEP," *Zeitschrift fur Kristallographie*, vol. 220, pp. 567–570, 5-6 2005.

[130] J. D. Gale and A. L. Rohl, "The General Utility Lattice Program (GULP)," *Molecular Simulation*, vol. 29, pp. 291–341, 5 2011.

[131] A. Togo and I. Tanaka, "First principles phonon calculations in materials science," *Scripta Materialia*, vol. 108, pp. 1–5, 2015.

[132] J. Kendrick and A. D. Burnett, "PDielec: The calculation of infrared and terahertz absorption for powdered crystals.," *Journal of computational chemistry*, vol. 37, pp. 1491–1504, 16 2016.

[133] J. Kendrick, A. D. Burnett, and C. N. Towler, *JohnKendrick/PDielec: PDielec Version 7.1.1 - Powder and Single Crystal Infrared Calculations*, version v7.1.1, Jan. 2022.

[134] E. B. Wilson, J. C. Decius, P. C. Cross, and B. R. Sundheim, "Molecular vibrations: The theory of infrared and raman vibrational spectra," *Journal of The Electrochemical Society*, vol. 102, 235Ca, 9 1955.

[135] J. H. Smith, S. E. Dann, M. R. J. Elsegood, S. H. Dale, and C. G. Blatchford, "α-lactose monohydrate: A redetermination at 150 k," *Acta Crystallographica Section E Structure Reports Online*, vol. 61, o2499–o2501, 8 2005.

[136] C. R. Groom, I. J. Bruno, M. P. Lightfoot, and S. C. Ward, "The cambridge structural database," *Acta Crystallographica Section B Structural Science, Crystal Engineering and Materials*, vol. 72, pp. 171–179, 2 2016.

[137] D. A. Bruggeman, "Berechnung verschiedener physikalischer konstanten von heterogenen substanzen. i. dielektrizitätskonstanten und leitfähigkeiten der mischkörper aus isotropen substanzen," *Annalen der Physik*, vol. 416, pp. 636–664, 7 1935.

[138] E. P. Parrott, J. A. Zeitler, and L. F. Gladden, "Accurate determination of optical coefficients from chemical samples using terahertz time-domain spectroscopy and effective medium theory," *Optics Letters, Vol. 34, Issue 23, pp. 3722-3724*, vol. 34, pp. 3722–3724, 23 2009.

[139] S. P. Ong, W. D. Richards, A. Jain, G. Hautier, M. Kocher, S. Cholia, D. Gunter, V. L. Chevrier, K. A. Persson, and G. Ceder, "Python materials genomics (pymatgen): A robust, open-source python library for materials analysis," *Computational Materials Science*, vol. 68, pp. 314–319, 2013.

[140] L. Ward, A. Dunn, A. Faghaninia, N. E. Zimmermann, S. Bajaj, Q. Wang, J. Montoya, J. Chen, K. Bystrom, M. Dylla, K. Chard, M. Asta, K. A. Persson, G. J. Snyder, I. Foster, and A. Jain, "Matminer: An open source toolkit for materials data mining," *Computational Materials Science*, vol. 152, pp. 60–69, 2018.

[141] P. U. Jepsen and S. J. Clark, "Precise ab-initio prediction of terahertz vibrational modes in crystalline systems," *Chemical Physics Letters*, vol. 442, pp. 275–280, 4-6 2007.

[142] F. Teixeira and M. N. D. S. Cordeiro, "Improving Vibrational Mode Interpretation Using Bayesian Regression," *J. Chem. Theory Comput.*, vol. 15, no. 1, pp. 456–470, 2019.

[143] A. Erba, J. Maul, M. Ferrabone, R. Dovesi, M. Rérat, and P. Carbonnière, "Anharmonic Vibrational states of Solids from DFT Calculations. Part II: Implementation of the VSCF and VCI Methods," *Journal of Chemical Theory and Computation*, vol. 15, pp. 3766–3777, 6 2019.

[144] M. Schreyer, L. Guo, S. Thirunahari, F. Gao, and M. Garland, "Simultaneous determination of several crystal structures from powder mixtures: The combination of powder x-ray diffraction, band-target entropy minimization and rietveld methods," *Journal of Applied Crystallography*, vol. 47, pp. 659–667, 2 2014.

[145] J. L. Allen, T. J. Sanders, R. Plathe, D. Appadoo, J. Horvat, and R. A. Lewis, "Temperature-dependent terahertz spectroscopy of l-phenylalanine," *Spectrochimica Acta - Part A: Molecular and Biomolecular Spectroscopy*, vol. 260, 2021.

[146] E. Fermi, J. R. Pasta, and S. M. Ulam, "Studies of nonlinear problems," 1955.

[147] M Sri, H. Puneet, K. Patra, M. S. Harish, and P. K. Patra, "Temperature and its control in molecular dynamics simulations," *Molecular Simulation*, vol. 47, pp. 701–729, 9 2021.

[148] A. C. Brańka, M Kowalik, K. W. Wojciechowski, A. C. Bran´ka, B. Bran´ka, and. M. Kowalik, "Generalization of the nosé–hoover approach," *The Journal of Chemical Physics*, vol. 119, p. 1929, 4 2003.

[149] P. K. Patra and B. Bhattacharya, "A deterministic thermostat for controlling temperature using all degrees of freedom," *The Journal of Chemical Physics*, vol. 140, p. 064 106, 6 2014.

[150] X. Dai, S. Fan, Z. Qian, R. Wang, V. P. Wallace, and Y. Sun, "Prediction of the terahertz absorption features with a straightforward molecular dynamics method," *Spectrochimica Acta Part A: Molecular and Biomolecular Spectroscopy*, vol. 236, p. 118 330, 2020.

[151] S. N. Thakur, L. Goodman, and A. G. Ozkabak, "The benzene ground state potential surface. i. fundamental frequencies for the planar vibrations," *The Journal of Chemical Physics*, vol. 84, p. 6642, 12 1998.

[152] Y. Haas and S. Zilberg, "The v14(b2u) mode of benzene in s0 and s1 and the distortive nature of the π-electron system: Theory and experiment," *Journal of the American Chemical Society*, vol. 117, pp. 5387–5388, 19 1995.

[153] F. A. Miller and B. L. Crawford, "The non-planar vibrations of benzene," *The Journal of Chemical Physics*, vol. 14, p. 282, 4 2004.

[154] S. Wang, "Intrinsic molecular vibration and rigorous vibrational assignment of benzene by first-principles molecular dynamics," *Scientific Reports*, vol. 10, pp. 1–14, 1 2020.

[155] R. Car, F. de Angelis, P. Giannozzi, and N. Marzari, "First-principles molecular dynamics," in *Handbook of Materials Modeling: Methods*, S. Yip, Ed. Dordrecht: Springer Netherlands, 2005, pp. 59–76.

[156] H. Gai and G. A. Voth, "First-principles molecular dynamics study of surface vibrations and vibrational mode coupling on the H/Si(111)1×1 surface," *The Journal of Chemical Physics*, vol. 101, p. 1734, 2 1998.

[157] S. Yatsyshyn, *Handbook of Thermometry and Nanothermometry*. Ifsa Publishing, 2015.

[158] F. Kawaizumi, N. Nishio, H. Nomura, and Y. Miyahara, "Heat-capacity measurements of aqueous solutions of mono-, di-, and tri-saccharides using an isoperibol twin calorimeter," *The Journal of Chemical Thermodynamics*, vol. 13, pp. 89–98, 1 1981.

[159] C. Červinka, M. Fulem, R. P. Stoffel, and R. Dronskowski, "Thermodynamic properties of molecular crystals calculated within the quasi-harmonic approximation," *Journal of Physical Chemistry A*, vol. 120, pp. 2022–2034, 12 2016.

[160] S. L. Mathews, P. D. Servio, and A. D. Rey, "Heat capacity, thermal expansion coefficient, and grüneisen parameter of ch4, co2, and c2h6hydrates and ice ihvia density functional theory and phonon calculations," *Crystal Growth and Design*, vol. 20, pp. 5947–5955, 9 2020.

[161] J. M. Skelton, L. A. Burton, S. C. Parker, A. Walsh, C. E. Kim, A. Soon, J. Buckeridge, A. A. Sokol, C. R. A. Catlow, A. Togo, and I. Tanaka, "Anharmonicity in the high-temperature cmcm phase of snse: Soft modes and three-phonon interactions," *Physical Review Letters*, vol. 117, p. 075 502, 7 2016.

[162] F. Druon, F. Balembois, and P. Georges, "New laser crystals for the generation of ultrashort pulses," *Comptes Rendus Physique*, vol. 8, pp. 153–164, 2 2007.

[163] R. M. Smith and M. A. Arnold, "Terahertz Time-Domain Spectroscopy of Solid Samples: Principles, Applications, and Challenges," *Applied Spectroscopy Reviews*, vol. 46, pp. 636–679, 8 2011.

[164] K. N. Murphy, M. Naftaly, A. Nordon, and D. Markl, "Polymer pellet fabrication for accurate thz-tds measurements," *Applied Sciences 2022, Vol. 12, Page 3475*, vol. 12, p. 3475, 7 2022.

[165] D. R. Bacon, C. Russell, M. Swithenbank, L. Li, E. H. Linfield, J. Cunningham, J. R. Freeman, C. D. Wood, P. Dean, A. D. Burnett, and A. G. Davies, "Free-space terahertz radiation from a LT-GaAs-on-quartz large-area photoconductive emitter," *Optics Express*, vol. 24, pp. 26 986–26 997, 23 2016.